A CASE STUDY OF MATERIAL TESTING FOR CORROSION IN LOW TEMPERATURE GEOTHERMAL SYSTEMS

A Thesis submitted to
the Graduate School of Engineering and Science of
Izmir Institute of Technology
in Partial Fulfillment of the Requirements for the Degree of

MASTER OF SCIENCE

in Materials Science and Engineering

by
Umut İNCE

July, 2005
Izmir, Turkey

We approve the thesis of **Umut İNCE**

                                                          Date of Signature

....   **25 July 2005**
Assoc. Prof. Dr. Mustafa GÜDEN
Supervisor
Department of Mechanical Engineering
Izmir Institute of Technology

....   **25 July 2005**
Prof. Dr. Macit TOKSOY
Co-Supervisor
Department of Mechanical Engineering
Izmir Institute of Technology

....   **25 July 2005**
Prof. Dr. Muhsin ÇİFTÇİOĞLU
Department of Material Science and Engineering
Izmir Institute of Technology

....   **25 July 2005**
Prof. Dr. Zafer İLKEN
Department of Mechanical Engineering
Izmir Institute of Technology

....   **25 July 2005**
Assoc. Prof. Dr. Sedat AKKURT
Department of Mechanical Engineering
Izmir Institute of Technology

....   **25 July 2005**
Prof. Dr. Muhsin ÇİFTÇİOĞLU
Head of Department
Izmir Institute of Technology

                    ....
                    Assoc. Prof. Dr. Semahat Özdemir
                    Head of the Graduate School

ACKNOWLEDGEMENTS

ABSTRACT

The main goal of this study is to determine the corrosion rate and mechanisms of an St-37 steel material currently used as a pipeline material in Izmir–Balçova Geothermal District Heating System. Alternative steel piping materials, AISI 304, AISI 316, AISI 316L austenitic stainless steels, were also investigated for their corrosion behaviour in the same geothermal system. Two fluid velocities, 0.02 and 9.6 m/s, showing the low or stagnant and high velocity fluid flow respectively were selected for the corrosion experiments at the site. Intentionally prepared tensile St-37 test specimens were used to investigate the effect of corrosion (particularly pitting type of corrosion) on the ultimate tensile strength of the steel, while conventional test coupons were used in the testing of stainless steels. These tests were further accompanied by the qualitative laboratory tests involving Ryznar stability index and electropotential measurements. It was found that laboratory measurements, Ryznar stability index, pitting resistance equivalent and electropotential measurements showed good agreement with the result of corrosion experiments conducted at the site. Although the uniform corrosion rates were relatively low in the tested steels, the pitting corrosion rate was greatly promoted in St-37 samples at the low fluid velocity, mainly driven by the SRB activity and tubercle formation. The tensile tests on the St-37 corroded samples have further shown that the UTS decreased as the exposure time increased. The decrease in the UTS of St-37 was more pronounced in the samples tested at the lower fluid velocity, which showed a good agreement with the measured maximum pitting depths found in these samples. The service life time of the St-37 was further predicted for two selected fluid velocities using the equations developed for the effect of defects on the bursting pressure of the pipelines. The predicted service life of St-37 was 57 and 95 months for low and high velocity fluid flow respectively. These service lives were also comparable with the reported service life of the pipelines used in the studied geothermal system. Finally, a solution were proposed to increase the service lifetime of St-37 pipes: addition of SRB activity reducing reagents to the fluid.

ÖZ

Bu çalışmada Izmir-Balçova bölgesel jeotermal ısıtma sisteminde yaygın şekilde boru malzemesi olarak kullanılan St-37 çeliğiyle alternatif AISI 304, 316, 316L östenitik paslanmaz çeliklerin ortalama özelliklere sahip bir jeotermal kuyu içerisindeki korozyon davranışı ve korozyon hızları 0.02 m/s ve 9.6 m/s akışkan hızlarında belirlenmiştir. Korozyona uğramış çeliğin mekaniksel özelliklerindeki değişimini incelemek ve boru hatlarının sistemdeki ömürlerini saptamak amacıyla St-37 çeliği korozyon testi numuneleri çekme deneyi numunesi biçiminde yapılmıştır. Paslanmaz çelik numuneleri ise korozyon deneylerinde sıklıkla kullanılan biçim ve boyutta, dikdörtgen olarak şekillendirilmiştir. Öncelikle yapılan Ryznar indeksi, çukurcuk korozyonu dayanım denklemi hesaplamaları ve elekto-potensiyel ölçümleri ile tahmin edilen korozyon davranışları ve yapılan niteliksel karşılaştırmaların uzun süreli saha deneyleriyle büyük ölçüde uyumluluk gösterdiği gözlenmiştir. Uzun süreli saha deneyleri; bütün çeliklerin düşük homojen dağılımlı korozyon hızlarına sahip olduğunu gösterirken, özellikle düşük akışkan hızında maruz bırakılmış St-37 çeliği için sulfat indirgeyici bakteriler ve "tubercle" olarak adlandırılan oluşumlar tarafından tetiklenen çukurcuk korozyonun çok daha hızlı ilerlediği tespit edilmiştir. Yapılan çekme deneyi sonuçları St-37 çeliğinin maksimum çekme gerilmesinin artan maruz kalma zamanı için azaldığını göstermiştir. Bu durumun St-37 çeliğinin yüzeyinde tespit edilen maksimum çukurcuk derinliğinin artan maruz kalma zamanı için artması ile önemli ölçüde uyumluluk gösterdiği tespit edilmiştir. Boru hatlarının patlama basınçlarının hesaplanması için geliştirilmiş olan formulasyonlar ile St-37 çeliğinden yapılmış boru hatlarının düşük akışkan hızında 57 ay ve yüksek akışkan hızında 95 ay olarak tahmin edilen ömürlerinin incelenen kuyuda kullanılan boru hatlarının ömürleriyle karşılaştırılabilir ölçüde doğru olduğu görülmüştür. Sonuç olarak boru hatlarının ömrünün arttırılması için sulfat indirgeyici bakterilerin aktivasyonunu önlemek veya indirgemek için kimyasal kullanımı önerilmiştir.

TABLE OF CONTENTS

LIST OF FIGURES

LIST OF TABLES

CHAPTER 1

INTRODUCTION

1.1. Geothermal Energy

"Geothermal" comes from the Greek words of *geo* (earth) and *thermal* (heat) and geothermal energy is literally defined as the heat contained within the Earth that generates geological phenomena on a planetary scale. However, "Geothermal energy" is used nowadays to indicate that part of the Earth's heat that can be recovered and exploited by man. The existence of valcanoes, hot springs, and other thermal phenomena was proved that parts of the interior of the Earth were hot. It was however pointed out that, it was not until a period between sixteenth and seventeenth century, when the first mines were excavated to a few hundred meters below ground level, that man deduced, from simple physical sensations, that the Earth's temperature increased with depth (Armstead 1983).

Energy resources in the earth can be divided into two groups; fossil fuels and renewable energy resources (EIA 2003, EIA 1994). Geothermal energy, which is an important renewable energy resources, has advantages and disadvantages comparing with other energy sources. World wide energy use increases by year and also with an increase in fossil fuel consumption (Figure 1.1 and Figure 1.2), leading to an increase of CO_2 concentration in the atmosphere. On the contrary, the geothermal energy is environmentally friendly and leads to lesser amounts of CO_2 emmision to the atmosphere (Figure 1.2). The equivalent savings in the production of CO_2 from electricity generation and direct-use of geothermal systems from fuel oils, natural gas and coal was 89.8, 21.2 and 104.8 millions tons respectively until 1990. Similar numbers were also determined for sulfur oxides as 0, 0.56 and 0.59 million tons for natural gas, fuel oil and coal respectively until 1990 (Goddart 1990). Geothermal energy requires very little land for geothermal power plant that has comparable price to that of fossil-fuel power stations and has less risk than nuclear power plants. Geothermal energy is an limitless source of energy, if it is used in a sustainable way. On the other hand, geothermal energy contains non-condensable gases, noise and odor can be

occurred by geothermal water, geothermal systems have very high startup costs, there can be unknown effects on earth's geologic anomolaus and heated core and not all areas are suitable for geothermal energy.
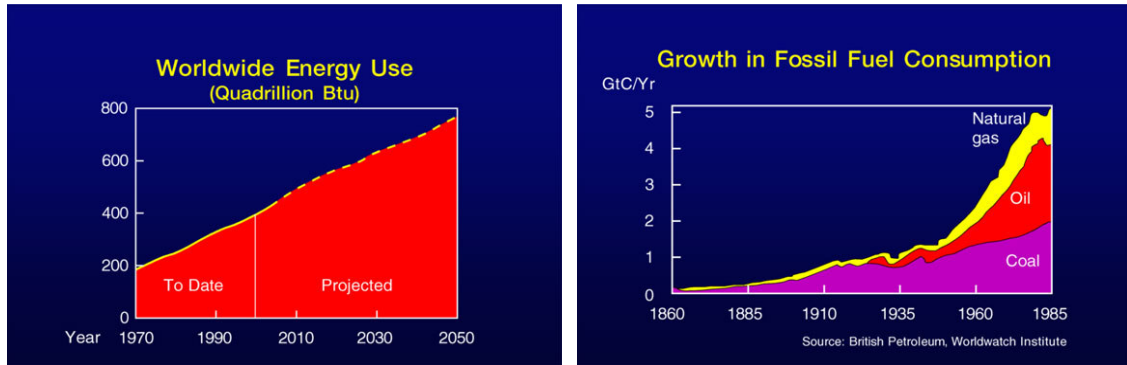
Figure 1.1. Change on worldwide energy use and growth in fossil fuel consumptions (Nemzer and Carter 2000).
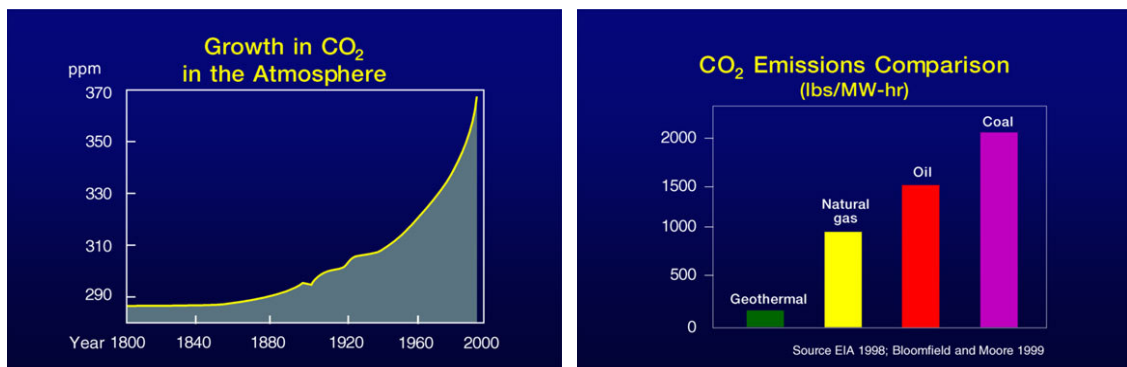
Figure 1.2. Change on growth in CO_2 in the atmosphere with years and CO_2 emissions from energy consumption for electricity generation (Nemzer and Carter 2000).

Geothermal heat originates from earth's fiery consolidation of dust and gas over 4 billion years ago. Calculations showed that the Earth would have cooled and become completely solid without an energy input in addition to that of the sun. It was also proposed that the ultimate source of geothermal energy is radioactive decay within the earth (Bullard 1973). At Earth's core, 6370 km deep, temperatures may reach over 5000 ^{o}C (Figure 1.3). The geothermal gradient expresses the increase in temperature with depth in the Earth's crust. The average geothermal gradient was determined to be about 2.5-3 ^{o}C per 100 m, down to the depth accesible by drilling with modern technology (Hochstein 1990). Geothermal systems can therefore be found in regions with a normal or slightly above the normal geothermal gradient. Geothermal systems can be described

as "convecting water in the upper crust of the Earth, which, in a confined space, transfers heat from a heat source to a heat sink, usually the free surface".
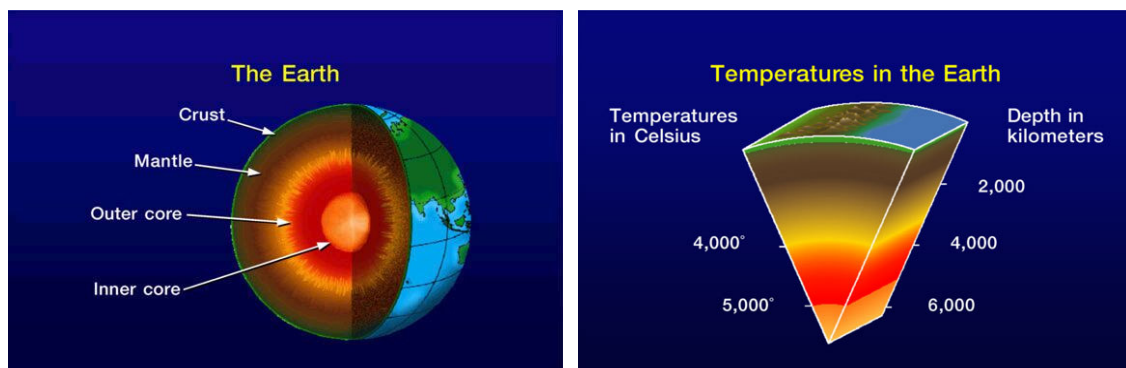
Figure 1.3. Temperatures in Earth and layer of the Earth (Nemzer and Carter 2000).

A geothermal system may be considered as composing of main elements: a heat source, a reservoir and a fluid. The heat source can be either a very high temperature ($>600\ ^0C$) magmatic intrusion that has reached relatively shallow depths (5-10 km) or, as in low temperature systems, the Earth's normal temperature increases with depth. The reservoir is a volume of hot permeable rocks and it is covered with impermeable rocks that prevents hot fluids from easily escaping the surface and keep the volume under pressure, see Figure 1.4 as an ideal geothermal system. The fluids are meteoric waters that can penetrate into the Earth's crust from the recharge areas through hot permeable rocks and can accumulate in reservoir. The fluid may be found as liquid or vapor phase depending on the temperature and pressure and often containes some chemicals and gases. The hot water and/or steam may be extracted by boreholes or, as in the case of springs, escape from the reservoir by natural means. Once, hot water and/or steam travels up to the surface, they can be used in many different types of application (Lindal 1973).

The use of geothermal resources may be divide into three catagories: these are electricity generation, direct-use applications and ground source heat pump applications. The use of geothermal energy for electricity generation was started in 1913 when a power plant of 250kWe was installed in Italy. This development was followed by new power plants installed in New Zealand (1958), Mexico (1959) and United States (1960) (Lund 1999). The geothermal electric and direct-use capacity, and energy use was determined on worldwide based on the papers of 59 countries submitted to the World Geothermal Congress 2000. According to the report, the total capacity of the installed

3

geothermal electric power plants in 21 countries was 7974 MWe and it was predicted that the total installed direct-use plants would increase to a cpacity of 15145 MWe in 58 reporting countries at the end of 2005 (Huttrer 2000).
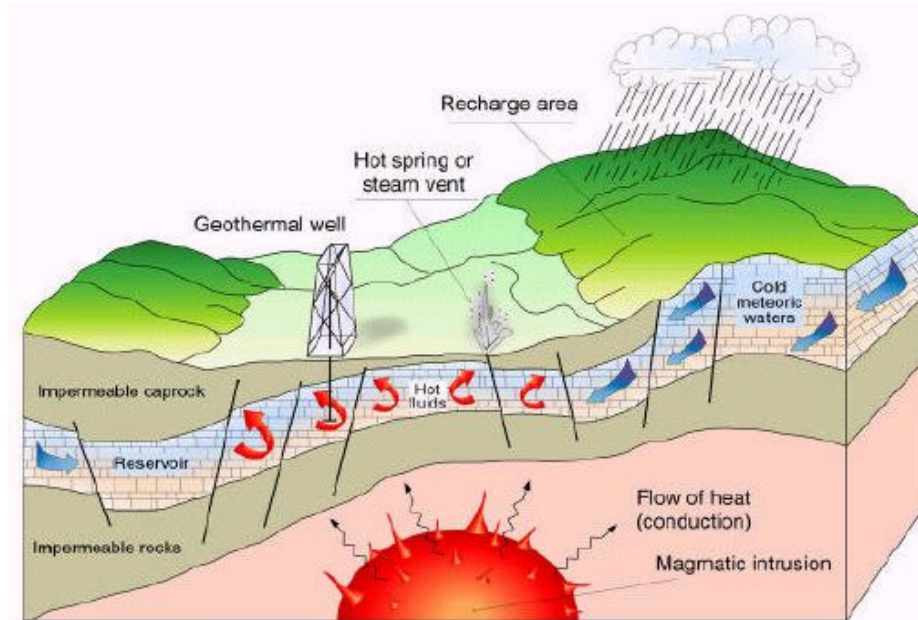
Figure 1.4. Schematic representation of an ideal geothermal system (Armstead 1983)

According to Hepbaşlı ve Özgener, there are 11 geothermal district heating systems with a total cpacity of 820 MW_t in Turkey (Hepbaşlı ve Özgener 2003). Another report gave 992 MW_t total capacity of geothermal district heating systems in Turkey (Mertoğlu et al. 2000). According to Akkuş (Akkuş et al. 2002), the electricity generation and district heating capacity of geothermal systems in Turkey were 764,81 MW_e and 1039 MW_t, respectively. Electricity generation takes place in conventional steam turbines and binary plants. Conventional steam turbines operate with a minimum fluid temperature of 150°C. Atmospheric or condensing exhausts are available for the conventional steam turbines. The steam, which comes from dry steam wells directly or, comes from wet wells after seperation process, is passed through a turbine and exhausted to the atmosphere by generating electricity. The used geothermal fluid is then reinjected into the reservoir, through an injection well, in order to be reheated, to maintain pressure and to prevent loss of level on geothermal reservoir. The condensing units are more complex and installation costs more expensive while steam consumption is half lesser than atmospheric units. The binary plants utilize secondary working fluids like waste hot waters coming from the seperators. The secondary fluid is used by a

Rankine cycle where the geothermal fluid yields heat to the secondary fluids via heat exchangers, in which this fluid is heated and vaporized, this vapour is used on a turbine to generate electricity and then cooled and condensed, and the cycle begins again .

Direct heat use is one of the oldest, most verstaile and most common form of the utilization of geothemal energy. Geothermal fluids can be used to grow vegetables, flowers and other crops in green houses. Geothermal fluids can be also used to shorten the time for growing fish, to dry onions and lumber and to wash wool, to pasteurize milk and also space heating of individual buildings and of entire districts, is besides hot spring bathing. In a typical direct-use system, the geothermal fluid is produced from the production borehole, when the geothermal fluid reaches the surface, it is delivered to the application site through the transmission and distrubition system (Figure 1.5).
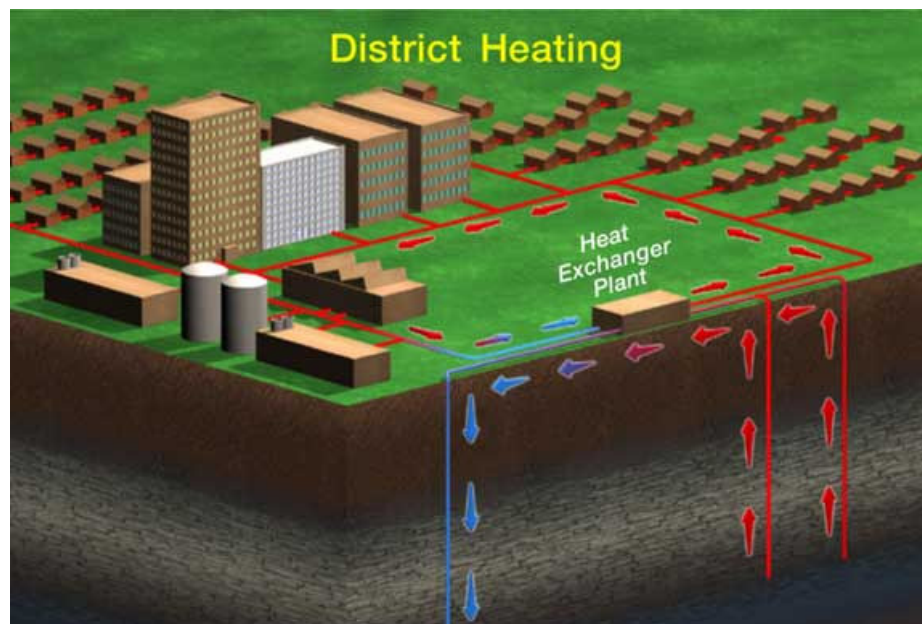
Figure 1.5. A sample of district heating system (Nemzer and Carter 2000).

In a geothermal direct use system, the geothermal production and disposal systems are coupled, and seperated from the contact by a heat exchanger as depicted schematically in Figure 1.5. The secondary loop is commonly used in large systems to limit the exposure of geothermal fluid to a small potion of the system. In such large systems, there is also a second heat exchanger thet transfers the heat to the building's heating systems. The fluid in the first loop is injected directly back into re-injection area to be heated and used again after from the contact with the heat exchanger. Geothermal heat pumps (GHPs) take the advantages of the earth temperature (about 7-15 ^{0}C) just a

few meters below the surface. GHPs are used both for heating or cooling depending on the weather condition. Buildings are heated using the difference between the earth's temperature and the colder temperature of the air via buried pipelines. In the heating mode, the cold circulating liquid absorbs heat from the ground. This heat is recovered by the heat pump. In the summer, the cooler ground absorbs the surplus heat from houses and buildings more efficiently than the hot air above the ground. Electrical power is used to concentrate heat and move it from one place to another. No any active technology of home cooling is more efficient than the geothermal heat pumps (EIA 1994).

1.2. Definition and Classification of Geothermal Resources

Geothermal resources can be classified based on the enthalpy or temperature of the geothermal fluids. The resources are divided into low, medium and high enthalpy or temperature resources according to several criteria (Table 1.1). Another classification is based on the pressure controlling phase: the liquid-dominated (water –dominated) or vapor-daminated system (White 1973). In liquid-dominated systems, although some vapour may be present, the liquid water is the continuous, pressure controlling phase. Liquid water and vapour are co-exist in the reservoir with vapour continuous, pressure controlling phase in vapour-dominated systems. Geothermal systems can also be classified based on the reservoir equilibrium state (Nicholson 1993). The reservoir is continually recharged by water that is heated and then discharged from the reservoir in the dynamic systems. This category includes low-temperature ($<150\ ^0$C) and high temperature systems ($>150\ ^0$C). Heat transfer is occurred by convection and circulation of fluid in dynamic systems. There is no recharge or only minor recharges in static systems, which includes low-temperature and geo-pressured systems. Heat is only transferred by conduction in these systems.

Table 1.1. Classification of Geothermal Resources [Muffler 1978, Hochstein 1990]

Classification of Geothermal Resources	(a)	(b)	(c)	(d)
Low enthalpy resources - (^{0}C)	<90	<125	<100	150
Intermadiate enthalpy resources - (^{0}C)	90-150	125-225	100-200	-
High enthalpy resources - (^{0}C)	>150	>225	>200	>150

1.3. Geothermal Fluid Chemistry

The contents of geothermal fluids are composed of gases and liquids. Normal ground waters are usually near neutral in pH and slightly bicarbonate, but they tend to dissolve more sodium chloride and high in salt content when they heated to a relatively high temperature, very much similar to the geothermal systems. Carbon dioxide (CO_2) and hydogen sulfide (H_2S) are the main gases for high temperature systems. Ammonia (NH_3), hydogen (H_2), methane (CH_4), nitrogen (N_2), hydrocarbons (HC), boron (B), fluorine (F), arsenic (As) and mercury (Hg) may also be present with trace quantities of oxygen (O_2) in low and high temperature systems. The chemicals dissolved in geothermal fluid at liquid phase include chlorides (Cl), sodium (Na), Magnesium (Mg), potassium (K), fluoride (F), calcium (Ca), silicate (Si), iodine (I), antimony (Sb), strontium (sr), bicarbnonates (HCO_3), lithium (Li), arsenic (As), boron (B), hydrogen sulfide (H_2S), mercury (Hg), rubidium (Rb) and ammonia (NH_3). Table 1.2 is the chemical analyses of the geothermal fluid in B-4 well in Balçova (Izmir, Turkey) geothermal district heating system as an representative and the chemical content of geothermal fluid and their avarage concentrations are also shown in Figure 1.6 (Serpen 1999). The chemicals dissolved in geothermal fluid may differ from well to well in the same field because of the geochemistry of the reservoir. However, geothermal fluid commonly contains seven chemical species; these are oxygen, hydrogen ion, chloride ion, sulfide species, carbon dioxide species, ammonia species and sulfide ion. These chemicals have important effect on the corrosion response of materials.

Table 1.2. Analyses of geothermal fluid in B-4 well in Balçova Geothermal District Heating System.

Name	T*	pH(25)	EC (25)	Li^+	Na^+	K^+	Mg^{2+}	Ca^{2+}	B	SiO_2	HCO^{3-}	SO_4^{2-}	F^-	Cl^-
	°C		µS/cm	mg/l	mg/l	mg/l	mg/l	mg/l	mg/l	mg/l	mg/l	mg/l	mg/l	mg/l
B-4	95,7	7,38	1914	1,5	371,4	31,1	12,5	28	8,7	148	634	180	3,9	206
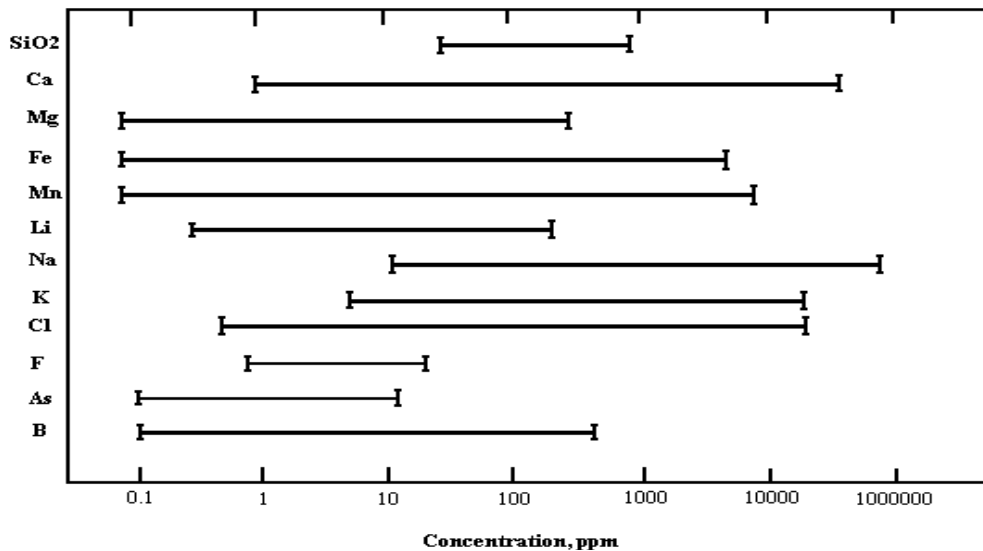
Figure 1.6. Chemical content of geothermal fluid and their average concentrations

1.4. Scaling Problems Associated with Geothermal Fluid Chemistry

The mineral salts contained in water vary depending on the local geological characteristics and climate. The dissociation of mineral salts produces anions and cations and the most common form of these anions and cations are listed in Table 1.3. The carbonic system is basically derived from the dissolution of carbon dioxide and carbonate minerals in the water. The carbonate system is a weak acid-base system, which exists in aqueous solutions as dissolved carbondioxide (CO_{2aq}), carbonic acid (H_2CO_3), bicarbonate (HCO_3^-), carbonate ions (CO_3^{2-}) and complexes of these ions such as $CaCO_3$. Natural water may also contain dissolved gases including oxygen, carbondioxide and nitrogen and the suspended and colloidal materials such as quartz, organic particles, living organisms and vegetal fragments.

Table 1.3. Principal ions contained in water (Francy et al. 1998)

Cations		Anions	
Na^+	Sodium	HCO_3^-	Bicarbonate or Hydrogen carbonate
Mg^{2+}	Magnesium	CO_3^{2-}	Carbonate
Ca^{2+}	Calcium	OH^-	Hydroxyl
K^+	Potassium	Cl^-	Chloride
Fe^{2+}, Fe^{3+}	Ferrous or Ferric	SO_4^{2-}	Sulphate
H_3O^+	Hydronium	NO_3^-	Nitrate
		$PO_4^{3-} HPO_4^{2-} H_2PO_4^-$	Phosphates
		SiO_3^{2-}	Silicate

1.4.1. Calcite Scaling

Calcium and carbonates are present in most natural waters and can have potential to form calcium carbonate ($CaCO_3$). The scaling problem is mostly derived from the destruction of the calco-carbonic balance of the water, leading to the precipitation of calcium carbonate. The change of the parameters such as the pH or concentration of the dissolved CO_2 because of the increase of temperature for example causes the destruction of calco-carbonic balance. Calcium carbonate precipates from water in one or more of three forms: calcite, arogonite and vaterite. The formation of these allotropes depends on the pressure, temperature, presence of foreign ions and the rate of the precipitation process (Loewental and Marais 1976). The calcite polymorph of calcium carbonate is the most commonly found scale-forming mineral. Vaterite is the solid phase forming first during the precipitation process. At higher temperature, though calcite is the most thermodynamically stable phase, aragonite has been reported to be the first phase to precipitate from the solution (Lippmann 1973). Usually, calcium carbonate precipitates as near cubic crystals of calcite at room temperature or as needle-like crystals of aragonite at temperatures over 65 ^{o}C. The common starting processes of the precipitation of calcium carbonate are (a) the addition of chemicals resulting in an increase of pH, which allows the dissociation of bicarbonates, (b) degassing or ventilation, which reduced the concentration of dissolved CO_2, thus increasing pH and (c) increase of the temperature of the water, which makes CO_2 less soluble and enables it to escape by unbalancing the carbonic chain. The carbonic chain process is depicted schematically in Figure 1.7. Carbonate chemistry refers to the series of chemical reactions leading to the equilibria between these reactions. Dissolved carbon dioxide are hydrated according to the following reaction :

$$CaCO_{3aq} + H_2O \Leftrightarrow CO_2, H_2O \tag{1.1}$$

The H_2CO_3 refers to the composite form, which is the sum of the activities of molecularly dissolved carbon dioxide CO_{2aq}, and the hydrated form CO_2,H_2O. The composite form is convenient due to the analytical difficulties of seperating out CO_{2aq} from CO_2,H_2O. The behavior of carbonic system is intimaley involved in the control of the pH and precipitation phenomena by the following equilibrium relationships:

$$H_2CO_3 \Leftrightarrow H^+ + HCO_3^-$$
$$HCO_3^- \Leftrightarrow H^+ + CO_3^{2-} \qquad (1.2)$$
$$Ca^{2+} + CO_3^{2-} \Leftrightarrow CaCO_3$$
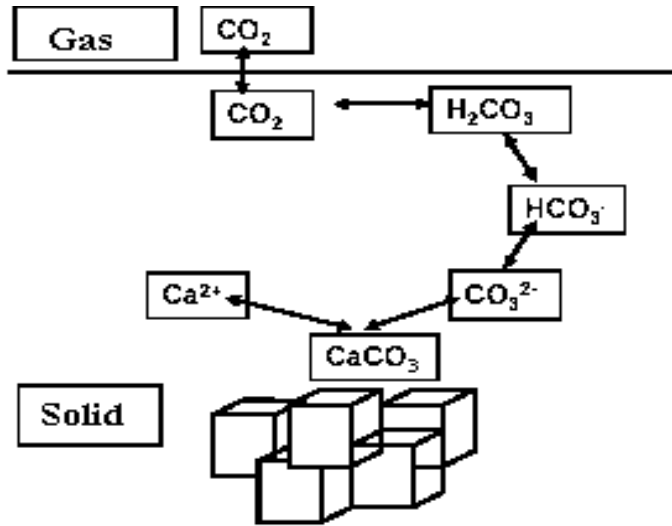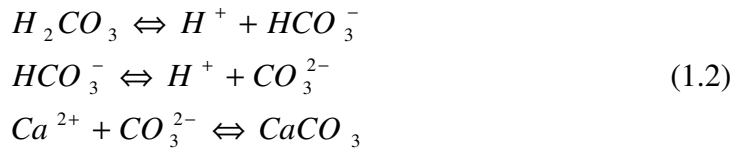
Figure 1.7. Schematic representation of carbonic chain (Francy et al. 1998).

The species involved react accordingly to the laws of mass action. When the amount of H_2CO_3 increases for some reason the equilibrium will move to dissolve the calcium carbonate. When the quantity of H_2CO_3 is less than the quantity needed for the equilibrium then $CaCO_3$ precipates and scaling will occur (Hamrouni and Dhahbi 2002). Moreover; when the solution is heated, CO_2 escapes, favoring the bicarbonate decomposition reaction followed by $CaCO_3$ precipitation by the following reactions (Web_1 2005) :

$$2HCO_3^- = CO_2(dissolved\,) + CO_3^{2-} + H_2O$$
$$Ca^{2+} + CO_3^{2-} = CaCO_3 \qquad (1.3)$$
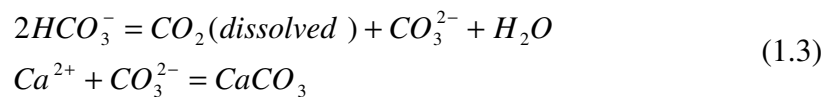
The composition of the scale in geothermal plants is found to be very complex and depends on many parameters, including the temperature and pressure of the fluid, the history of water-rock relations and the operating conditions. Geothermal systems of low and moderate fluid temperature scale consisting of calcium carbonate as a rule but there are a few exceptions has been remarked untill now. Calcium carbonate scaling

layer may be in tenths of millimeter in thick as shown in Figure 1.8, which shows a thick scaling layer on a stainless steel taken from Balçova-Izmir geothermal system.

Figure 1.8**.** Stainless steel pipe scaling layer section

There are numerous methods in use to control scale formation in geothermal systems. Some of the most common measures are the proper design of the geothermal plant and selection of operating conditions, pH adjustment, use of chemical additives and the removal of deposits by chemical or mechanical means. For instance, carbonate deposits can be prevented by the use of scale inhibitors, but the use of inhibitors in preventing sulphide and silica scaling is met by limited success. These scales can be prevented through the decreasing of the pH with the addition of mineral acids. The least desirable method is however the removal of deposits because this technique can be used to clean some specific pieces of equipment like heat exchangers or valves (Andritros et al. 1998). For many years, the Ryznar Index has been used to estimate the corrosivity and scaling tendencies of potable water supplies (Rafferty 1992). However, the statistical study found no significant correlation (at the 95 percent confidence level) between corrosion and Ryznar Index (Ellis 1985). But this has not been proofed yet for many different environments and for different types of steels. However, it has been known for many years that indexes can only give a probable indication of the potential corrosivity of a water and generally accepted that if conditions encourage the formation of a protective calcium carbonate film, then corrosion will generally be minimized. Ryznar stability index (RSI) can be used to predict the scale formation and given as (Butlin et al 1951):

$$RSI = 2\,pH_s - pH \qquad\qquad (1.4)$$

Where, pH_s is the pH above which calcium carbonate precipitate. The Ryznar stability index is interpreted as the indication for the scale formation as tabulated in Table 1.4. It should be noted that the accuracy of the Ryznar stability index is greater as a predictor of scaling than of corrosion.

Table 1.4. Interpretation of the Ryznar Stability Index (Carrier 1965).

RSI-index value	Indication
<5.0	Heavy scale
5.0-6.0	Light scale
6.0-7.0	Little scale
7.0-7.5	No scale or Little corrosion
7.5-9.0	Light corrosion
>9.0	Heavy corrosion

Langelier saturation index (LSI) was derived from thermodynamic considerations similar to the Ryznar stability index and used to predict corrosion or scaling tendency of water. It is given with the following relation,

$$LSI = pH - pH_s \qquad (1.5)$$

The LSI is an equilibrium model and provides an indicator of the degree of saturation of water with respect to calcium carbonate. LSI is probably the most widely used indicator of cooling water scale potential; however it provides no indication of how much scale or calcium carbonate will actually precipate to bring water to equilibrium. In order to calculate the LSI, it is necessary to know the alkalinity (mg/l as $CaCO_3$) the calcium hardness (mg/l Ca^{2+} as $CaCO_3$), the total dissolved solids (mg/l TDS), the actual pH, and the temperature of water (^{0}C). Flentje and by Fujii (Flentje 1961) (Fujii et al. 1983) showed that water with a less negative LSI was less corosive. Waters with a slightly negative LSI index may deposit calcium carbonate because of pH fluctuations.

1.4.2. Silica and Carbonate Scaling

Silica and carbonate scales are the ones most extensively studied in connection with geothermal resource utilisation. The precipitated minerals cause ultimately

problems by restricting the fluid flow, preventing valves from closing, scaling turbine blades etc. Chan reviewed the chemistry of silica deposition and claimed that it was neither simple nor well understood (Chan 1989). Silica deposition depends primarily on the fluid kinetics and it can be delayed from minutes to hours after its saturation limit has been exceeded (Rimstidt and Barnes 1980). The solubility of silica polymorphs with temperature has been studied extensively. Solubilities of various silica polymorphs with temperature have proven useful as geothermometers. Hot water in the reservoir is in equilibrium with quartz and undersaturated with respect to amorphous silica. When a geothermal fluid is brought to the surface, the difference in solubilities between amorphous silica and quartz allows a considerable temperature drop before the solution becomes saturated with respect to amorphous silica. The silica saturation temperature is the temperature at which separated water reaches saturation with respect to amorphous silica. When steam separation takes place above this temperature, then silica scaling usually does not take place and could depend on other dissolved species in the fluid like the fluid salinity. If re-injection is being considered, the temperature is usually kept above the amorphous silica saturation temperature. The pH dependence of silica solubility was also investigated (Henley 1983). Investigations have shown that amorphous silica solubility increased markedly as the pH (temperature) increased. Also, the dissolved salts in geothermal fluid have found appreciable effects on silica solubility. At low salinities, there are no marked effects of dissolved species on silica solubility. But as the concentration of other dissolved species, e.g. $NaNO_3$, $MgSO_4$, $MgCl_2$, increases in solution the solubility of both quartz and amorphous silica decreases. In highly concentrated solutions the cation influence on amorphous silica solubility decreases in the following order :

$Mg^{2+} > Ca^{2+} > Sr^{2+} > Li^+ > Na^+ > K^+$
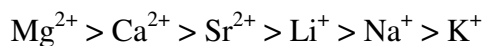
Anions also have an effect in the order:

$I^- > Br^- > Cl^-$ (Kizito 2002)
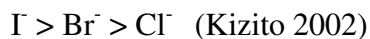
1.3.3. Metal sulphide and oxide scales.

Criaud and Foulliac (1989) noted the dissolved sulphides of metals such as lead, zinc, copper and iron in geothermal fluids and the utilization schemes and flashing induce deposition of substantial metal sulphide scales. They found that the conditions of

temperature and salinity in a low-temperature environment such as in sedimentary basins, where bacterial action have occurred, resulted in high concentrations in the fluids. Magnesium silicate scaling was also reported in heating systems. The heating of groundwater depletes the magnesium in the water, and magnesium concentration of geothermal water is mostly below 0.1 mg/kg (Krismannsdottir 1989).

CHAPTER 2

CORROSION OF STEEL IN WATER : AN OVERVIEW

The word corrode is derived from the latin "corrodore", which means " to gnaw to pieces". Corrosion can be defined in many ways. Some definitions are very narrow and deal with a specific form of corrosion, while others are quite broad and cover many forms of deterioration. As a general definition, corrosion can be defined as a chemical or electrochemical reaction between a material, usually a metal, and its environment that produces a deterioration of the material and its properties. Corrosion is a natural process and all natural processes tend toward the lowest possible energy states. In the case of iron and steel, they have a natural tendency to combine with other chemical elements like water and oxygen to return to their lowest energy states of oxides as illustrated in Figure 2.1 (Davis 2003).
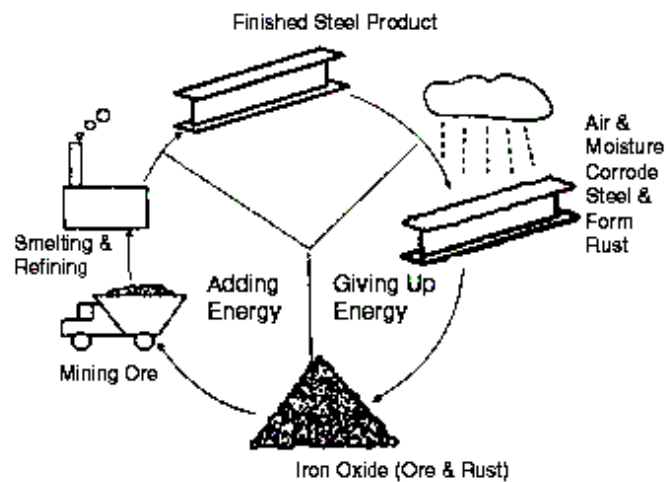
Figure 2.1. The corrosion cycle of steel.

Corrosion can be classified as low temperature and high temperature corrosion or oxidation and electrochemical corrosion or wet and dry corrosion. Wet corrosion occurs when liquid is present. This usually involves aqueous solutions or electrolytes and accounts for the greatest amount of corrosion (Fontana 1987). There are also few

principal concepts in order to understand basic corrosion phenomena and there are as followings:

- Three possible behavior of a metal when immersed in a solution
- Electrochemical reactions of corrosion
- The many forms of corrosion

2.1. Three possible behaviors of a metal immersed in a solution

When a metal is exposed to an environment, the metal can behave in three ways. One possibility is that metal can show immunity to the environment. Metals known to display this immunity are called noble metals like gold, silver and platinum. Immune behavior results from the metal being thermodynamically stable in the particular environment; that is, the corrosion reaction does not occur spontaneously. The change in the free energy (ΔG) is a direct measure of the work capacity or maximum electric energy available from a system. If the change in free energy accompanying the transition of a system from one state to another is negative, this indicates the spontaneous reaction direction of the system, if not, this indicates the immune behavior of the metal to environment. The free-energy change accompanying an electrochemical reaction can be calculated using the following equation.

$$\Delta G = -nFE \qquad (2.1)$$

Where, n is the number of electrons involved in the reaction, F is the Faraday's constant, and E is the cell potential.

Another possible behavior is that the metal will corrode, when exposed to the environment. In a specific environment, If the metal corrodes, it is described as active. When active behavior is observed, the metal dissolves in the solution and forms soluble, nonprotective corrosion products. Active corrosion is characterized by the weight loss of the metal. If the metal sample is weighed before and after exposing to the environment, a significant weight loss is measured and thus free energy change is negative. In some cases, although the metal is active, a state of passive behavior is observed. When the metal is immersed into the solution, it corrodes until a thin protective film, also reffered to as a passive film, forms, leading to the slowing down

the reaction rate to very low levels. All metals and alloys have a thin protective corrosion product film present on their surface resulting from reaction with the environment. For example when an iron or steel is immersed in aqueous environment hydrous ferrous oxide $(FeO.nH_2O)$ or ferrous hydoxide $[Fe(OH_2)]$ composes diffusion barrier layer next to the iron surface through which O_2 must diffuse, acting as protective corrosion layer role on the iron surface. The color of $Fe(OH_2)$, although white when the substance is pure, is normally green to greenish black because of incipient oxidation by air. At the outer surface of protective layer (oxide film), access to dissolved oxygen converts ferrous oxide to hydrous ferric oxide or ferric hydroxide $[Fe(OH_3)]$. Hydrous ferric oxide is orange to red-brown in color and makes up most of ordinary rust. It exist as nonmagnetic αFe_2O_3-hematite or as αFe_2O_3, the α form having the greater free energy of formation that means that the greater thermodynamic stability. A magnetic hydous ferrous ferrite, $Fe_3O_4.nH_2O$, often forms a black intermediate layer between hydrous Fe_2O_3 and FeO (Roberge 2000). Important iron-oxides and their colors that are very important for visual inspection, are listed in Table 2.1 (Cornell and Schewertmann 1996). When a stainless steel is immersed in aqueous environment, for another example, passivity is caused by an ultra-thin surface protective film (1 to 2 nm thick). The passive film on stainless steel has its own composition that is strongly enriched in chromium. When the chromium content is above 10.5% the corrosion product film changes from an active film to a passive film. While the active film continues to grow over the time in the corroding solution until the base metal is consumed, the passive film will form and stop growing. For an alloy containing 15% Cr in its bulk composition, the chromium content in the top layer of passive film can be high as 80%.(Qiu 2002). An interesting observation for the nickel containing stainless steel is that nickel is actually depleted in the passive film and in some cases is found to be enriched in the metallic form immediately beneath the passive film (Cumpson 1993, Seah 1994). The principal constituents of the passive film include metal cations from the substrate with a high affinity for oxygen. The most common cations are Cr^{+3} and Fe^{+3}, although ferrous ions Fe^{+2} are also possible. The cations become associated with water molecules from the surrounding solution. Some of these water molecules lose protons into the solution to balance the positive charges on the cations by the creation of hydroxyl (OH^-) and oxide (O_2^-). The passive film on stainless steel is of the "double layers" type, with an inner layer of $(Fe, Cr)_2O_3$ oxide in contact with the substrate and an external layer essentially composed of hydrated hydroxides of the type $Cr(OH)_3.nH_20$ (Cunat 2000).

Table 2.1. Iron oxides names, formula and colors (Cornell and Schwertmann 1996).

Name	Chemical formula	Colour
Goethite	α-FeOOH	Yellow-brown
Lepidocrocite	γ-FeOOH	Orange
Akaganéite	β-FeOOH	Brown to bright yellow
	δ-FeOOH	Red-brown
Feroxyhyte	δ'-FeOOH	Red-brown
	High pressure FeOOH	
Ferrihydrite	$Fe_5HO_8 \cdot 4H_2O$	Reddish brown
Bernalite	$Fe(OH)_3$	Greenish
	$Fe(OH)_2$	White
Schwertmannite	$Fe_{16}O_{16}(OH)_y(SO_4)_z \cdot nH_2O$	Yellow
Haematite	α-Fe_2O_3	Red
Magnetite	Fe_3O_4	Black
Maghemite	γ-Fe_2O_3	Red-brown
	β-Fe_2O_3	
	ε-Fe_2O_3	
Wüstite	FeO	Black

If such films did not exist on metallic materials exposed to the environment, they would revert back to termodynamically stable condition of their origin as indicated before. The phenomenon of passivity is therefore a critical element controlling corrosion process and usually four conditions are required for breakdown of passive film that initiates localized attack like pitting (Hoar 1967):

1) A certain critical potential must be exceed.

2) Damaging species like chloride or the higher atomic weight halides are needed in the environment to initiate breakdown.

3) An induction time exists, which starts with the initiation of the breakdown process by the introduction of breakdown conditions and ends when the localized corrosion density begins to rise.

4) The presence of highly localized sites where breakdown takes place.

2.1.1 Potential-pH Diagrams

Potential-pH diagrams present a map of the regions of the stability of a metal and its corrosion products in aqueous environments. The diagrams identify conditions under which the metal is stable and will not corrode, soluble reaction products are formed and corrosion will occur and insoluble reaction products are formed and passivity will occur. The diagrams are generated from thermodynamic calculations. These diagrams are also called Pourbaix diagrams in the honor of Marcel Pourbaix, a

Belgian scientist credited with the development and wide use of these diagrams (Davis 2003). For corrosion in aqueous media, two fundemental variables, namely corrosion potential and pH, are particularly important. Changes in other variables, such as the oxygen concentration, tend to be reflected by changes in the corrosion potential. To draw potential-pH diagrams for an system, it is necessary to determine the potential of a system in which the reactants are not at unit activity like almost all systems, the familiar Nerst equation can be employed for this; that is,

$$E = E_0 + 2.3 \frac{RT}{nF} \log \frac{a_{oxid}}{a_{red}} \qquad (2.2)$$

where, E is the half-cell potential (V), E_0 the standart half-cell potential (V), R is the gas constant (8.314 j.mol^{-1}.K^{-1}), T is absolute temperature (K), n is the number of electrons transferred, F is the Faraday constant (96487 C.mol^{-1}), a_{oxid} and a_{red} are the concentrations of oxidized and reduced species. Half-cell potential is not only used for drawing potential-pH diagrams, it is also used to calculate free-energy change for a system. As seen Nerst equation, standart haf-cell potential must be determined in order to calculate half-cell potential. In order to understand how an standart half-cell potential can be determined for example for an zinc and iron system, it can be constructed an electrochemical cell containing iron and zinc electrodes in equilibrium with their ions at 25 ^{0}C seperated by a porous membrane to retard mixing, as illustrated in Figure 2.2. For purposes of simlicity, the concentrations of metal ions are maintained at unit activity; each solution contains 1 gram-atomic weight of metal ion per liter. These reactions will occur in that system for each cell;

Zn $= Zn^{2+} + 2e$; $Fe^{2+} + 2e = Fe$
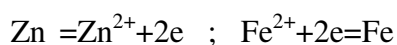
The reaction rates of metal dissolution and deposition in each cell must be the same; there is no net change in the system. These electrodes are called half-cell, and when the concentarions of all reactants are maintained at unit activity, they are termed standart half-cells. If a high-resistance voltmeter is connected to between the iron and zinc electrodes, a potential difference of appriximately 0.323 volts is measured. This is the cell potential that is used in determining free energy of the overall electrochemical reactions (Fontana 1987).
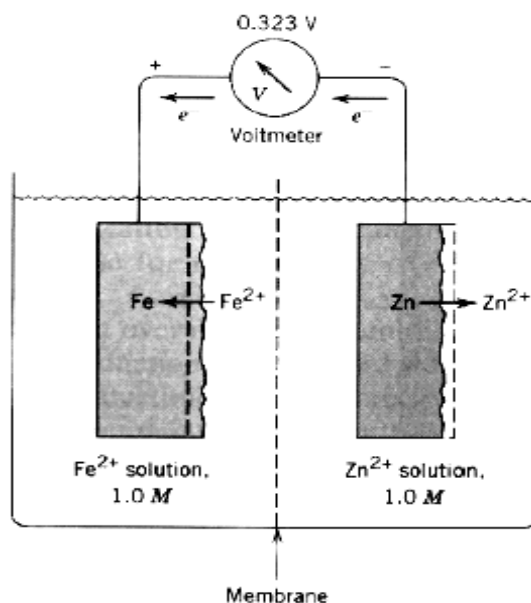
Figure 2.2. Reversible cell containing iron and zinc in equilibrium with their ions.

If a platinum inert electrode was used in 1M solution of H^+ instead of zinc electrode, standart half-cell potential would has been read at voltmeter as –0.440 volt for iron. Standart half-cell potentials are referenced against the hydogen electode, which is arbitrarily defined zero like platinum electrode are given Figure 2.3 for the 25 ^0C electrolyte temperature.

Figure 2.4 shows the potential-pH diagram of water with no metal involved. In between the two diagonal lines marked as *a* and *b* in this figure is the region of the stability of water as a function of potential and pH. At any conditions of potential and pH below the line *a,* water is thermodynamically unstable with respect to the generation of hydrogen gas and at any conditions of potential and pH above line *b*, water is thermodynamically unstable with respect to the evolution of oxygen. For potential and pH conditions between lines *a* and *b*, water is thermodynamically stable. Line *a* represents the equilibrium for the reaction of hydrogen ions to evolve hydogen gas as,

$$2H^+ + 2e^- \rightarrow H_2$$

The electropotential of above reaction using the Nerst equation is ;

$$E = 0.00 - 0.059\,pH \qquad\qquad (2.3)$$

The potential at pH=0 is 0 V, and the potential decreses by 0.059V for each unit increase in pH. At any potential and pH below this line, the hydrogen ion in water will react with electrons to evolve hydrogen gas.

	Electrode Reaction	Standard Electrode Potential, V^0(V)
	$Au^{3+} + 3e^- \longrightarrow Au$	+1.420
	$O_2 + 4H^+ + 4e^- \longrightarrow 2H_2O$	+1.229
	$Pt^{2+} + 2e^- \longrightarrow Pt$	$\sim$+1.2
Increasingly inert	$Ag^+ + e^- \longrightarrow Ag$	+0.800
(cathodic)	$Fe^{3+} + e^- \longrightarrow Fe^{2+}$	+0.771
	$O_2 + 2H_2O + 4e^- \longrightarrow 4(OH^-)$	+0.401
	$Cu^{2+} + 2e^- \longrightarrow Cu$	+0.340
	$2H^+ + 2e^- \longrightarrow H_2$	0.000
	$Pb^{2+} + 2e^- \longrightarrow Pb$	−0.126
	$Sn^{2+} + 2e^- \longrightarrow Sn$	−0.136
	$Ni^{2+} + 2e^- \longrightarrow Ni$	−0.250
	$Co^{2+} + 2e^- \longrightarrow Co$	−0.277
	$Cd^{2+} + 2e^- \longrightarrow Cd$	−0.403
	$Fe^{2+} + 2e^- \longrightarrow Fe$	−0.440
Increasingly active	$Cr^{3+} + 3e^- \longrightarrow Cr$	−0.744
(anodic)	$Zn^{2+} + 2e^- \longrightarrow Zn$	−0.763
	$Al^{3+} + 3e^- \longrightarrow Al$	−1.662
	$Mg^{2+} + 2e^- \longrightarrow Mg$	−2.363
	$Na^+ + e^- \longrightarrow Na$	−2.714
	$K^+ + e^- \longrightarrow K$	−2.924

Figure 2.3. Standart half-cell electrode potentials vs. normal hydrogen electrode at 25 ^{o}C.
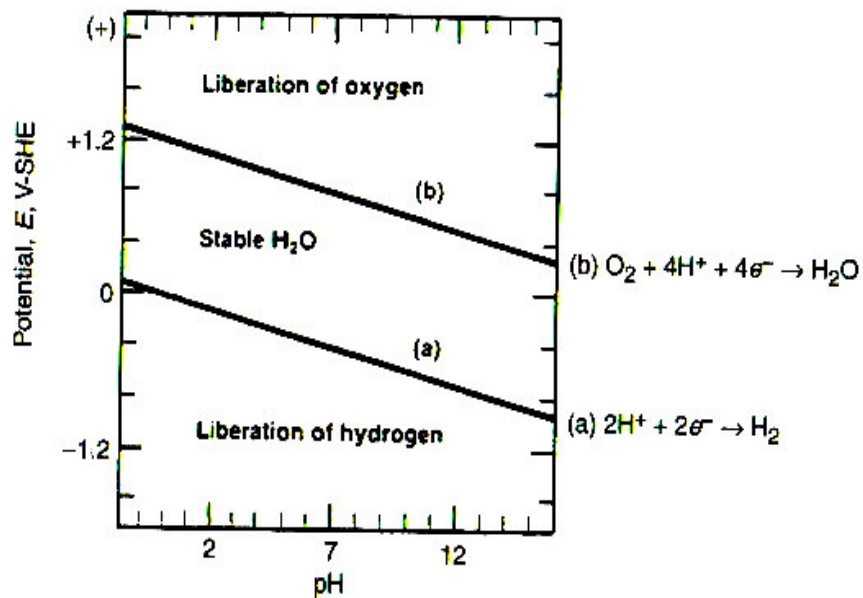
Figure 2.4. Potential-pH diagram for water (Davis 2003).

Line *b* represents the equilibrium of oxygen plus hydrogen ions and electrons to form water as,

$$O_2 + 4H^+ + 4e^- \rightarrow H_2O$$
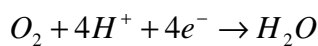
The equation for electropotential is,

$$E = 1.229 - 0.059\,pH$$

21

When pH=0, the potential is +1.229 V as seen Figure 2.3 and it decreases by 0.059 V for every unit increase in pH. Above the line *b* the oxidized species are stable, and water under those conditions reacts spontaneously to produce oxygen and hydrogen ions. Thus, if a metal electrode is at a potential and pH below line *a*, hydrogen bubbles will evolve on the metal surface and similarly, for any metalelectrode potential-pH conditions above line *b*, the oxygen gas will evolve. For any potential-pH condition between lines *a* and *b*, water is thermodynamically stable and no gas evolution will occur (Davis 2003).

The observed corrosion behaviors of a particular metal or alloy can be superimposed on E-pH diagrams. Such a superposition is presented in Figure 2.5 for iron. The E-pH ranges of sea, natural and fresh waters derived from experimental data are also included in the same figure as a rectangular box. Many phenomena associated with corrosion damage to iron-based alloys in water at elevated temperature can also be rationalized on the basis of iron-water E-pH diagrams (Roberge 2000). Hot water heating systems like geothermal district heating systems for buildings are relevant practical examples. An excellent detailed account of corrosion damage to steel in the hot water flowing through the radiators and pipes has been published by Jones in 1993. He investigated the corrosion bevahior of iron in the pH range of 6.5 to 8 in main water, of which the E-pH diagrams are shown in Figures 2.6(a) and (b). It has been understood that minimal corrosion damage is expected if the corrosion potential remains below – 0.65V. As seen Figure 2.6, for a given corrosion potential, the hydrogen evolution is thermodynamically more favorable at low pH values. The position of the oxygen reduction lines indicates that the cathodic oxygen reduction reaction is thermodynamically very favorable. The oxygen content is an important factor in determining corrosion rates at kinetic considerations. The oxygen content of the water is usually minimal, since the solubility of oxygen in water decreases with increasing temperature as seen in Figure 2.7, and any oxygen remaining in the hot water is consumed over time by the cathodic corrosion reaction. The undesirable oxygen pickup is possible during repairs because of the additions of fresh water in order to prevent pressure loss at closed hot water pipelines and design faults that lead to continual oxygen pickup from the expansion tanks. The higher oxygen concentration shifts the corrosion potential to higher levels and $Fe(OH)_3$ fields comes into play at these high potential levels increasing the potential of severe or mild pitting as shown in Figure 2.5 (Roberge 2000) .
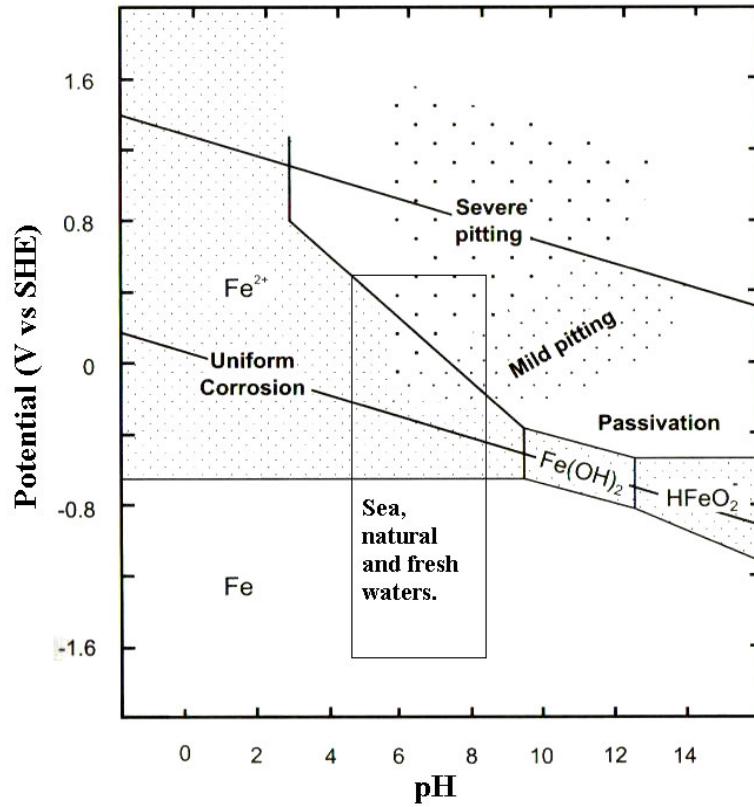
Figure 2.5. Thermodynamic boundaries of the types of corrosion observed on steel and E-pH ranges for water environments (Roberge 2000, Davis 2003)

(a)   (b)
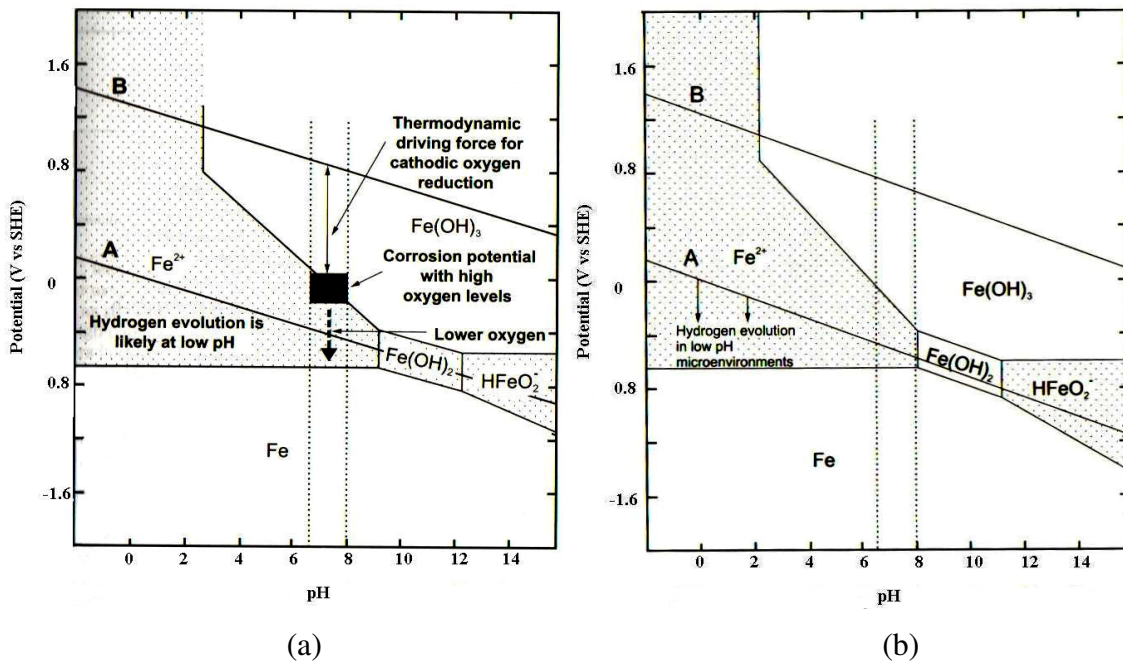
Figure 2.6. (a) E-pH diagram of iron in water at 25 ^{0}C, (b) E-pH diagram of iron in water 85 ^{0}C (Jones 1993).
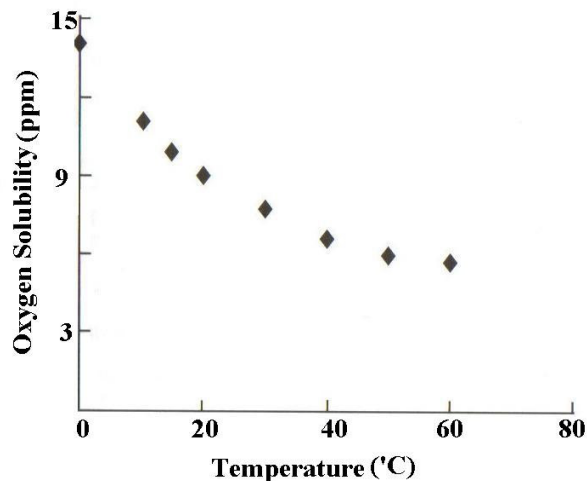
Figure 2.7. Solubility of oxygen in water in equilibrium with air at different temperatures (Roberge 2000).

2.2. Electrochemical Reactions of Corrosion

Corrosion is either chemical or electrochemical in nature. The distinction between chemical and electrochemical corrosion is based on the corrosion causing mechanism. Chemical and electrochemical corrosion are not mutually exclusive and can occur simultaneously. Chemical corrosion is the direct result of exposure of a material to a chemical and is governed by the kinetics of chemical reactions. Chemical corrosion does not involve the generation of an electrical current. Direct chemical attack, such as the dissolutive of a material by an acid, and selective attack, such as leaching of a specific soluble compound from a material, are two common forms of chemical corrosion. Electrochemical corrosion is the dissolution of a metal through the oxidation process. Oxidation and reduction reactions occur simultaneously and are interdependent. Corrosion only occurs at the site of oxidation reactions (Degiorgi 2000).

Corrosion of metals in aqueous environment is almost always electrochemical in nature. Corrosion process requires anodes and cathodes in electrical contact and an ionic conduction path through an electrolyte, and corrosion occurs once electrons flow between the anodic and cathodic areas (Zheng 2000). The characteristics of an electrochemical reaction can be illustrated by considering the behavior of iron in hydrochloric acid. Iron reacts vigorously with HCl; hydrogen is evolved and iron gradually goes completely into solution. The reaction is:

$$F_e + 2HCl \rightarrow FeCl_2 + H_2$$
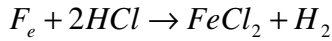
This equation can be written as the following:

$$Fe + 2H^+ + 2Cl^- \rightarrow Fe^{2+} + 2Cl^- + H_2$$
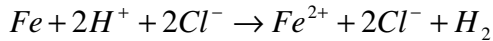
The solid iron gradually disappears and a gas is evolved. The iron converted to an iron with two positive charges. The iron is oxidized. On the other hand, the hydrogen ions have each gained an electron, thus, they have been reduced. The overall reaction can be considered as two seperate ones:

$$F_e \rightarrow Fe^{2+} + 2e^- \text{ (oxidation)}$$

$$2H^+ + 2e^- \rightarrow H_2 \text{ (reduction)}$$
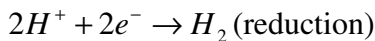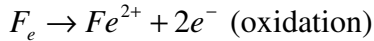
The mechanism for the preceding case is shown schematically in Figure 2.8. The areas where oxidation occurs are defined as anode, and those where reduction takes place are defined as cathode. An electrical potential exists between the anode and cathode areas. A complete electrical circuit exists, and a current flows from anode to cathode. The faster the solid is converted to iron ions means that greater corrosion, the larger is the current flowing in this corrosion cell. Therefore, the possible anodic reactions in a system are relatively easy to predict. With cathodic reactions, there are more possibilities. The most common are:

$$2H^+ + 2e \rightarrow H_2 \text{ ....Hydrogen evolution.}$$

$$O_2 + 4H^+ + 4e \rightarrow 2H_2O \text{ ....Oxygen reduction (acid solutions).}$$

$$O_2 + 2H_2O + 4e \rightarrow 4OH^- \text{ ....Oxygen reduction (neutral solutions).} \quad (2.4)$$

$$M^{3+} + e \rightarrow M^{2+} \text{ ....Metal ion reduction.}$$

$$M^+ + e \rightarrow M \text{ ....Metal deposition.}$$
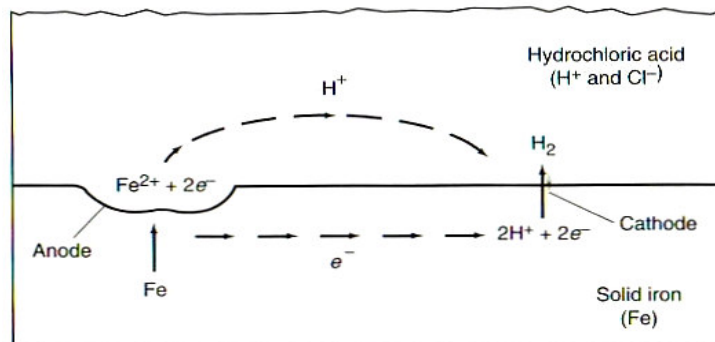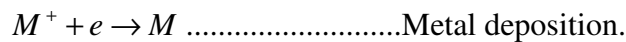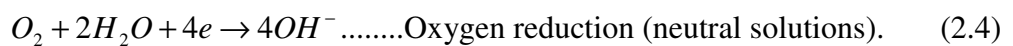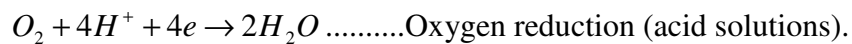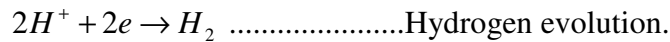
Figure 2.8. Schematic representation of corrosion of iron in hydrochloric acid.

2.3.   Many Forms of Corrosion

Corrosion problems can be divided into nine categories based on the appearance of the corrosion or the mechanism of attack. These are:

1-Uniform corrosion

2-Pitting corrosion

3-Crevice corrosion

4-Galvanic corrosion

5-Erosion-corrosion

6-Intergranular corrosion

7-Stress corrosion cracking

8-Dealloying

9-Biocorrosion

Many corrosion problems are due to more than one form of corrosion acting simultaneously. For instance, pitting corrosion may be caused by crevice corrosion, deposit corrosion, cavitation or fretting corrosion. Additionaly, in some metal systems where dealloying may occur, this form of corrosion may be a precursor to stress-corrosion cracking. Similarly, deep pits can act as stress raisers and serve as nucleation sited for corrosion fatigue failures.

2.3.1 Uniform Corrosion

Uniform corrosion, or general corrosion, is a corrosion process exhibiting uniform thinning that proceeds without appreciable localized attack. It is the most common form of corrosion and may appear initially as a single penetration, but with thorough examination of the cross section it becomes apparent that the base material has uniformly thinned. Uniform chemical attack occurrs in the atmosphere, solutions, and soil, frequently under normal service conditions. Excessive attack can occur when the environment has changed from that initially expected. Weathering steels, magnesium alloys, zinc alloys, and copper alloys are examples of materials that typically exhibit general corrosion. Passive materials, such as stainless steels, aluminum alloys, or nickel-chromium alloys are generally subject to localized corrosion. Under specific conditions, however, each material may vary from its normal mode of corrosion.

Uniform corrosion commonly occurs on metal surfaces having homogeneous chemical composition and microstructure. Access to the metal by the attacking environment is generally unrestricted and uniform. Any gradient or changes in the attacking environment due to the corrosion reaction or stagnancy can change the degradation mode away from uniform corrosion. At the microlevel, uniform corrosion is found to be an electrochemical reaction between adjacent closely spaced microanodic and microcathodic areas. Consequently, uniform corrosion might be considered to be localized electrolytic attack occurring consistently and evenly over the surface of the metal. This is well illustrated in binary alloys that contain phases of differing corrosion potentials. The grain in one phase becomes anodic to grain in the second phase in the microstructure, thus producing an electrolytic cell when the proper electrolyte is present. Another illustration is ductile cast iron, where there are three compositionally different phases within the material: ferrite, pearlite, and graphite. The corrosion process will initiate as uniform corrosion with the formation of an electrolytic microcell between the graphite cathode and ferrite or pearlite anode. The process can turn into a pitting mechanism if the microcells develop enough to produce acidic gradients (Kent 2000). In the case of only ferrite and perlite structure, the adherence of the corrosion product film has often been related to the presence of iron carbide. The carbide phase strengthens the film and anchors it to the steel substrate, so the size and distribution of carbides become very important (Lopez et al. 2002). The term corrosion rate refers to the effect of uniform corrosion on a metal (or nonmetal) per unit of time. Corrosion rate can be expressed as the mass of metal turned into corrosion products per unit area of surface per unit of time or an increase in corrosion depth per unit time. The rate of metal removal due to corrosion is calculated from:

$$R = \frac{K \times W}{A \times T \times d} \tag{2.5}$$

where, R is the corrosion rate, K is a constant, W is weight loss in gram to the nearest mg, A is the area to the nearest 0.01 cm^2, T is time of exposure in hours to the nearest 0.01 hours, and d is the density in g/cm^3. Many different units are used to express the corrosion rate. Using the preceding units for W, A, T and d, the corrosion rate can be calculated in a variety of units with the appropriate value of constant "K" as shown Table 2.2.

Table 2.2. Constants to calculate corrosion rate units desired (Davis 2003).

Corrosion Rate Units Desired (mpy)	Constant (K) in Corrosion Rate Equation
Mils per year (mpy)	$3,45 \times 10^6$
Inchs per month (ipm)	$2,87 \times 10^2$
Milimeters per year (mm/yr)	$8,76 \times 10^4$
Micrometers per year (mm/yr)	$8,76 \times 10^7$
Grams per square meter per hour ($g/m^2/hr$)	$1,00 \times 10^4 \times d$ (*)
(*) Density is not needed to calculate corrosion rate in this unit. The density in the constant K cancels out the density in the corrosion rate equaiton.	

Most widely used corrosion rate expression is milimeters per year. This unit can be calculated as,

$$\text{Corrosion Rate (mm / yr)} = \frac{87.6 \times W}{d \times A \times T} \qquad (2.6)$$

By knowing the expected general corrosion rate and the anticipated plan for service life of a part, the designer can calculate the extra wall thickness required for corrosion resistance of the process equipment being designed. After determining a wall thickness that meets mechanical requirements, such as pressure and weight of equipment, an extra thickness called a corrosion allowance is added to the wall thickness to compansate for the metal expected to be lost over the life of the equipment. Because the penetration depth can vary, a corrosion allowance is assigned a safety factor of 2.

2.3.1.1 Some Important Environmental Effects for Uniform Corrosion

The investigations showed that the uniform corrosion rate of steel in seawater increases with increasing the velocity of the water until a critical velocity is reached, beyond which there is further increase in corrosion rate. This behavior is noted to be different from that in fresh waters, where corrosion rate decreases above the critical velocity due to the passivation. In seawater, passivity is not formed at any velocity because of high concentrations of Cl⁻ ions. When the velocity increses above a critical value, the corrosion rate of steel markedly increases because of erosion-corrosion, even

in the absence of solid particles. The critical velocity depends on the state of flow, but some investigations showed that the critical velocity was about 20m/s (Ichikawa et al. 1973). At areas where flow is disturbed like bends or joints in piping, erosion-corrosion may occur at much lower velocities. The expected maximum uniform corrosion rate of carbon steel piping by seawater under velocities up to 4m/s is 1 mm/year (40 mpy) approximately, but above this velocity, erosion-corrosion occur at areas of flow disturbance (Matsushima 1992a). The effect of fresh water velocity on corrosion of mild steel was also investigated (Matsushima 1992b). The critical velocity above which the corrosion rate decreases because of the passivation is in the range of 0.3-0.7 m/s as shown Figure 2.9.
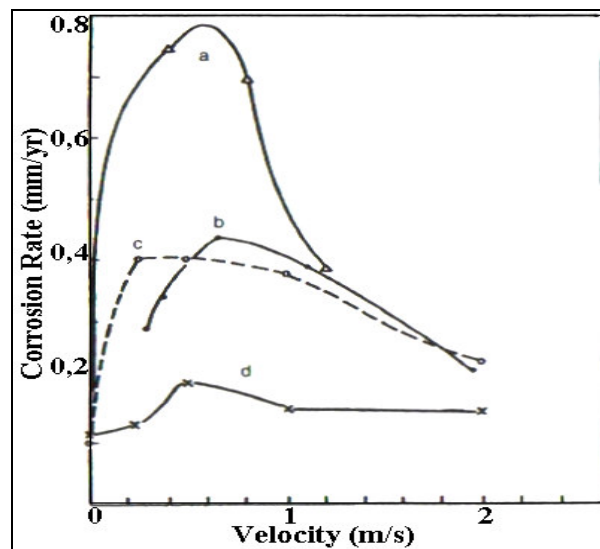
Figure 2.9. Effect of water velocity on corrosion of carbon steel. (a) Distilled water +10 ppm Cl⁻ , 50 ^{0}C, 14 days. (b) Soft tap water, Tokyo, Japan, room temperature, 67 days. (c) Soft tap water, Amagasaki, Japan, 20 ^{0}C, 15 days (killed steel). (d) Soft tap water, Amagasaki, Japan, 20 ^{0}C, 15 days (rimmed steel) (Matsushima 1992b)

The critical velocity and the corrosion rate at velocities above the critical depend on the concentration of chloride ions that prevent passivation. An example of effect of Cl ion concentration on the critical velocity and corrosion rate of a carbon steel is shown in Figure 2.10 (Herce et al. 1995). An increase in temperature may increase the corrosion rate. However, oxygen solubility decreases as the temperature increases and, in an open system, may approach zero as water boils. Beyond a critical temperature level, the corrosion rate may decrease due to a decrease in oxygen solubility. However, in a

closed system, where oxygen cannot escape, the corrosion rate may continue to increase with an increase in temperature. For those alloys, such as stainless steel, that depend on oxygen in the environment for maintaining a protective oxide film, the reduction in oxygen content due to an increase in temperature can accelerate the corrosion rate by preventing oxide film formation.
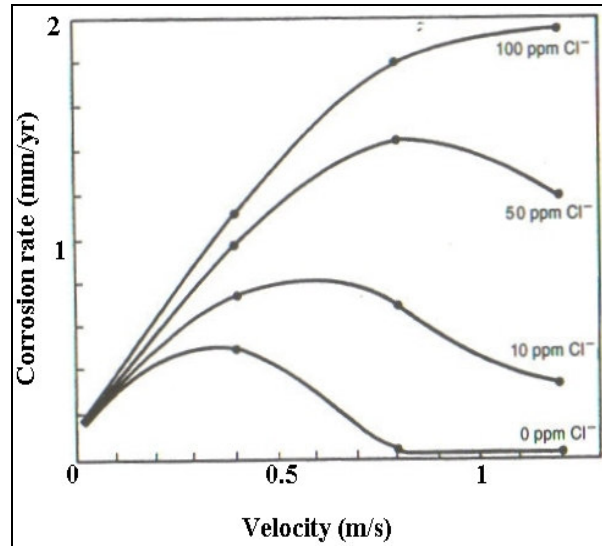
Figure 2.10. Effect of water velocity and chloride concentrations on corrosion of carbon steel. Distilled water+NaCl, 50 ^{0}C, 14 days (Herce 1995).

Temperature can affect corrosion potential by causing a salt dissolved in the environment to precipitate on the metal surface as a protective layer of scale. One example is calcium carbonate scale in geothermal waters. Temperature can also affect the nature of the corrosion product, which may be relatively stable and protective in certain temperature ranges and unstable and non-protective in others (AAH 1999).

2.3.2 Pitting Corrosion

Pitting corrosion is a localized form of corrosion by which cavities, or holes, are produced in the material. Pitting is considered to be more dangerous than uniform corrosion damage because it is more difficult to detect, predict, and design against. Pits usually grow in the direction of gravity. Most pits develop and grow downward from horizontal surfaces. Pitting corrosion may form in different shapes and can be divided into two group as through and sideway pits as depicted in Figure 2.11 (Web_2 2005).

The tendency of pits to undercut the surface, as seen in Figure 2.11, makes their detection and measurement difficult. Pitting is an autocatalytic; the corrosion process within a pit produces conditions, which are both stimulating and necessary for the continuing activity of the pit. Pitting is sometimes difficult to detect in laboratory tests and in service because there may be a period of months or years before the pits intiate and develop to a visible size. Delayed pitting sometimes occurs after an unpredictable period of time in service, when some change in the environment causes local destruction of a passive film. Immediately after a pit has initiated, the local environment and any surface films on the pit-initiation site are unstable, and the pit may become inactive after just a few minutes if convection currents sweep away the locally high concentration of hydrogen ions, chloride ions, or other ions that initiated the local attack. The stainless steel alloys are more suspectible to damage by pitting corrosion than are any other group of metals or alloys. The effects of alloying elements on the pitting resistance of stainless steel alloys are tabulated in Table 2.3. One way of combining the effect of alloying elements is via the so-called "Pitting Resistance Equivalent- (PRE)" which takes into account the different effects of chromium, molybdenum and nitrogen.
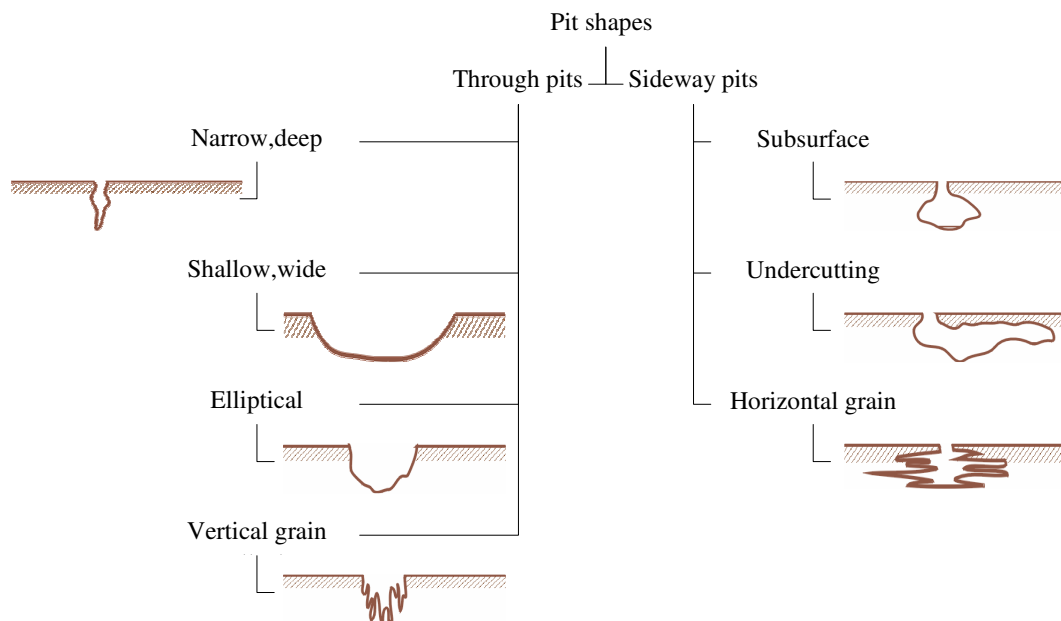
Figure 2.11. Most observed pit shapes.

One of the most commonly used formula for the pitting resistance equivalent is the following:

$$PRE = \%Cr + 3.3 \times \%Mo + 16 \times \%N \qquad (2.7)$$

Above formula is widely used for the duplex steels but it is occasionally also applied to austenitic stainless steels. The difference between the formulas is generally small but the higher coefficient for nitrogen will give a difference in the PRE value for the nitrogen alloyed grades. Pitting resistance equivalent provides a good qualitative indication of the comparative pitting resistance of different alloys, but can not be easily used to quantitative prediction of performance in relation to a particular corrosive environment (Bela 1996). Pitting is a serious corrosion in heat exchangers since they have thin walls and large surface area and even a single pinhole perforation may constitute a failure. An example of the pitting corrosion failure of an AISI-316 type austenitic stainless steel heat exchanger is shown in Figure 2.12, in which the exchanger is considered to be failed due to the pinhole perforation.

Table 2.3. Effects of alloying on pitting resistance of stainless steel alloys (Fontana 1987)

Element	Effect on pitting resistance.
Chromium	Increases.
Nickel	Increases.
Molybdenum	Increases.
Silicon	Decreases; increases when present with molybdenum.
Titanium and Columbium	Decreases resistance in $FeCl_3$; other mediums no effect.
Sulfur and Selenium	Decreases.
Carbon	Decreases, especially in sensitized condition.
Nitrogen	Increases.

Pits due to pitting corrosion of steel and iron usually occur by the action of macrogalvanic cells. This is usually formed by bimetallic contact, an inhomogeneous steel matrix (typically at welded joints), discontinuous surface films, differential aeration, and differential pH caused by combinations of an alkaline and a near-neutral environment that leads to the formation of passive-active cells. In a macrogalvanic cell, the anodic and cathodic areas are macroscopic, and their locations are fixed, whereas in

a microgalvanic cell the anodic and cathodic sites are microscopic and their locations change randomly with time.

Figure 2.12. Pits on the surface of a stainless heat exchanger.

Bimetallic contact is based on galvanic corrosion principles and it tends to accelerate localized attack caused by some other types of macrogalvanic cells. Another reason for pitting is the discontinuous surface films. Steel corroded in water and covered with corrosion products may undergo localized corrosion if the corrosion products are removed repeatedly from a fixed area of relatively small size. Corrosion product films protect the underlying steel from corrosion to some extent by acting as a barrier layer against the corrosive environment. If this barrier layer is damaged at a fixed area repeatedly, so that the steel surface is exposed to the environment, the penetration rate at the exposed area increases. Because the surface covered with corrosion products tends to be noble than the exposed steel, the former acts as the cathode of the macrogalvanic cell.

Another important example of localized corrosion caused by differential aeration in water is associated with the formation of tubercles (Matsushima 1992c). A schematic of tubercle structures formed on steel in oxygenated waters is shown in Figure 2.13. Tubercle structures or oxygen concentration cells may be initiated by anything that will shield a small area from the dissolved oxygen in the water, such as a grain of sand or a microbial colony. Once started, the cell becomes self-perpetuating. A pit forms that is covered with a crust of metal oxide, assuring there will be no oxygen under the tubercle. When the corroding metal is iron or steel, an additional reaction occurs. The ferrous ions produced are oxidized to ferric hydroxide:

$$Fe(OH)_2 + \frac{1}{4}O_2 + \frac{1}{2}H_2O \rightarrow Fe(OH)_3$$
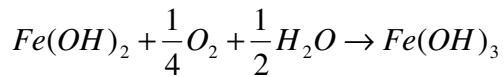
The interior of a tubercle contains a solution of ferrous chloride and sulfate ions in concentrations greater than those in the water. The solution is slightly acid and covered by a black inner crust consisting of hydrous Fe_3O_4, which, being magnetic, is attracted to the iron to form porous columnar fibers. The outer crust consists of reddish brown ferric hydroxide or hydrated ferric oxide. The flow of current protects the metal in the immediate vicinity of the pit. In ferrous metals, pits generally become inactive after a period of time. When this occurs, they no longer protect the metal in their vicinity, and new pits develop. Apparently the tubercles become so impermeable that ions cannot diffuse through, and since the solution inside must maintain electrical neutrality, no additional iron ions are formed (Rossum 1998).
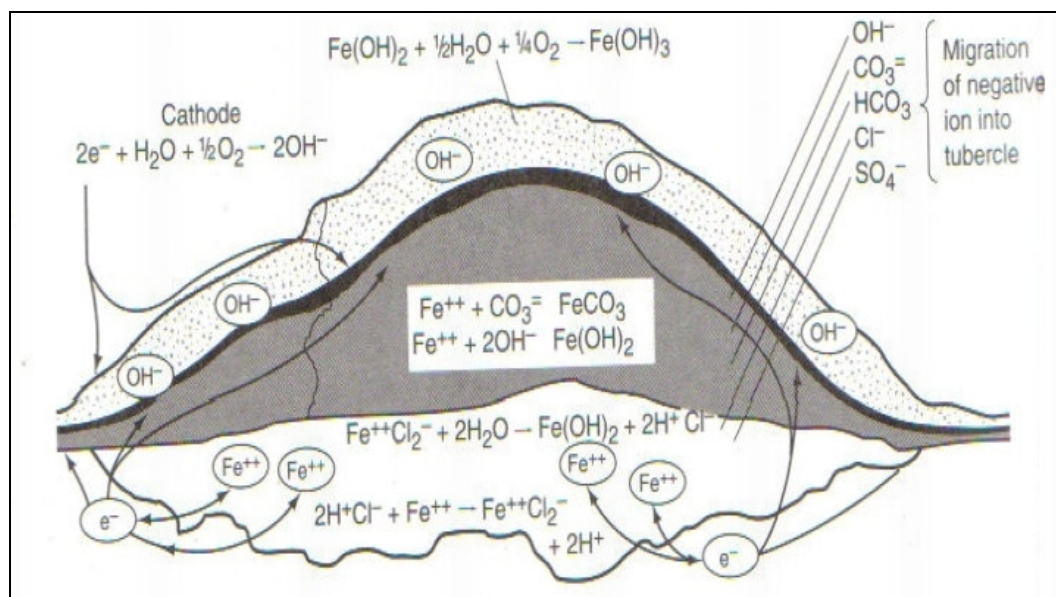
Figure 2.13. Schematic of tubercle structures formed on steel in oxygenated waters.

Pit depth is usually measured by microscopic methods or by using mechanical devices. Results are usually reported as the maximum pit depth, number of pits per unit area, average pit depth or average of a selected number of the deepest pits. Coupons of relatively small area are used and tested in a relatively short time in a laboratory. During plant operation, much larger surface of the plant is exposed to the corrosive environment during longer operation times. Extreme value statistics using Gumbel distribution is quite useful for estimating the maximum pit depth and its dependence on surface area. Gumbel distribution presents a graphical or minimum variance linear

unbiased estimation method to estimate the maximum depth of pits over the larger surface area from which specimens of small area are extracted (Shibata 1992).

2.3.2.1. Environmental Effects for Pitting Corrosion

Slow-moving and stagnant waters can prevent, damage, or remove passive films. The low velocity allows loosely adherent solid corrosion products to form on metal surfaces and allows to debris collect, which facilitates further corrosion damage. In closed systems as geothermal systems, if a corrosion inhibitor is used, it is effectiveness is often reduced where the water is stagnant or quiet. In the case of high velocity, water may carry dissolved metal ion away from corroding areas before the dissolved ions can be precipitated as protective layer. Gritty suspended solids in water occur metal surfaces and continually expose fresh metal to corrosive attack. As water velocity increases, it is expected that corrosion of steel first increases, then decreases, and then increases again. The latter occurs because erosive action serves to break down the passive state. Thus, increase in the water velocity increases the uniform corrosion rate of metals, on the other hand, it is expected that pitting will act an important role in the stagnant waters (Colin et al. 2000). From a practical standpoint, most pitting failures are caused by chloride and chlorine-containing ions. Chlorides are present in varying degrees in most waters and solutions made with water. A special study done by Efird and Moller in 1978 in fresh water resources showed the critical chloride contents as function of temperature necessary to form pitting type corrosion in 304 and 316 type austenitic stainless steels (Figure 2.14) (Effird and Moller 1981).

The mechanisms for pitting by chlorides have not been well understood. One explanation is the acid-forming tendency of chloride salts and the high strength of its free acid (HCl), leading to localized corrosion. Three factors influence the pitting corrosion: chloride content, pH, and temperature. In general, the higher the temperature and chloride content and the lower the pH, the greater the probability of pitting. As chromium is added to the stainless steels, a rapid reduction in corrosion rate is observed to around 10% because of the formation of this protective layer or passive film. In order to obtain a compact and continuous passive film, a chromium content of at least 11% is required. Passivity increases fairly rapidly with increasing chromium content up to about 17% chromium. Many studies about pitting of austenitic stainless

steels and environment have showed an relationship between pH, chloride content of water, molybdenum content of stainless steel and proofed that increase on chloride content and decreased pH of water need much more molybdenum content to prevent pitting initiation (Web_3 2005).
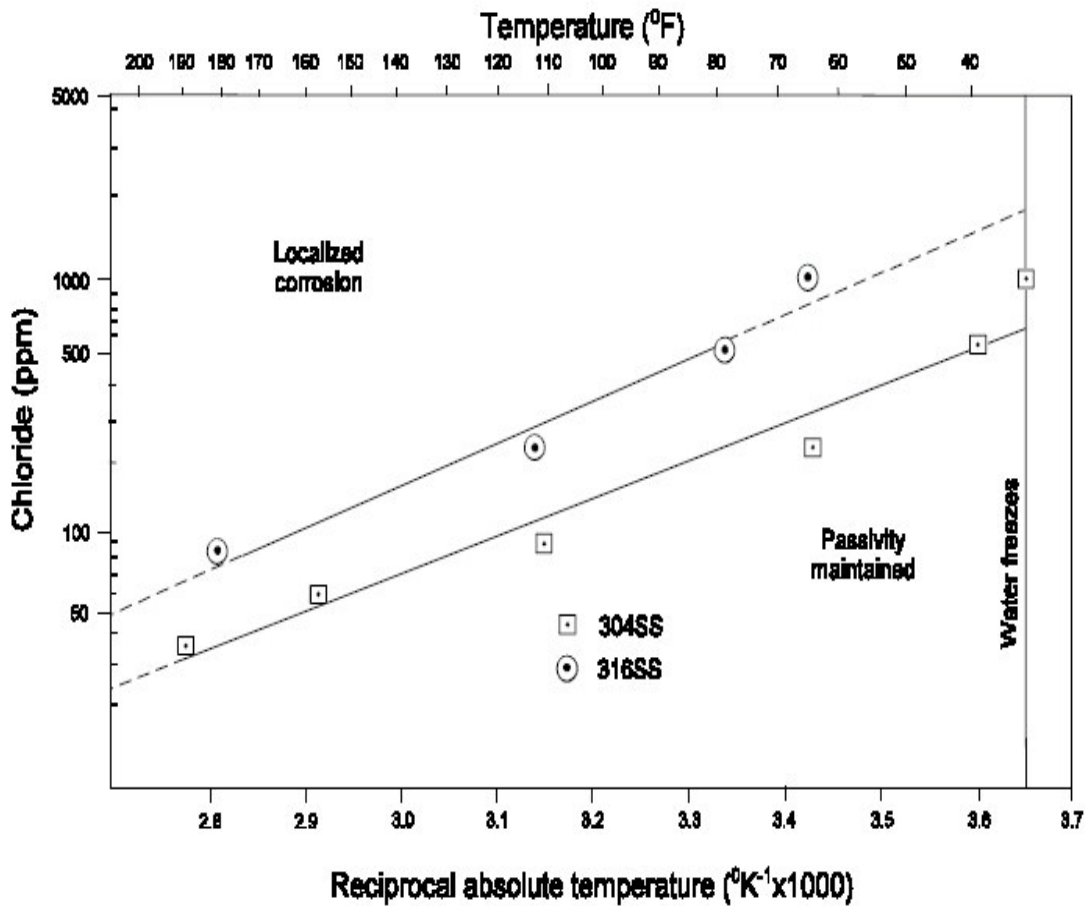
Figure 2.14. Chloride required to produce localized corrosion of type 304-316 stainless steels as a function of temperature (Efird and Moller 1978).

2.3.3. Crevice Corrosion

Crevice corrosion is a form of localized attack that occurs at narrow openings or spaces between metal to metal or nonmetal-to metal components. It is similar to pitting but it differentiates by the place of origination. It occurs in geometrically confined spaces such as crevices where tube and tube sheets join, where the plate ridges of flat plate heat exchangers overlap or under scale deposits. The differential aeration cell is the main part that takes place in this corrosion reaction. At crevices, the difference in

oxygen concentration produces a potential difference and causes current to flow. This accounts for pronounced damaged formed at the interface of two coupled pipes or at threaded connections. It also accounts for pitting damage under rust.

Crevices may be produced by design or accident. Crevices caused by design occur at gaskets, flanges, robber O-rings, washers, bolt-holes, rolled tube ends, threaded joints, riveted seams, overlapping screen wires, lap joints, beneath coatings or insulation, and anywhere close-fitting surfaces are present (Davis 2003).

2.3.4. Galvanic Corrosion

Galvanic corrosion is the accelerated corrosion of one metal (more active one in galvanic series) resulting from its electrical contact with another (passive metal in galvanic series). A galvanic corrosion caused by the galvanic action between an AISI-304 type austenitic stainless steel (spring part), which is nobler, and an St-37 type carbon steel (body part) taken from Balçova-Izmir geothermal system, is showed in Figure 2.15. Pitting caused by galvanic action is clearly seen in this figure on the surface of carbon steel pipe part of compensator.

Figure 2.15. Corrosion caused by the galvanic effect on a compensators taken from Balçova-Izmir geothermal system.

The factors that influence galvanic corrosion include conductivity of the circuit, potential between anode and cathode, polarization, relative areas of anode and cathode, geometrical relationships between dissimilar metal surfaces, and contact between metals. Of these, relative areas of anodic and cathodic surfaces have the most pronounced effect on the extent of damage produced by galvanic action, because a small anode and a large cathode result in an increase in current density at the anode with a great consequent increase in the rate of corrosion. Thus, small differences in potential under these conditions may produce extensive corrosion because of increased current density in the anodic areas.

2.3.5. Erosion Corrosion

Erosion-corrosion is the highly accelerated corrosion of an alloy exposed to a corrosive solution flowing faster than a critical velocity peculiar to that alloy. Characteristically, corrosion is mild at lower velocities. Critical velocity is determined as 20 m/s to initiation of erosion corrosion in seawater for steel materials (Ichikawa 2000, Ellis 1985)

2.3.6. Intergranular Corrosion

Inter-granular corrosion occurs when the grain boundaries of the metallic microstructure corrode preferentially, causing the grains to fall out. This process can occur in austenitic stainless steels in low- temperature geothermal environments, but only if the stainless steel is defective in heat treatment or is improperly welded (Ellis 1985).

2.3.7. Stress Corrosion Cracking

Stress corrosion cracking (SCC) is the cracking of an alloy as a result of the interaction of stress, applied or residual from forming and fabrication, and a specific environmental factor. Some stainless steels are crackled by chlorides under certain conditions (chloride- SCC) and some copper alloys are so attacked by traces of

ammonia (ammonia-SCC). A special case of SCC can result when high strength low alloy (HSLA) steels are exposed under stress to waters containing hydrogen sulfide. This particular form of SCC is commonly called sulfide stress cracking (SSC).

2.3.8. Dealloying

Dealloying is the selective leaching on one constituent element of an alloy, without change in the gross shape of the component. Three forms have been observed in low-temperature geothermal components: dezincification of yellow brass, graphitization of cast iron (the iron is removed leaving the carbon matrix), and deplumbification (removal of lead) from a lead-tin solder (Ellis 1985).

2.3.9. Biocorrosion

Corrosion reactions can be influenced by microbial activities, especially when the organisms are in close contact with the metal surface forming a bio-film. The resulting metal deterioration is known as biocorrosion, or microbially -influenced corrosion (MIC). MIC is the result of a microbiologically-influenced change that promotes the establishment or maintenance of physicochemical reactions not normally favoured under otherwise similar conditions. The main types of bacteria associated with corrosion failures of cast iron, mild and stainless steel structures are sulfate-reducing bacteria, sulfuroxidising bacteria, iron-oxidising/reducing bacteria, manganeseoxidizing bacteria, and bacteria secreting organic acids and exopolymers or slime (Beech and Gaylarde 1999). Sulfate reducing bacteria (SRB) are nonpathogenic and anaerobic. They are capable of causing severe corrosion of iron material in a water system because they produce enzymes which have the power to accelerate the reduction of sulphate compounds to the corrosive hydrogen sulphide, thus SRB act as a catalyst in the reduction reaction. However, in order for this reduction to occur, four components must be present. That is, SRB must be present, sulphates must be present, an external energy source in the form of free electrons must be present, and the temperature of the water for better SRB activity must be less than approximately 65 ^{0}C (Yuzwa and Eng 2000). There are some main characteristics of the anaerobic corrosion of iron by SRB's: It only occurs in anaerobic environments e.g. the inside of water pipes. Corrosion often occurs

more rapidly in areas which are subject to partial or intermittent anaerobic conditions. The metal is not evenly corroded, but tends to be pitted resulting in local perforation of pipes, and at the point of corrosion the metal is completely removed, often leaving the graphite skeleton of the pipe in its original form. The mechanism whereby this corrosion occurs is cathodic depolarisation (Reeves 1997). In order to reduce the possibility of sulphate reducing bacteria proliferation in a water system, these activities are recommended: Maintain a water temperature greater than 65 ^{0}C for hot water heating systems and domestic hot water systems. Reduce the corrosion of iron material in hot water heating & chilled water systems by eliminating air ingression into the system and by maintaining the prescribed inhibitor concentration in the system. Drain & flush the expansion tank and cooling coils of chilled water systems at the beginning of the cooling season. Circulate the contents of stagnant domestic hot water, chilled water, and hot water heating systems periodically during their shut down periods. Chemically clean the piping of the water system if it contains appreciable amounts of corrosion deposits (Yuzwa and Eng 1991).

2.4. Corrosion Inhibitors

A corrosion inhibitor is a chemical substance which, when added in small concentrations to an environment, minimizes or prevents corrosion (Riggs 1973). The application of inhibitors must be viewed with caution by the user because inhibitors may afford excellent protection for one metal in a specific system but can aggravate corrosion for other metals in the same system. Various types of inhibitors commonly used include anodic, cathodic ohmic, precipitation and vapor phase inhibitors (Van Delinder 1984). Anodic inhibitors function by slsectively covering anodic sites on the metal surface. Cathodic inhibitors reduce corrosion by slowing the reduction reaction rate of the electrochemical corrosion cell. This is done by blocking the cathodic sites by precipitation. Arsenic, bismuth and antimony, which are refferred to as cathodic poisons, reduce the hydrogen reaction rate and, thus, lower the overall corrosion rate. Ohmic inhibitors also referred to as general filmin inhibitors, reduce the corrosion rate by decreasing the mobility of ionic species between anodes and cathodes on the corroding metal surface. By decreasing the ionic activity of the solution, the corrosion rate is reduced. Precipitation inhibitors promote the formation of a bulky precipitation

film over the entire surface. Vapor-phase inhibitors are chemical compounds that have relatively high vapor pressures and that adsorb on metal surfaces. Once adsorbed, they can either neutralize moisture, promote the formation of passive films, or protect through the formation of a general film on the surface (Davis 2003). Inhibitors used in practice are seldom pure substance, but are usually mixtures that may be byproducts, for example, of some industrial chemical processes for which the active constituents is not known. Commercial inhibitor packages may contain, in addition to the active ingredients for inhibition, other chemicals, including surfactants, deemulsifiers and biocides (Papavinasam 1992). Biocides are chemicals that kill or control microorganisms. For example, if SRB are detected in a hot water heating system, a biocide must be added to circulating system (Van Delinder 1984).

2.5. Characterization of Corrosion Products using Scanning Electron Microscopy / Energy Dispersive X-ray Spectroscopy

Scanning electron microscopy (SEM) is used to obtain an electron image of the morphologic and topographic information of a material surface. For an electron microscopic image, the surface of a material is scanned with a finely focused beam of electrons. When the energetic beam of electrons scans the surface, signals including secondary, back scattered electrons are produced from the surface. The secondary electrons signal is usually used to modulate the brightness of the cathode ray display screen, thereby forming the image. The secondary electron emission is determined to a large extent by the surface topography. When the image is formed from the back-scattered electron signal, the contrast is determined largely by compositional differences in the sample surface rather than topographic characteristics. The intensity of the signal is proportional to the number of electrons emitted from each scanned location on the surface. The difference in signal intensity from different locations allows an image of the surface to be formed. Energy dispersive x-ray (EDX) analysis is used to obtain the quantitative information about the elemental composition on the local surface of the material. In addition, the elemental distribution of the surface can be mapped or line scanned (Metal Handbook 1986, Maeng 1999).

2.6. Corrosion Classification in Low Temperature Geothermal Systems

Ellis (1985) proposed a Geothermal Corrosivity Classification System that divided the currently developed geothermal resources into six classes based on the key corrosive species, temperature, and similarities in corrosion behavior. This classification allow some to generalize the materials performance and design requirements. The Class V is the class containing low-temperature geothermal resources and it is further divided into two sub-classes, Class Va and Class Vb. The division was based on the statistical evaluation of carbon steel corrosion data from 29 separate tests of different resources. Class Va systems have some defining parameters that are liquid-dominated resource type, less than 5000 ppm total corrosive key species (TKS = Total chloride + sulfide + carbon dioxide species + sulfide species + ammonia species in produced fluid.), 3 to 72 percent chloride fraction in total corrosive key species, 207 to 1329 ppm $CaCO_3$ total alkalinity, 6,7 to 7,6 pH (unflashed fluid), 48 to 96 ^{0}C resource and plant inlet temperature. In non-aerated fluids, the median uniform (weight-loss) corrosion rate is 12.5 mpy, with a probable range (95 percent confidence limits) of 4.9 mpy - 20.2 mpy and one of nine tests showed no pitting, others showed severe pitting as high as 83 mpy, moreover, aeration may cause a 4- to 15-fold increase in weight-loss corrosion as pitting for carbon steel in Class Va class low temperature geothermal systems. In non-aerated fluid, uniform corrosion of copper in heat transfer service is 1 to 10 mpy with severe crevice corrosion under corrosion product scale. Brasses and cupronickels are less suitable than copper for heat transfer. Type 316 stainless steel is resistant to uniform corrosion, pitting and crevice corrosion, and stress corrosion cracking in many applications for class Va low temperature geothermal systems. Class Vb systems have similar defining parameters with class Va systems. Differences are on the total alkalinity with less than 210 ppm $CaCO_3$ and 7.8 to 9.85 pH for unflashed fluid. For class Vb low temperature geothermal systems, in non-aerated fluid, the median uniform (weight-loss) corrosion rate is 0.12 mpy with an upper limit (95 percent confidence) of 1.65 mpy with 28 percent no detectable pitting. Additional 40 percent pitted at less than 5 mpy. Maximum observed pitting rate was 20 mpy. Aeration may cause a 4- to 15-fold increase in weight-loss corrosion with probably heavy pitting (Ellis 1985, Ellis and Conover 1981)

CHAPTER III

EXPERIMENTAL

3.1. Materials

The materials tested for the corrosion performance in Izmir-Balçova geothermal district heating system include the four widely used steels in the geothermal heating systems, these are St-37 carbon and AISI 304, 316 and 316L austenitic stainless steels. The steels were commercially available and obtained from a local company in the form of sheet. Corresponding chemical compositons of the steels provided by the supplier are tabulated in Table 3.1. AISI 316L steel has the same compositin with AISI 316 except the former contains the lower content of carbon. The carbon content of St-37 is higher than those of stainless steels, 0.17%, but still considered as low carbon steel. The microstructures of as-received steels were analyzed through the optical microscope and a representative micrograph of typical microstructure of St-37 carbon steel is shown in Figure 3.1. The structure consists of 10 µm ferrite grains on the average and small regions of fine perlite distributed between the ferrite structure. Figure 3.2 shows the microstructure of the AISI 304 stainless steel tested, composed of 8 µm austenite grains on the average and twins inside grains. It was found microscopically that 316 and 316L austenitic stainless steels used resembled the similar microstructure with AISI 304 stainless steel.

Table 3.1. Chemical composition of investigated steels.

Name	C	Mn	P	S	Si	Cr	Ni	Mo	Others
St 37	0.17	0.3	0.05	0.05	0.3	-	-	-	-
AISI 304	0.08	2.00	0.05	0.03	1.00	19.00	9.25	-	-
AISI 316	0.08	2.00	0.05	0.03	1.00	17.00	12.00	2.50	-
AISI 316L	0.03	2.00	0.05	0.03	1.00	17.00	12.00	2.50	-
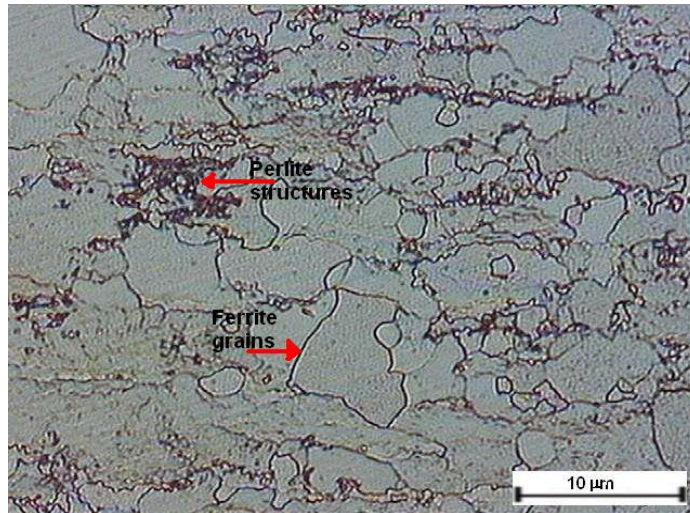
Figure 3.1. The optical micrograph of the microstructure of st37 steel, showing feritte grains and fine perlitic structure.
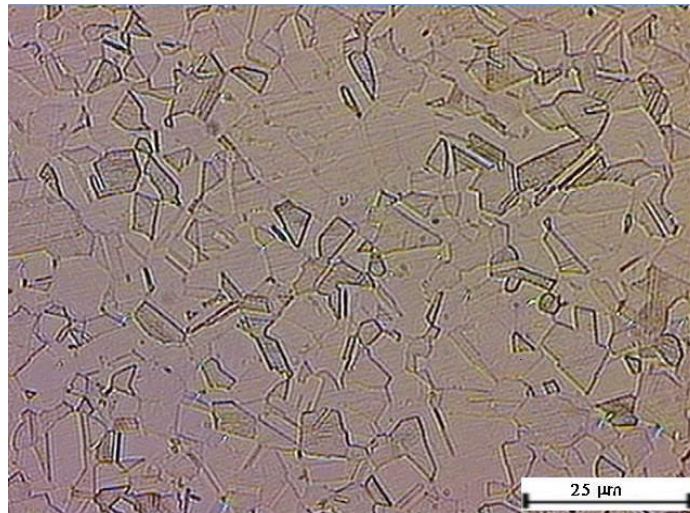
Figure 3.2. The optical micrograph of the microstructure of AISI 304 austenitic stainless steels, showing austenite grains and twins.

3.2. Laboratory Tests

As stated before in Chapter 1 Ryznar stability index calculation is a suitable test to be applied for a rough estimation of the corrosion behavior of materials in geothermal water before a complex test is performed at the site. The following equations and parameters were used in the calculations. In below equations, MC is the molar concentration in ppm, TDS is the total dissolved solid and C is conductivity at µs/cm.

$$RSI = 2\,pH_s - pH$$

$$where:$$

$$pH_s = Calcium\ factor + Alkalinity\ factor + pseudoconst.$$

$$Calcium\ factor = -\log(MC\ of\ calcium)\quad MC = Molar\ Concentration$$

$$Alkalinity\ factor = -\log(ALK) \hspace{4cm} (3.1)$$

$$ALK = (MC\ of\ HCO_3^{-}) + (MC\ of\ CO_3^{-2} \times 2) + 10^{pH-14} - 10^{-pH}$$

$$if\ total\ dissolved\ solid\ factor\ is\ between\ 1000-2000$$

$$pseudoconst. = 0.00007 \times t^2 - 0.0239 \times t + 2.7925 \quad C = conductivity\ (\eta\ s/cm)$$

$$TDS\ factor = (-0.000000006 \times C^3) + (0.00005 \times C^2) + (0.5886 \times C) - 2.726$$

The electropotentials of the steels tested were also measured in the geothermal water taken from the site against a reference electrode. The set-up used in these tests is shown in Figure 3.3. An Ag/AgCl reference electrode was used as the reference against a working electrode machined from the steel tested. A glass vessel containing the geothermal fluid, electrodes and a thermometer was closed tightly at the top in order to prevent any air inlet to the test fluid as seen in Figure 3.3.
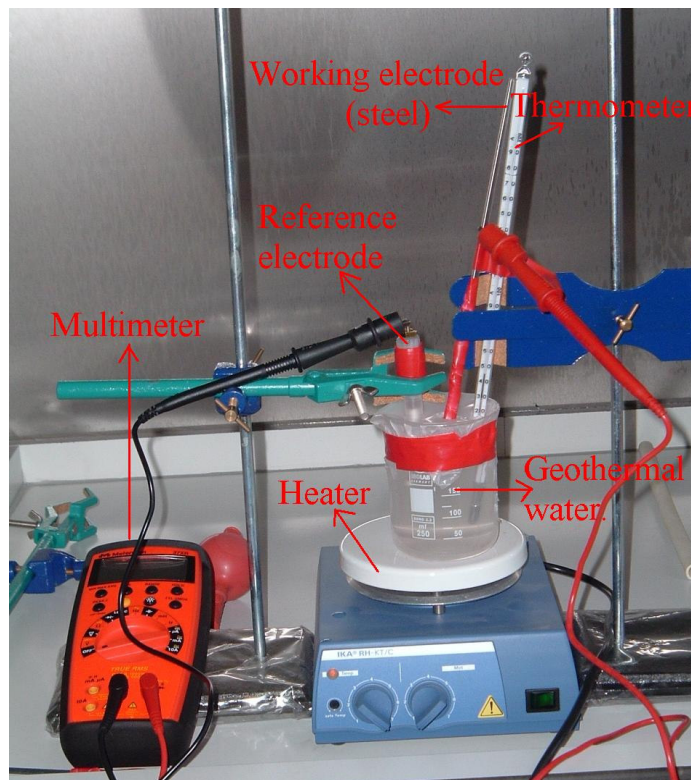
Figure 3.3. Experimental set-up used to measure electropotential of the steels tested in the actual geothermal water.

The glass vessel was heated on a hot plate until the geothermal fluid temperature reached the working temperature of geothermal site, 96 ^{o}C for St-37 and 120 ^{o}C for austenitic stainless steels. Then, the electropotential of the cell was measured using a multimeter. The measured potentials were converted in to saturated hydrogen electrode potentials using the conversion chart given in Figure 3.4.
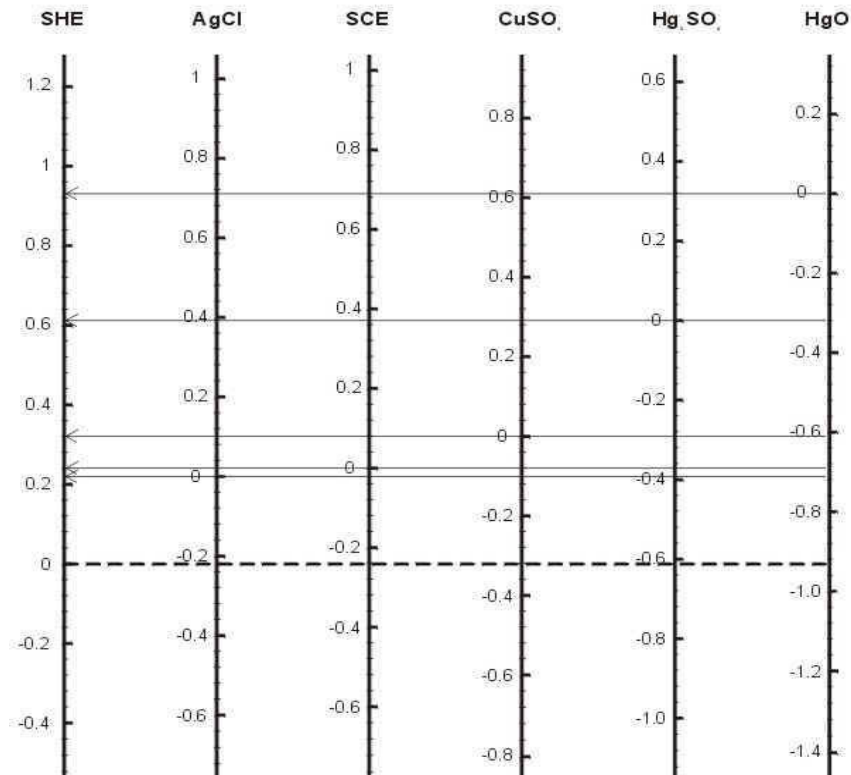
Figure 3.4. The reference electrodes conversion chart (Web_2 2005)

3.3. Specimen Preparation and Experimental Set-up

St 37 steel corrosion test coupons were prepared intentially in the form of tensile test specimens according to ASTM E-8 in order to investigate the effects of corrosion including uniform and pitting type on the mechanical properties. The dimensions of the prepared dog-bone shape tensile test specimens are shown in Figure 3.5. The length of the specimens was 200 mm with a 60 mm gage-length and a thickness of 3 mm. The specimens were machined using a wire-spark erosion machine. Classical rectangle test coupons having dimensions of 40x60x4.5mm and shown in Figure 3.6 were used to test the uniform and pitting corrosion behavior of AISI 304, 316 and 316L austenitic

stainless steel. The surfaces of all tensile and coupon test specimens were grounded with 800 and 1200 grit silicon carbide grinded papers followed by a final polishing with a 6 μm water based diamond solution.
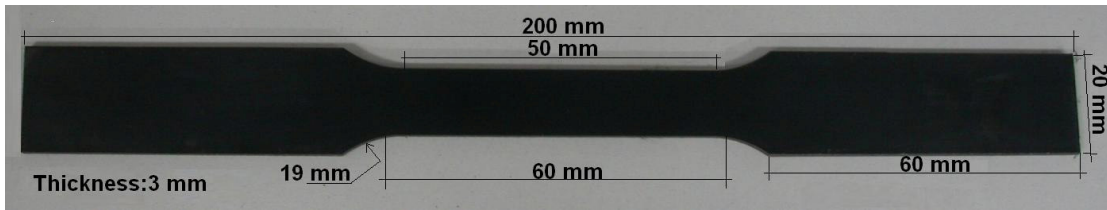
Figure 3.5. St-37 steel tensile test specimen machined according to ASTM E-8 and dimensions.

Figure 3.6. Austenitic stainless steel corrosion test coupons.

The corrosion tests were performed at the site using an experimental set-up designed and constructed particularly for the corrosion tests. The set-up was contructued from st-37 steel and installed in Izmir-Balçova geothermal district heating system. A schematic drawing of the set-up and its dimensions are shown in Figure 3.7. The set-up consists of two sections, A (tank) and B (pipe), as shown the figure. The fluid in these sections flowed with different velocities, allowing the assessment of the effect of fluid velocity on the corrosion rate. The corrosion rates at lower fluid velocities were performed in section A, while higher fluid rates in section B. The fluid velocities were determined using

$$V = \frac{Q}{S} \qquad (3.2)$$

where, Q is the flow rate (m³/sec), V is the fluid velocity (m/sec) and S is the cross-sectional area (m²). The geothermal fluid of B11 well first entered to the set-up from the top of the section A, and then flowed to the reinjection area after passing through the section B (Figure 3.7). The flow were adjusted using a valve inserted to the enterence of the section A. A thermocouple, manometer and digital flow meter were placed to the entrances of the sections A and B in order to measure the temperature, pressure and velocity of the fluid. A valve was also used to drain the water before the corroded specimens were taken from equipment and another was used for outletting the air before the fluid was allowed to flow through the set-up. A lid in section A of Figure 3.7 was to insert/take out the specimens to/from the set-up.

Specimens were hanged up in section A using a heat resistance rope between cylindrical rods as depicted in Figure 3.8. Specimens were placed in way that they did not touch to the rods and any section of the set-up and their flat surfaces remained parallel to the fluid flow. Specimens in section B were placed again using the heat resistance rope, but in this only three specimens were replaced in each run due to the smaller diameter of the pipe. Specimens were hanged up in section between bottom cylindrical rods and filter which is placed on the pipe at exit of tank as depicted in Figure 3.7.
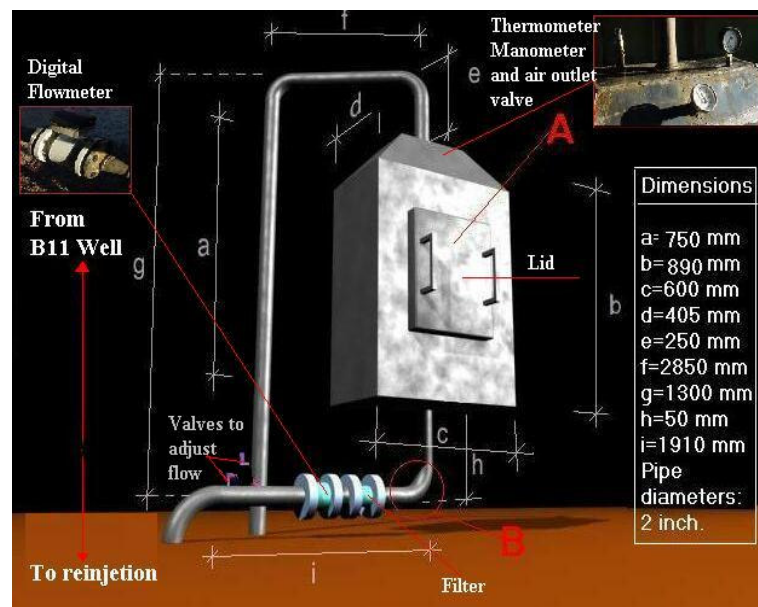
Figure 3.7. Schematic representation of the experimental set-up.
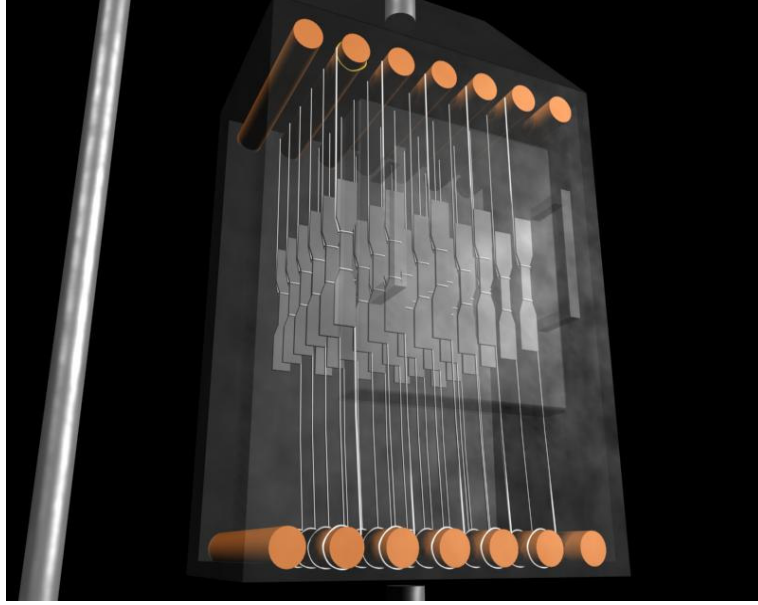
Figure 3.8. Schematic of St-37 specimens replacement in section A using heat resistant ropes.

The temperature, pH, electrical conductivity and chloride content of the few wells in Izmir-Balçova district heating geothermal system are shown in Figures 3.9 (a-d), respectively. B11 well represented an average property of the wells in terms of temperature, electrical conductivity and Cl content and therefore was selected for the corrosion studies. The chemical analysis of the water of B11 well provided by the Izmir-Balçova geothermal system, is given in Table 3.2. The properties of the fluid in the corrosion testing of St-37 and stainless steels including temperature, pressure, flow rate, velocity, Reynold number (Re) and flow pressure are tabulated in Table 3.3. The Reynolds number and pressure at section B were calculated using the following equations.

$$\mathrm{Re} = \frac{V_m \times Dh}{v} \tag{3.3}$$

$$\frac{P_1}{gq} + \frac{V_1^{\,2}}{2g} + z_1 = \frac{P_2}{gq} + \frac{V_2^{\,2}}{2g} + z_2 + h_{total} \tag{3.4}$$

$$h_{total} = f_{pipe} \times \frac{L_{pipe}}{Dh_{pipe}} \times \frac{V_2^{\,2}}{2g} + f_{\tan k} \times \frac{L_{\tan k}}{Dh_{\tan k}} \times \frac{V_1^{\,2}}{2g} + Kl_{contr.} \times \frac{V_1^{\,2}}{2g} + Kl_{elbow} \times \frac{V_2^{\,2}}{2g} \tag{3.5}$$

where, V_m is the mean velocity, Dh is the hydraulic diameter, v is kinematic viscosity, P_1 is the pressure in section A, P_2 is the pressure in the section B, q is the density, V_1 is velocity in section A and V_2 is the velocity in section B, Z is the level, h_{total} is the total head losses due to the friction, contraction and 90° elbow, f is the friction loss factor determined using a moody chart. Relative roughness which equals to roughness of material divided by hydraulic diameter of considered equipment and calculated reynolds number was used to find friction loss factor using moody chart. The roughness of the section A and B was taken as 0.045 mm. Kl constant value was taken 0.2 for 90° bend and 0.5 for the contraction of fluid flow from the tank to the pipe. L is the length. P_1 was measured via a manometer as mentioned before and P_2 was calculated using above equations.

(a)   (b)

(c)   (d)
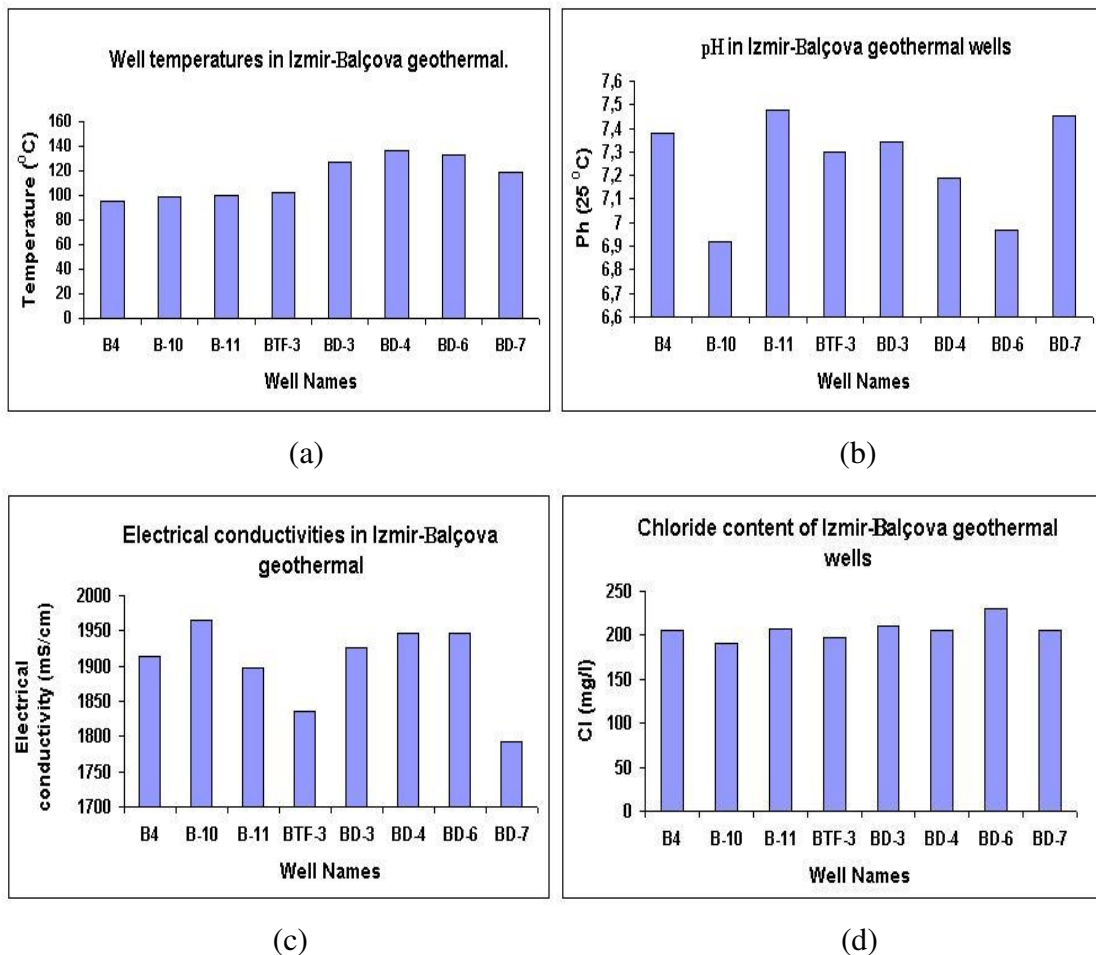
Figure 3.9. (a) temperature, (b) pH, (c) electrical conductivity and (d) chloride content
of the few wells in Izmir-Balçova district heating geothermal system.

Table 3.2. B11 well fluid chemical analysis taken during the exposure of the specimens.

St 37 type carbon steel specimens	Well	T (°C)	pH (25 °C)	EC (25 °C) μS/cm	Li⁺ mg/l	Na⁺ mg/l	K⁺ mg/l	Mg₂⁺ mg/l	Ca₂⁺ mg/l	B mg/l	SiO₂ mg/l	HCO₃⁻ mg/l	SO₄⁻² mg/l	F⁻ mg/l	Cl⁻ mg/l
	B11	96	7,48	1897	1,5	367	30	24	31	9,2	124	623	161	3,8	208
Austenitic stainless steel specimens	Well	T (°C)	pH (25 °C)	EC (25 °C) μS/cm	Li⁺ mg/l	Na⁺ mg/l	K⁺ mg/l	Mg₂⁺ mg/l	Ca₂⁺ mg/l	B mg/l	SiO₂ mg/l	HCO₃⁻ mg/l	SO₄⁻² mg/l	F⁻ mg/l	Cl⁻ mg/l
	B11	120	7,37	1864	1,6	371	31	13	34	8,7	148	634	180	3,9	206

Table 3.3. The properties of the fluid in the corrosion tests

St-37 Carbon steel specimens		
	Section A	Section B
Temperature (^{0}C)	96-98	96-98
Pressure (bar)	2	1.26
Flow (m^3/h)	17.5-18.5	17.5-18.5
Velocity (m/s)	0.020-0.021	9.580-10.127
Reynold Number	32093.023	1641196.013
Flow Type	Turbulent	Turbulent
Austenitic stainless steel specimens		
	Section A	Section B
Temperature (^{0}C)	118-120	118-120
Pressure (bar)	2	1.26
Flow (m^3/h)	17.5-18.5	17.5-18.5
Velocity (m/s)	0.020-0.021	9.580-10.127
Reynold Number	32093.023	1641196.013
Flow Type	Turbulent	Turbulent

3.4. Procedure for the Cleaning of the Specimens Before and After Testing

Grounded and polished specimens were degreased using acetone in an ultrasonic bath to remove the traces of metal remained at the specimen surface after grinding and polishing. The specimens were then dried in a stream of hot air and left in a desiccator for 24 hours before they were used in corrosion test. After a corrosion test the corroded specimens were cleaned to remove the corrosion products via scrubbing with a rubber bristle brush and holding the specimen under a stream of distilled water. Removal was confirmed by the examination with a stereozoom microscope. Repeated cleaning treatment was applied if necessary as a result of surface examination. The mechanical forces used in cleaning were tried to be held as nearly constant as possible for each

specimen. All stages of the cleaning were in accord with ASTM G01-90 standart for preparing, cleaning and evaluating corrosion test specimens.

3.5. Corrosion Rate Calculation and Pitting Depth Measurement

The specimens exposed to the fluid were weighted after cleaning. The corrosion rate was calculated as

$$Corrosion\,Rate\,(mm/\,yr) = \frac{87.6 \times W}{d \times A \times T} \qquad (3.6)$$

where, W is the weight loss in mg, d is the density in g/cm^3, A is the surface area in cm^2 and T is the time of exposure in hours according to ASTM G01-90. The thickness loss of the specimen due to the uniform corrosion was determined using the following relation

$$Thickness\,Loss\,(mm) = \frac{0.0099 \times W}{d \times A} \qquad (3.7)$$

Cleaned and weighed specimens were microscopically analyzed under a stereo zoom microscope (Meiji EMZ-TR). All pits on the test sample surfaces were detected and marked with a water-proofed pen. The depths of detected and marked pits were measured using a roughness test device (Mitutoyo SJ-201). The maximum pith depth corresponding to the Ry_{max} value that is the maximum peak to the lowest valley vertical distance within a single sample, was measured. At least 5 measurements were conducted on the detected and marked pits and the obtained maximum value of Ry_{max} was assumed as the maximum pitting depth. Pits were measured only in the gauge length of the st-37 tests samples in order to assess the effect pitting on the mechanical properties.

3.6. Corrosion Product Analysis

The morphologic information on the corrosion products of the specimens exposed to geothermal fluid was obtained with a Scanning Electron Microscopy (SEM-Philips XL 305 FEG). The quantitative elemental compositions of the corroded surfaces

and corrosion product layer were further investigated using an Energy Disperse X-Ray (EDX) spectroscopy. The corrosion product layer of few specimens was investigated through SEM-Line Scan Mode in order to determine the variations of an element through the thickness of the layer. Samples for SEM and optical microscope were prepared metarialographically. Samples were cut using a diamond saw through the thickness direction and then epoxy mounted. Mounted samples were grinded using 800 and 1200 grid silicon carbide papers and the polished sequentially with 9, 6 and 1 μm water based diamond solution. The compounds of the corrosion layers were determined using an X-Ray Diffraction (XRD-Philips X'pert Pro) device.

3.7. Estimation of Service Life

St-37 carbon steel corrosion tensile test specimens which were exposed to the corrosive geothermal water at a prescribed time were tensile tested using a Schimadzu type Universal test machine at a cross-head speed of 2 mm/min. The load-displacement curves were then converted into stress-strain curves. The service life of the St-37 pipes used in the district heating system was estimated based on the Norway standarts "Rules for Subsea Pipeline Systems" called DNV 1996 (FRP I&II 2000). The DNV rules for Subsea Pipeline Systems were first issued in 1976 and updated in 1981 and the most recently in 1996. At all calculations, only internal pressures were considered, others like lateral bending, thermal loading and residual stresses were neglected. The objective of the DNV is to provide an internationally acceptable standard of safety with respect to strength and performance by defining minimum requirements for the design, material selection, fabrication, installation, commissioning, operation, maintenance, re-qualification and abandonment of submarine pipeline systems. DNV RP-F101 is the first codified and comprehensive recommendation practice on the pipeline corrosion defect assessment. The RP-F101 provides an allowable stress design method and gives following equations for the bursting pressure (P_f) as

$$Pf = 2t \times \frac{UTS}{(D-t)} \times \frac{(1-\frac{d}{t})}{(1-\frac{d}{t \times Q})} \qquad Q = \sqrt{1 + 0.31 \times (\frac{1}{\sqrt{D \times t}})^2} \qquad (3.8)$$

where, D and t are the pipe outside diameter and wall thickness, respectively, UTS is the ultimate tensile strength, Q is the geometric factor, d is the pit depth. If the pit lenght is deep enough to raise the stress locally, the following equation is proposed (Brown et al. 1995).

$$Pf = 2.3t \times \frac{UTS}{D} \times \frac{(1 - \frac{d}{t})}{(1 - \frac{d}{t \times Q})} \qquad Q = \sqrt{1 + 0.6275 \times \frac{L^2}{D \times t} - 0.003375 \times \frac{L^4}{D^2 \times t^2}} \qquad (3.9)$$

CHAPTER 4

RESULTS AND DISCUSSION

4.1. Prediction of the Corrosion Behaviour of the Steels from Laboratory Tests

The Ryznar Stability Index of the geothermal water composition is calculated using Eqn.3.1. This value of the index corresponds to light calcium carbonate scaling and relatively low uniform corrosion rate for St-37 steel. Calculations however showed that the Ryznar Stability Index of the geothermal water composition and conditions for stainless steels corrosion experiments was lower, 4.60, corresponding to a heavy calcium carbonate scaling with again relatively low uniform corrosion rates. Another prediction is made on the expected corrosion types of the steels investigated using the E-pH diagram (Figure 4.1.).
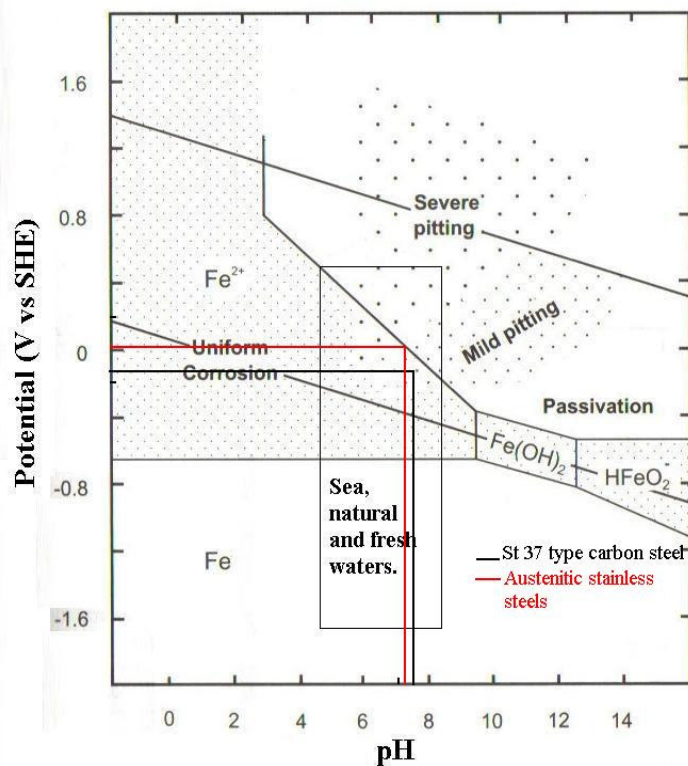
Figure 4.1. Prediction of investigated steel corrosion types in thermodynamic boundaries of the types of corrosion observed on steel and E-pH ranges for water environments graph.

For this purpose the electropotentials of the steels tested in geothermal fluid were measured against Ag/AgCl reference electrode. The measured potentials for St-37, AISI 304, 316 and 316L were sequentially –0.4066, –0,2016, –0.1617 and –0.1529 V, corresponding to -0.1866, 0.0201, 0.0161 and 0.01529 V when converted in to saturated hydrogen electrode potentials The measured electropotential values dictate that AISI 316L stainless steel is the least, while St-37 steel the most active of the steels investigated in the geothermal fluid. Inserting electropotential values of the steels and pH values of the fluids into the E-pH diagram further shows an expected pitting corrosion in the tested steels as seen Figure 4.1. These results should be, however, considered carefully in that they merely show qualitative indications of the corrosion behavior. The pitting resistance equivalents of AISI 316L, 316 and 304 stainless steels were calculated using Eqn.2.7 and found sequentially 25.25, 25.25 and 19, showing a lower pitting resistance of AISI 304 steel as compared with 316 counterparts.

4.2. The Corrosion Behaviour of St-37 Steel at Low Fluid Velocity

4.2.1 Corrosion Rate and Products

The measured weight loss and corrosion rate *vs.* exposure time graphs of St-37 steel in geothermal fluid of 0.02 m/s are shown in Figure 4.2(a) and (b), respectively. The maximum exposure time in this graph is about 1600 h, corresponding to 60-days exposure to the fluid. The initial high uniform corrosion rate at low exposure times seen in Figure 4.2(b) decreases as the exposure time increases and the uniform corrosion rate reaches a constant value, 0.0178 mm/yr after about 600 h. The corrosion rate directly relates to the morphological structure and chemical compounds of the corrosion products, if the environmental parameters are kept the same during an experiment. Therefore, the morphological analyses of the corrosion products were further investigated. Figure 4.3 (a), (b), (c) and (d) show the SEM micrographs of the surfaces of the samples exposed 0, 336, 845 and 1207 h to the geothermal fluid, respectively. A amorphous, porous scaling can be easily seen in Figure 4.3 (b) on the surfaces of the sample exposed 336 h, as compared with untested specimen surfaces given in Figure 4.3 (a). The corrosion rate at 336 h exposure is still high, 0.031 mm/yr. At increasing exposure times, 845 and 1207 h, denser corrosion layers are seen in Figure 4.3 (c) and

(d) on the specimen surfaces. This proves that the initial amorphous, porous corrosion product layer is replaced with a denser one as the corrosion products form and fill the porosities of the initial layer. Once the dense layer is formed, the uniform corrosion rate reaches almost a constant value. The critical exposure time for the dense corrosion layer corresponds to 600 h for the studied St-37 steel and geothermal fluid as depicted in Figure 4.2(b).
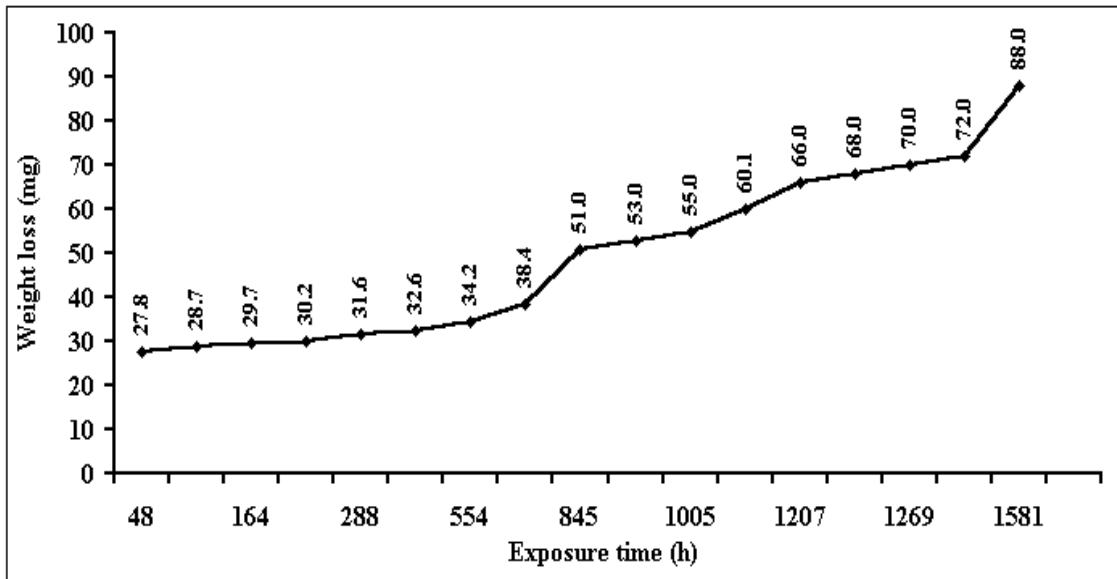
(a)
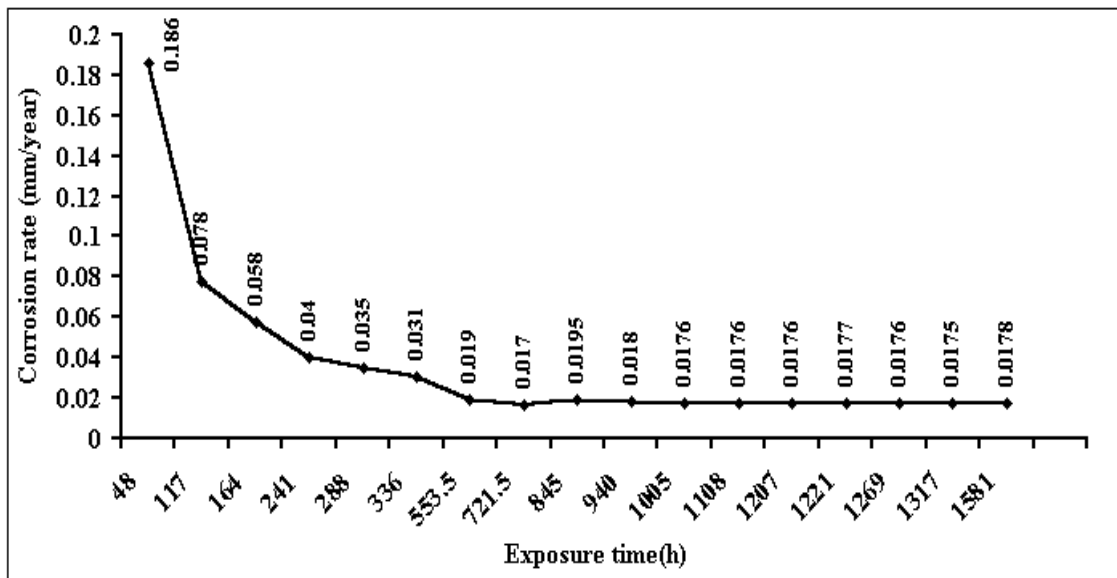
(b)

Figure 4.2. Weight loss and corrosion rate *vs.* exposure time for st-37 at a fluid velocity of 0.02 m/s.

(a)

(b)

(c)

(d)
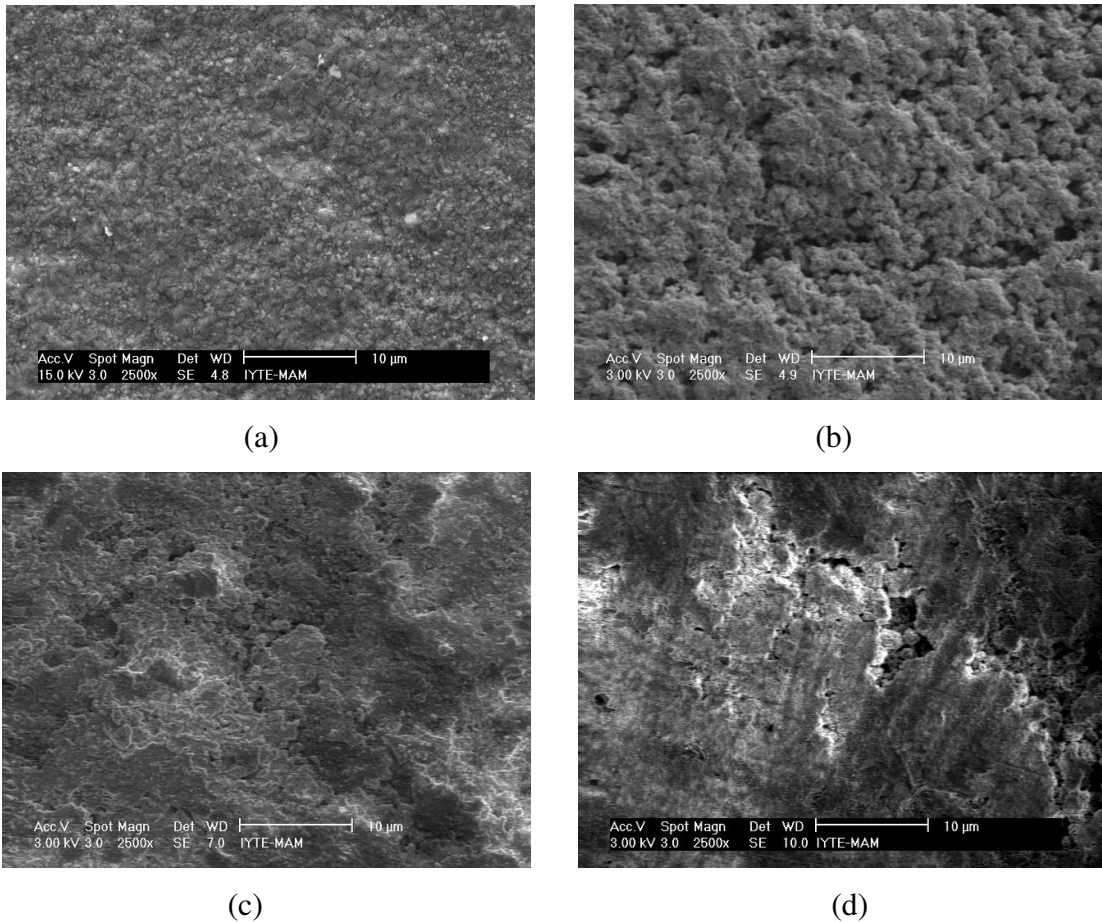
Figure 4.3. SEM surface images of the specimen surfaces after exposure times of (a) 0, (b) 336, (c) 845 and (c) 1207 h.

The EDX analyses results of the corrosion products of the specimens of 336, 845 and 1207 h exposure are shown in Figure 4.4 (a), (b) and (c), respectively. In all tested specimens, the EDX analyses proved the presence of the following elements: C, O, Mg, Si, S, Sb and Fe. The compositions of the corrosion products at these three different exposure times are also tabulated in Table 4.1. It is noted in the same table trace amounts of Si are found in all samples within the studied range of exposure time. Despite relatively small differences, the chemical compositions of the corrosion products of the samples after 845 and 1207 h exposure are very much similar to each other. It is also noted in the same table, although C, O and Fe concentrations increase with increasing exposure time from 336 to 845 and 1207 h, Sb concentration decreases at higher exposure times. Since an Sb-based (Ferrofos 8441 AF) inhibitor was added into the geothermal fluid in the recommended amounts as cathodic inhibitor, Sb was detected in the surfaces of all tested specimens. The function of inhibitor is to slow down the electrochemical cell reactions by adhering to the cathodic sites. The SEM

micrograph shown in Figure 4.5 shows two sites, marked as A and B on the surface of a sample exposed 336 h to the fluid. The section A shown in this figure is a corroded site while the section B is an uncorroded site. The corresponding EDX analysis of the marked sections of A and B are shown in Figure 4.6 (a) and (b), respectively. The relatively high concentration of Sb found in uncorroded section B basically shows the protective feature of the inhibitor. It is also noted in Figure 4.6 (b) that relatively high concentration of S is found in the corroded section A as compared with section B. The presence of a high S content in the corroded sites is related to the microbiological corrosion, which will be discussed later in this chapter.

(a)

(b)

(c)
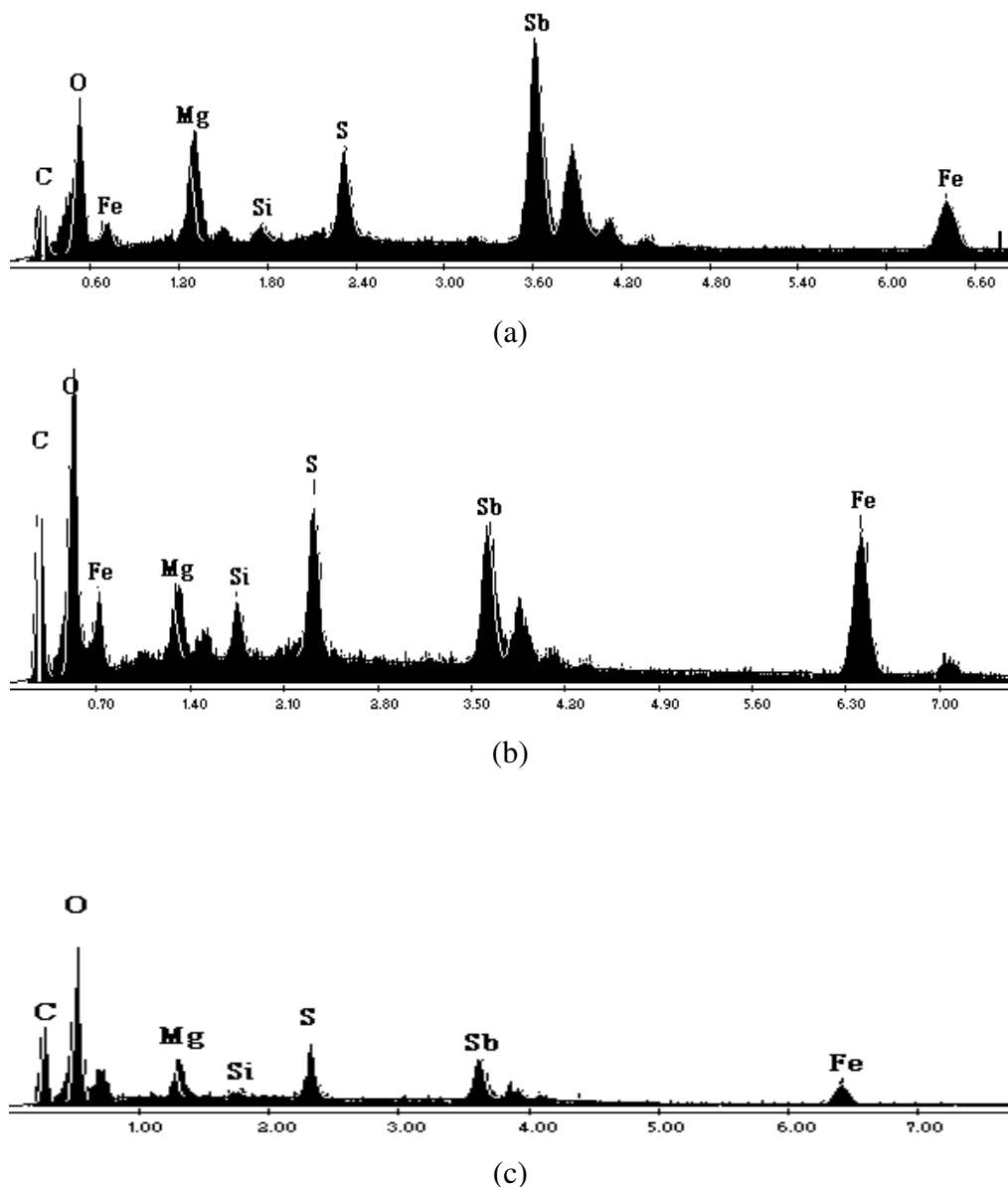
Figure 4.4. The EDX analyses of the corrosion products after exposure times of (a) 336, (b) 845 and (c) 1207 h.

Table 4.1. EDX analyses results of the tested St-37 specimens at three different exposure times.

336 Hours		845 Hours		1207 Hours	
Element	Wt%	Element	Wt%	Element	Wt%
C	11.71	C	23.41	C	22.24
O	10.16	O	16.12	O	17.30
Mg	5.34	Mg	2.06	Mg	3.00
Si	0.94	Si	1.71	Si	0.86
S	4.80	S	5.20	S	6.67
Sb	50.4	Sb	21.54	Sb	26.60
Fe	16.65	Fe	29.95	Fe	23.34
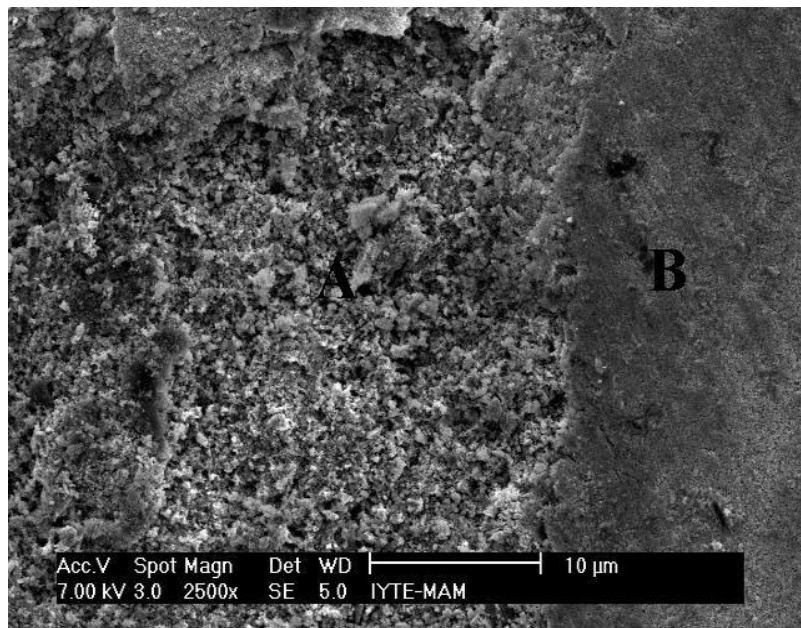
Figure 4.5. An SEM image showing corroded (A) and uncorroded (B) sites on an St-37 sample surface after 336 h exposure.

Element	Wt%	At%
C	14,46	36,32
O	8,76	16,51
Mg	4,86	6,03
Si	1,43	1,53
S	15,52	14,6
Sb	16,05	3,98
Fe	38,92	21,02
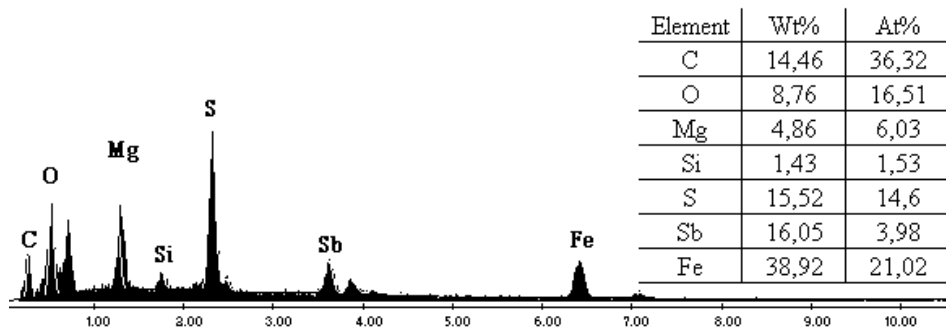
(a)

Figure 4.6. The EDX analyses results of the specimen surfaces shown in Figure 4.5, (a)site A and (b) site B.   (Cont.on next page)

Element	Wt%	At%
C	12,36	42,61
O	10,06	26,02
Mg	1,58	2,7
Si	0,46	0,68
S	0,96	1,24
Sb	71,06	24,16
Fe	3,51	2,6
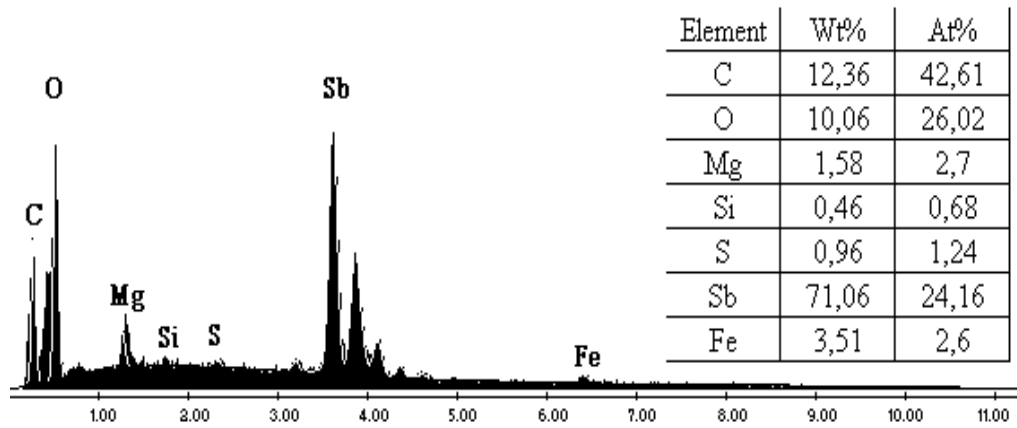
(b)

Figure 4.6. (Cont.)

In Figure 4.7, the epoxy mounted and polished cross-section of the corrosion layer formed on a sample of St-37 after 336 h exposure time is shown. The sample was prepared by cutting the tension sample normal to the gage length and mounting the cross-section in an epoxy mount. As seen in Figure 4.7, the corrosion layer was pulled apart in two parts, one part remained attached to the steel specimen and the other remained attached to the epoxy mount. The split of the corrosion layer is believed to occur most probably during the curing of the epoxy, pulling apart a section of the corrosion layer that was loosely attached to the surface of the sample. It may also be possible that the splitting formed during the grinding and/or polishing stages of the materiallographic specimen preparation. The part of the corrosion layer remained attached to the sample is marked as A and the part on the epoxy site as B. The corresponding EDX analyses of the section A and B in Figure 4.7 are shown in Figures 4.8 (a) and (b), respectively. It is noted from Figures 4.8 (a) and (b) and also from Figure 4.4 (a) Sb is detected only on the surface of the corrosion layer after exposure time of 336 h, while S is found both at the surface and along the cross-section of the corrosion layer. The variations of Sb, S and Fe concentration through the corrosion product layer as function of distance starting from the surface of the corrosion layer (as shown by an arrow in Figure 4.7) are shown in Figure 4.9. The concentration of Sb as shown in this figure decreases slightly from the surface, while the S concentration reaches a maximum and similar to Sb it decreases to an insignificant value in section A. These results conformed with the EDX results shown in Figures 4.8 (a) and (b).
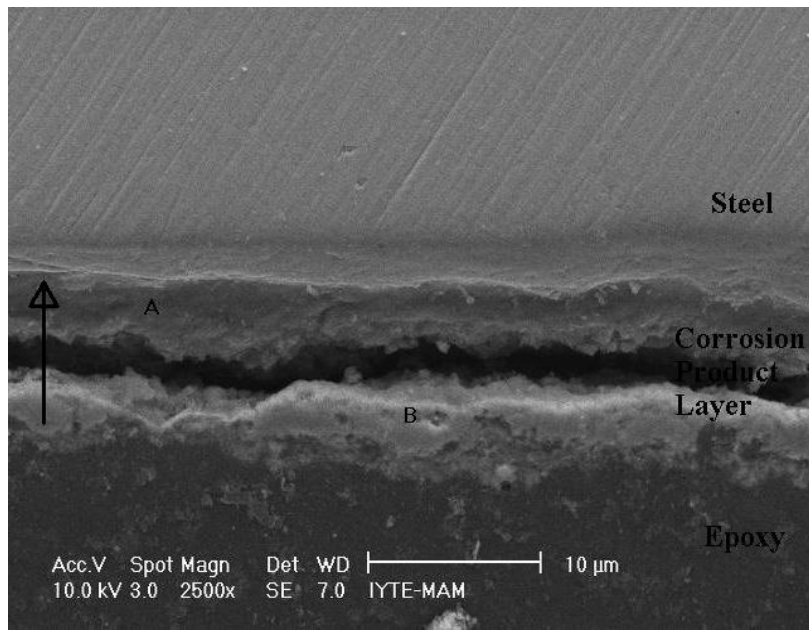
Figure 4.7. The epoxy-mounted and polished cross-section SEM image of an St-37 sample (336 h), showing the split corrosion layers marked as A and B.

Element	Wt%	At%
C	9,74	32,58
O	1,39	3,49
Fe	88,87	63,93

(a)

Element	Wt%	At%
C	14,54	35,23
O	5,95	10,82
Mg	5,52	6,61
Si	0,81	0,84
S	21,7	19,69
Sb	0	0
Fe	51,48	26,82
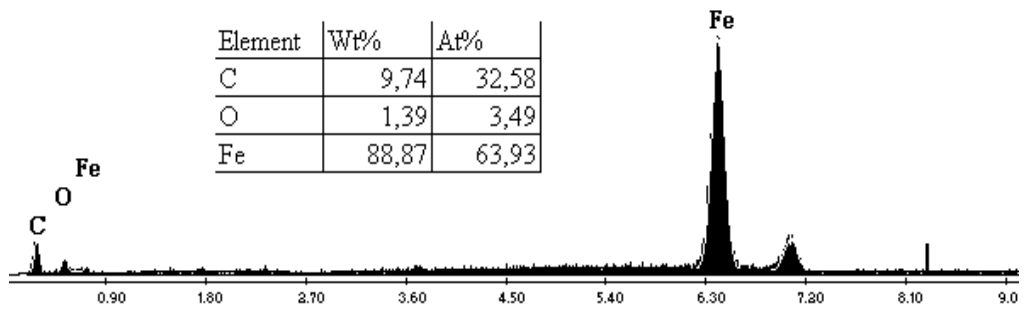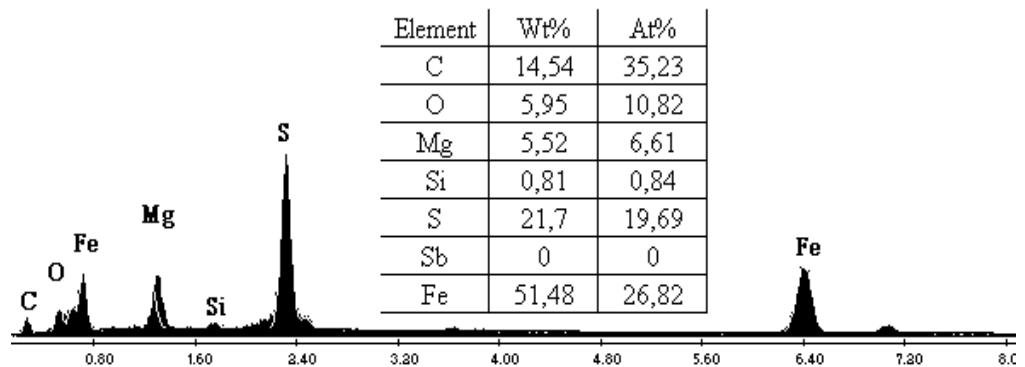
(b)

Figure 4.8. The EDX analyses results of the cross-section shown in Figure 4.7, (a) section A and (b) section B.
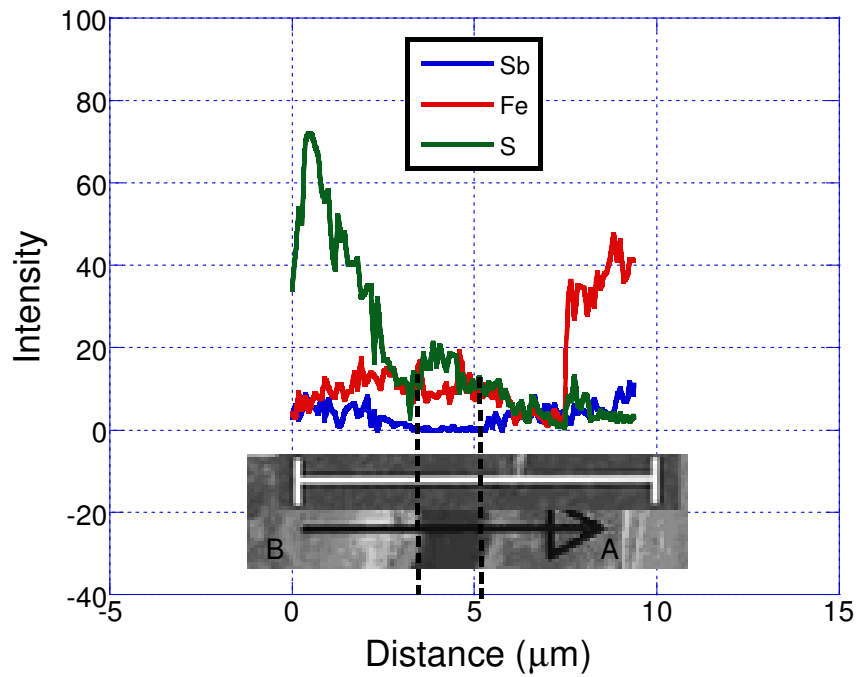
Figure 4.9. The EDX line scans of Sb, S and Fe through the corrosion layer (336 h exposure).

The SEM cross-section image of the corrosion layer formed on a sample after 845 hours is shown in Figure 4.10.
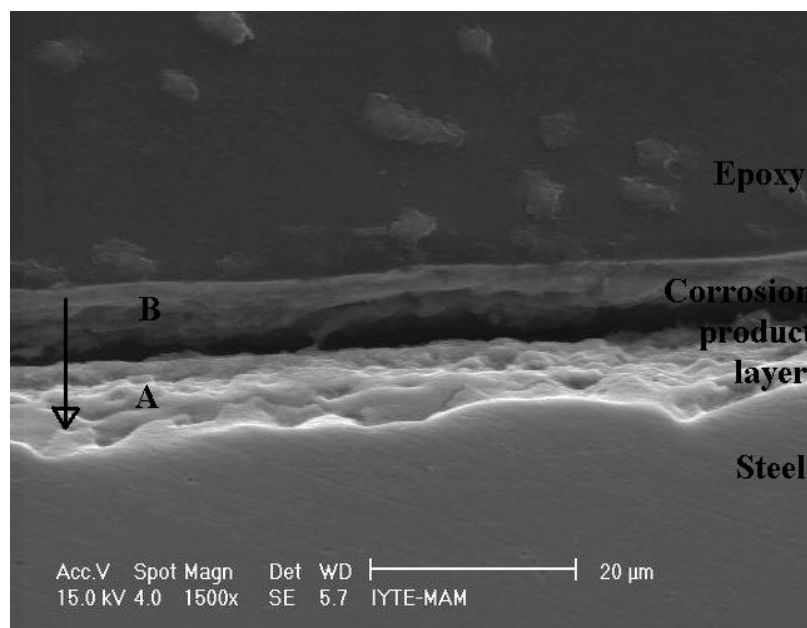
Figure 4.10. The epoxy-mounted and polished cross-section SEM image of an St-37 sample (845 h), showing split corrosion layers marked as A and B.   .

Corresponding EDX analyses results of the split the corrosion layer marked as A and B in this figure are shown in Figures 4.11(a) and (b) respectively. Similar to 336 h exposure, the EDX analyses results shown in Figures 4.11(a) and (b) show the presence of S, Mg, C, O, Sb, Fe and trace amount of Si in the corrosion product layer. The line scans analyses of Sb and S given in Figure 4.12 further show the presence of Sb and S through corrosion layer. The precipitation of Sb is however more pronounced near the surface. Increase on 845 hours exposed specimen antimony precipitation layer thickness comparing with 336 hours exposed specimen was proofed by both EDX analyses and SEM-LS analyses. Change of precipitated sulphur amounts throughout corrosion product layer which was shown in figure 4.12, was also remarkable for 845 hours exposure. As determined at 336 hours exposure time, sulphur precipitation was also found mostly under antimony layer.

Element	Wt%	At%
C	28,57	52,61
O	10,65	14,73
Mg	8,66	7,87
Si	0,57	0,45
S	13,76	9,37
Sb	0	0
Fe	37,79	14,97

(a)

Element	Wt%	At%
C	28,29	51,83
O	16,81	23,13
Mg	0,95	0,86
Si	0,79	0,62
S	3,56	2,42
Sb	10,24	5,63
Fe	39,36	15,51

(b)
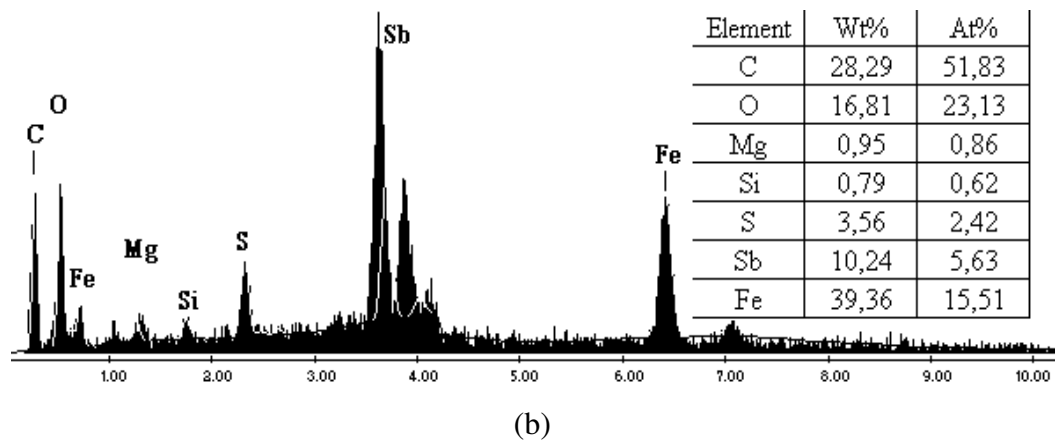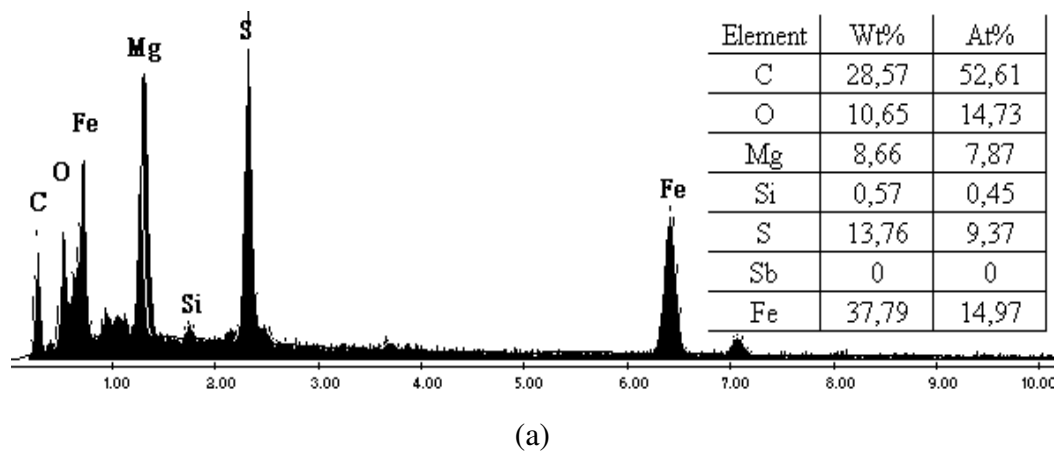
Figure 4.11 EDX analysis results of the cross-sections shown in Figure 4.10, (a) section A and (b) section B.
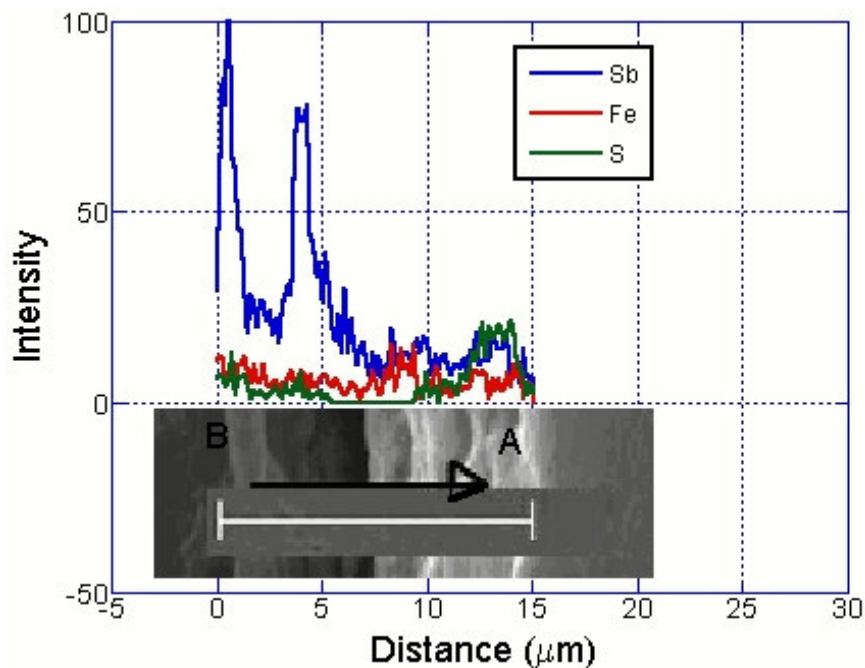
Figure 4.12. EDX line scans of Sb, Fe and S through the corrosion layer (after 845 h exposure).

The microscopic analyses of the corroded specimen surfaces before and after cleaning have shown the evidences of the Sulphate Reducing Bacteria (SRB) particularly in the pits. As is known the SRB reduce sulphate to sulphide, leading a localized corrosion region mostly filled with a black sulphide corrosion product. Although SRB activity requires a complete absence of oxygen (anaerobic) and a highly reduced environment to function efficiently, they also circulate (probably in a resting state) in aerated waters, including those treated with chlorine and other oxidizers until they find an ideal environment supporting their metabolism and multiplication. Studies on geothermal waters have previously shown SRB activity even at temperatures higher than 100 $^{\circ}$C (Torres et al. 2001). A localized corrosion region formed on the surface of a sample after 336 h exposure is shown in Figure 4.13. An anodic region (inside the pit) and a cathodic region (outside of the pit) are clearly seen in the same figure. The SRB inside the pit shown in Figure 4.13 are seen clearly at a higher magnification in Figure 4.14(a) and Figure 4.14(b) further shows an SEM image of SRB in a pit found on the surface of a sample after 1207 h exposure. The sizes of the SRB observed varied in thicknesses and lengths between approximately 0.3 and 0.5 μm and 1 and 3 μm, respectively.
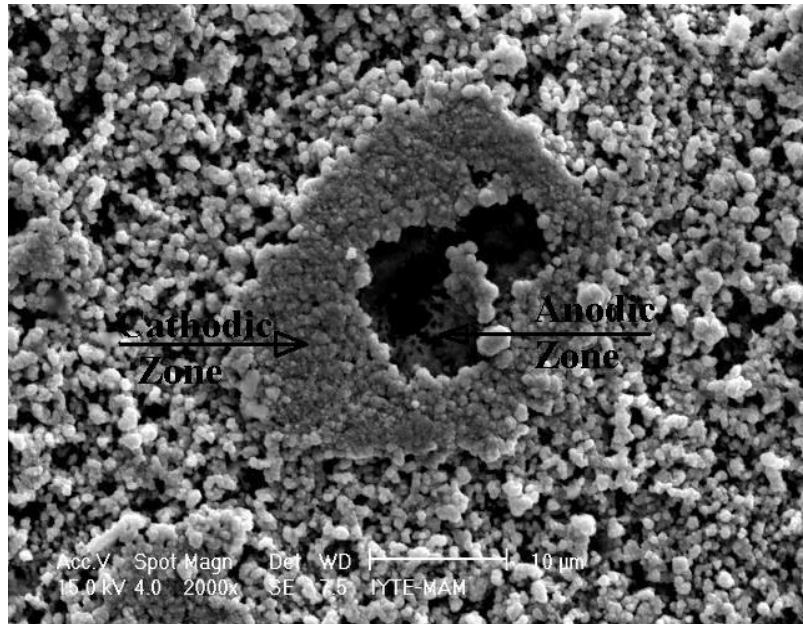
Figure 4.13. SEM image of a pit, showing the anodic and cathodic zones and the accumulation of the SRB in the anodic zone.
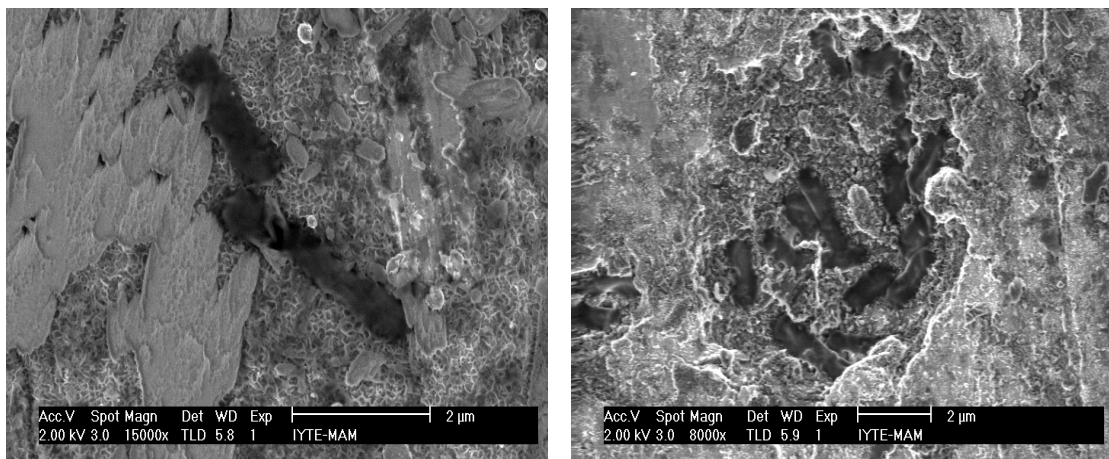
Figure 4.14. SEM images of the SRB inside the pits after (a) 336 h and (b) 1207 h exposure.

Tubercle structures were detected on the corroded surfaces of the tested samples. An example of the tubercle structure containing a porous columnar fiber region (inner crust) on it is shown in Figure 4.15(a). The tubercle shown in this figure is approximately 30 μm in diameter. The EDX analyses results of the outer crust of the tubercle structure shown in Figure 4.15(a) are given in Figure 4.15(b). The EDX analyses of the outer crust of the tubercle structure show the presence of ferric hydroxide and/or hydrated ferric oxide.
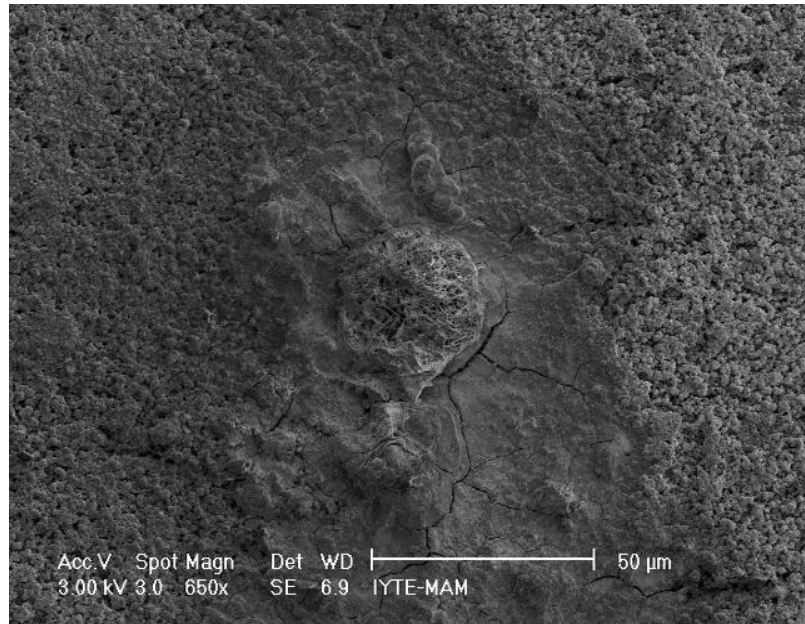
(a)
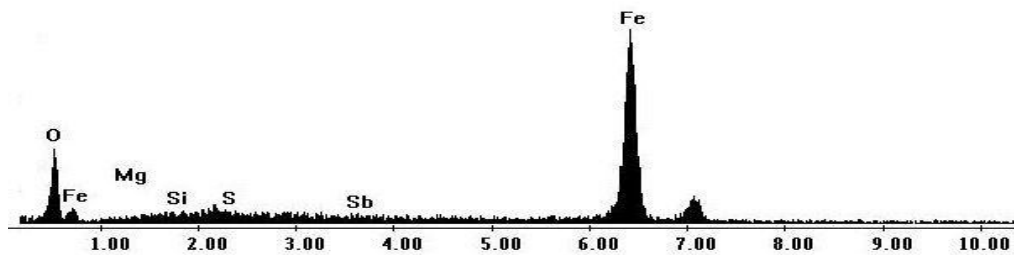
(b)

Figure 4.15. (a) SEM image of a tubercle structure of porous columnar fibers formed on the corroded St-37 steel surface and (b) EDX analysis of the outer crust.

Stereo zoom microscope images of a macro level tubercle structure, 0.8 mm in diameter, before cleaning the surface of the sample is further shown in Figure 4.16 (a). The outer crust of the tubercle consisting of a reddish brown ferric hydroxide or hydrated ferric oxide is easily detectible. The interior of a tubercle usually contains a solution of ferrous chloride and sulfate ions in concentrations higher than those in the water. The solution is slightly acid and may have a pH of approximately 6. This liquid is covered by a black inner crust consisting of hydrous Fe_3O_4, which, being magnetic, is attracted to the iron to form porous columnar fibers. The flow of the current protects the

metal in the immediate vicinity of the pit. After cleaning of the surface, the presence of a pit under the tubercle is shown in Figure 4.16(b). Optical microscope micrograph of a macro size tubercle structure, 0.1 mm in diameter, is shown in Figure 4.17(a). The pitting initiation under the tubercle structure is again clearly seen in Figure 4.17(b) after cleaning of the corroded surface of the specimen. Tubercle structures were detected almost in the surfaces of every specimen investigated at fluid velocity of 0.02 m/s.

(a)   (b)
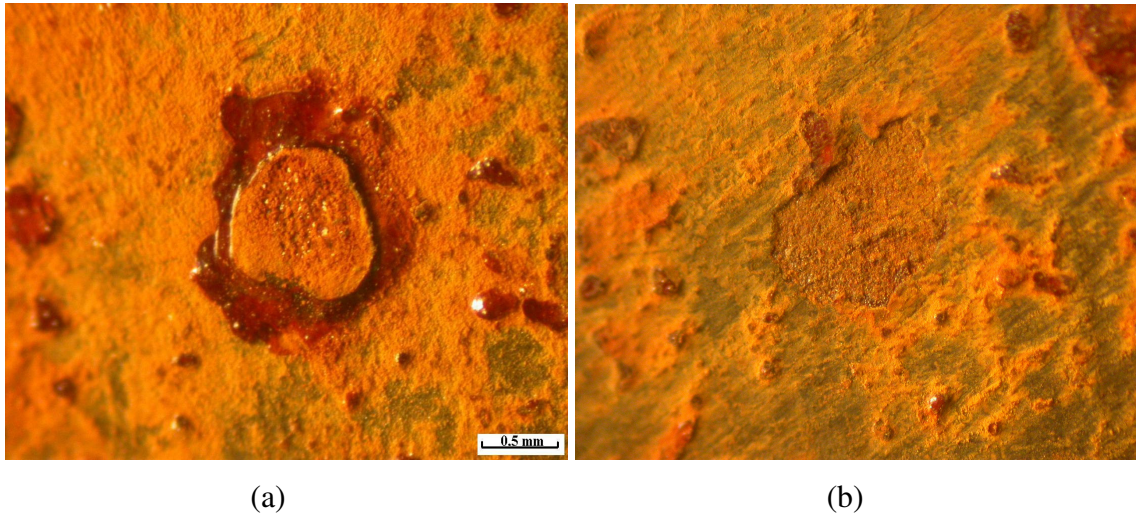
Figure 4.16. Stereo zoom microscope images of (a) a tubercle structure and (b) pitting corrosion initiated under the tubercle structure.

(a)   (b)
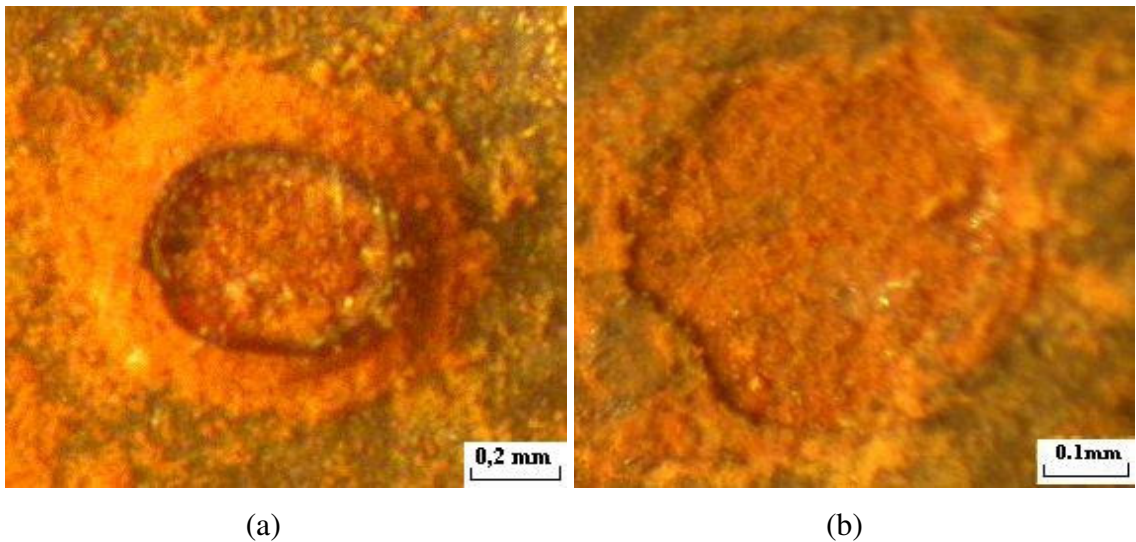
Figure 4.17. Stereo zoom microscope images of (a) a tubercle structure and (b) pitting corrosion initiated under tubercle structure.

The XRD analysis on the corrosion products recovered after cleaning of the surfaces of the specimens confirmed that the corrosion products were the same after 336, 845 and 1207 h exposure and composed of elemental iron, mackinawite (FeS), valentinite (Sb_2O_3) and carbon sulfide (CS_2) as shown in Figure 4.18. The SRB assist the corrosion of steel apparently by consuming hydrogen produced in the cathodic reaction and therefore increase the rate of the cathodic reaction. The bacteria make use of the H^+ to reduce sulphate to iron sulphide through the following reactions;

$$8e^- + 8H^+ \rightarrow 8H$$
$$SO_4{}^{-2} + 8H \rightarrow S^{-2} + 4H_2O \qquad (4.1)$$
$$Fe^{+2} + S^{-2} \rightarrow FeS$$
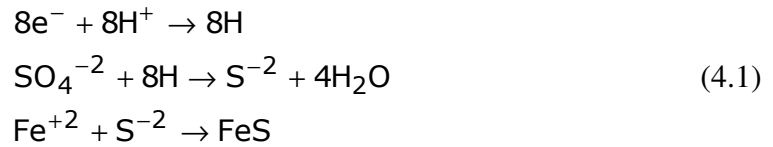
Therefore, the formations of FeS and also CS_2 are attributed to the SRB, while the formation of valentinite is derived from the inhibitor.
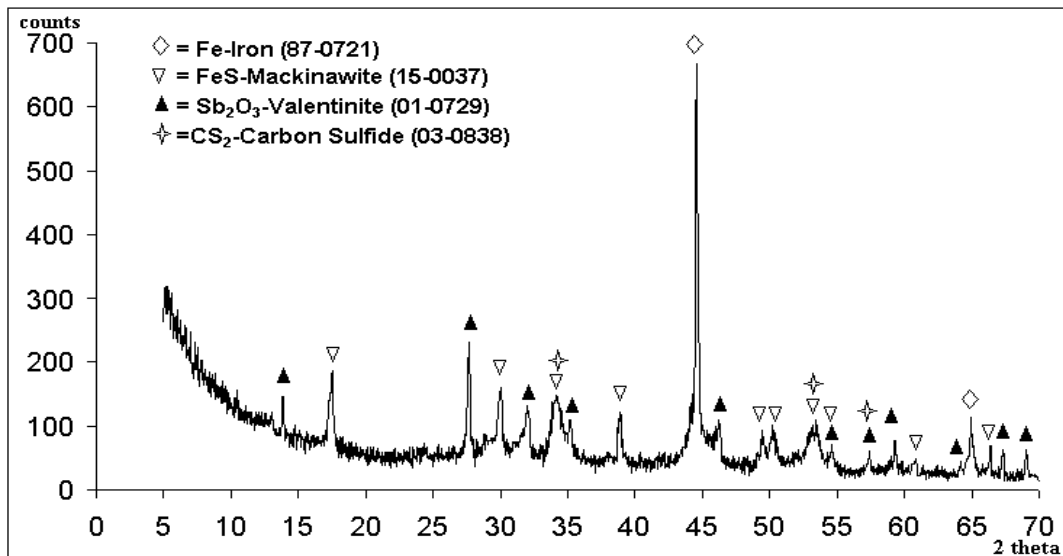
Figure 4.18. Typical XRD analysis of the corrosion products form on the surface of St-37 samples after 336, 845 and 1207 h exposure.

4.2.2. Pit Depth, Mechanical Properties and Service Life at Low Velocity Fluid Flow

The optical microscope images of the pits at increasing exposure times are shown in Figure 4.19. The corresponding exposure time for each image is indicated on

the left-bottom of the image. The pit having the maximum measured depth is further marked with a red-circle in each image. As seen in this figure, at increasing exposure times the pit length increases. The maximum pith length is measured 0.8mm and found in the sample exposed 1005 h. The maximum, minimum average pitting length rates were calculated and found 19.917, 3.32 and 8.72 μm/day, respectively. It has been also found that the pit lengths were higher than it's depths; therefore, the pit shapes of the corroded St-37 steel surface can be classified as shallow wide, vertical grain and elliptical type. Since the pit formation and growth processes are stastical in nature, the maximum pit depths of 8 tests specimens exposed 1581 h to the fluid were measured. The results are shown in Figure 4.20. The maximum pit depth varies between 33-38 μm for a constant exposure time as shown in this figure. Therefore the measured maximum pit depths for different specimens show maximum plus and minus 5 μm deviance.
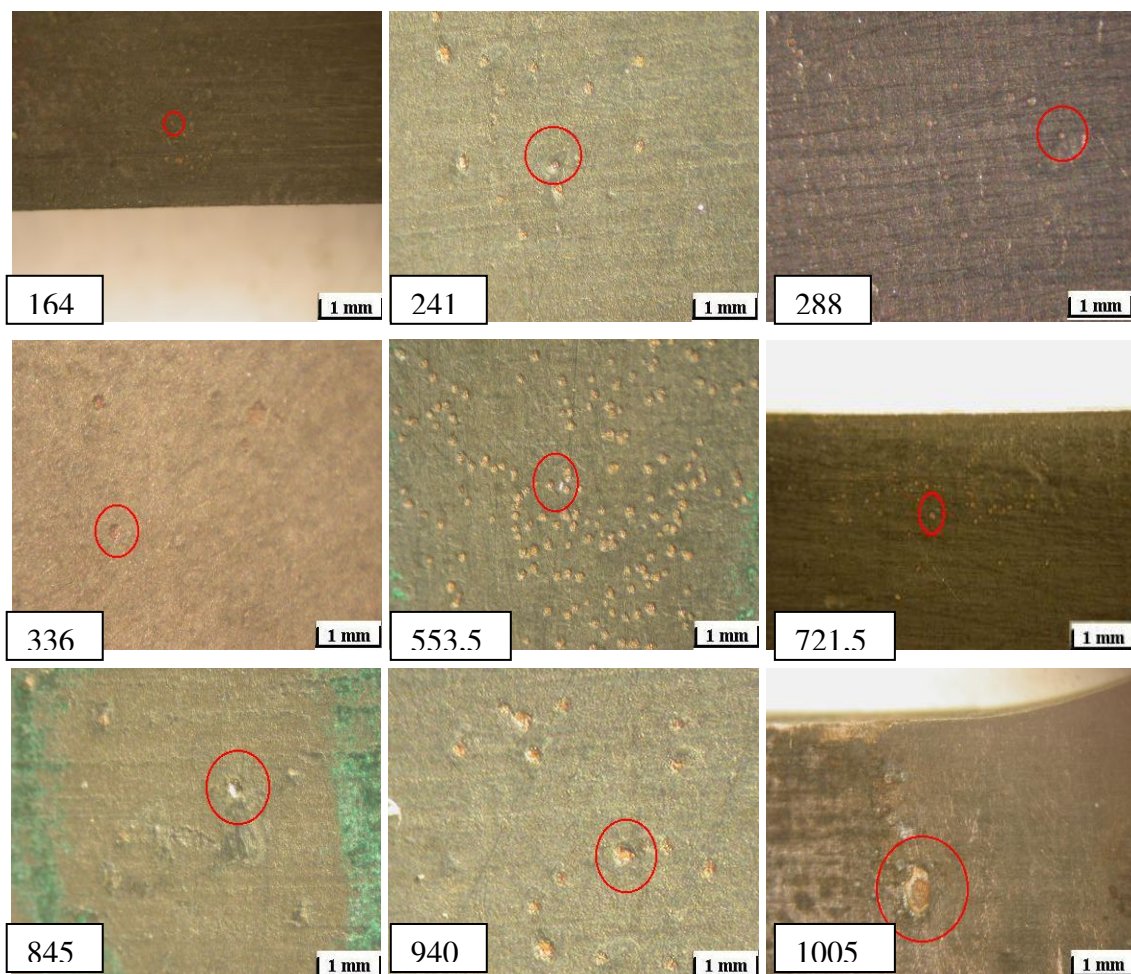
Figure 4.19. Stereo zoom microscope images of the pits formed on surfaces of St-37 steel at increasing exposure times.
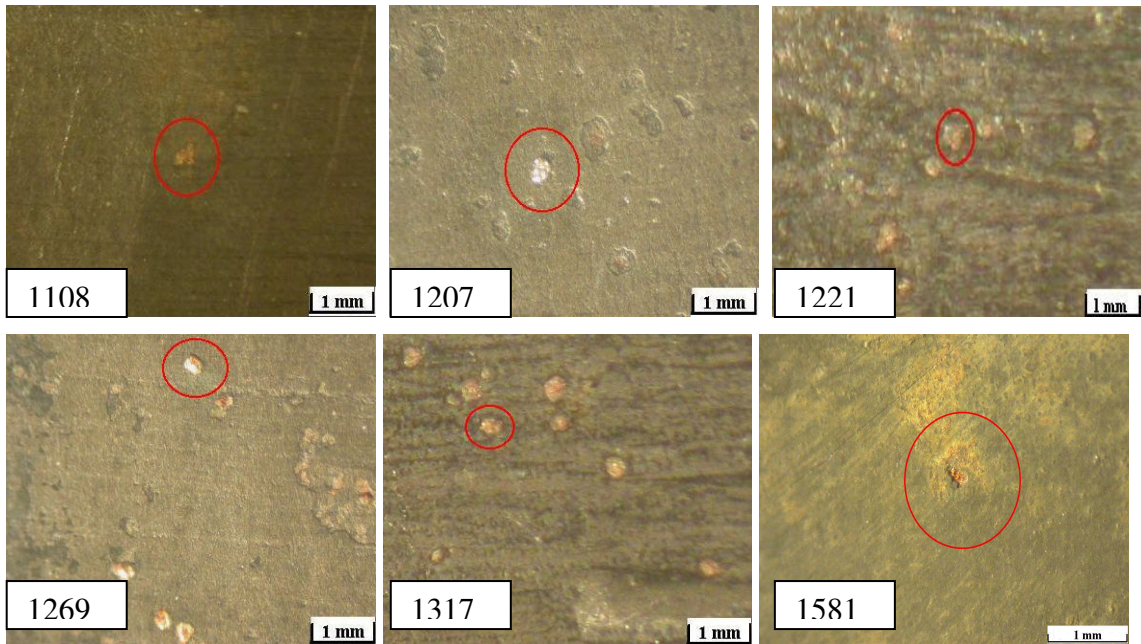
Figure 4.19. (Cont.)
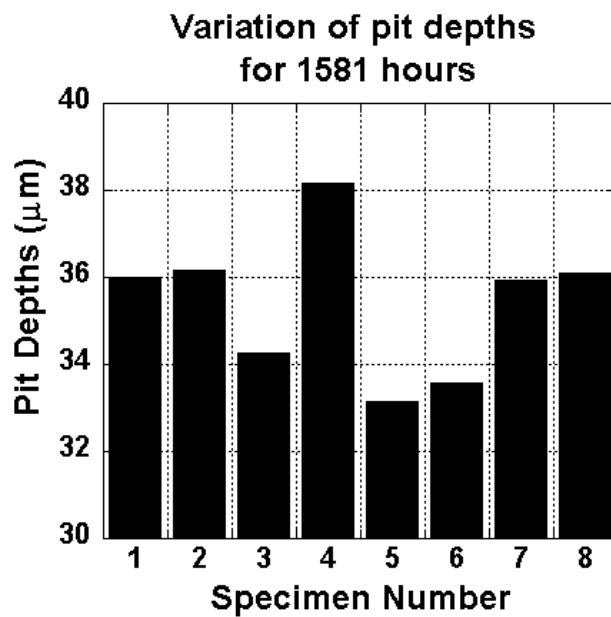
Figure 4.20. The maximum pit depths of 1581 h exposed specimens.

The thickness loss due to uniform corrosion and the maximum pit depth increase with increasing exposure time was shown in Figure 4.21. Thickness loss after 1581 h exposure is about 3.220 μm even though the weight loss of specimen is merely due to uniform corrosion. While at the same exposure time, the measured maximum pit depth is about 38 μm, pointing out a higher rate of pitting corrosion in the steel investigated. This tendency is more clearly seen in Figure 4.22, in which the maximum pitting

corrosion rate is drawn as function of exposure time. Although, the maximum value of the maximum pit depth rate is much higher, 1.450 μm/day, the average maximum pit depth corrosion rate is 0.617 μm/day, comparable higher than uniform corrosion rate.
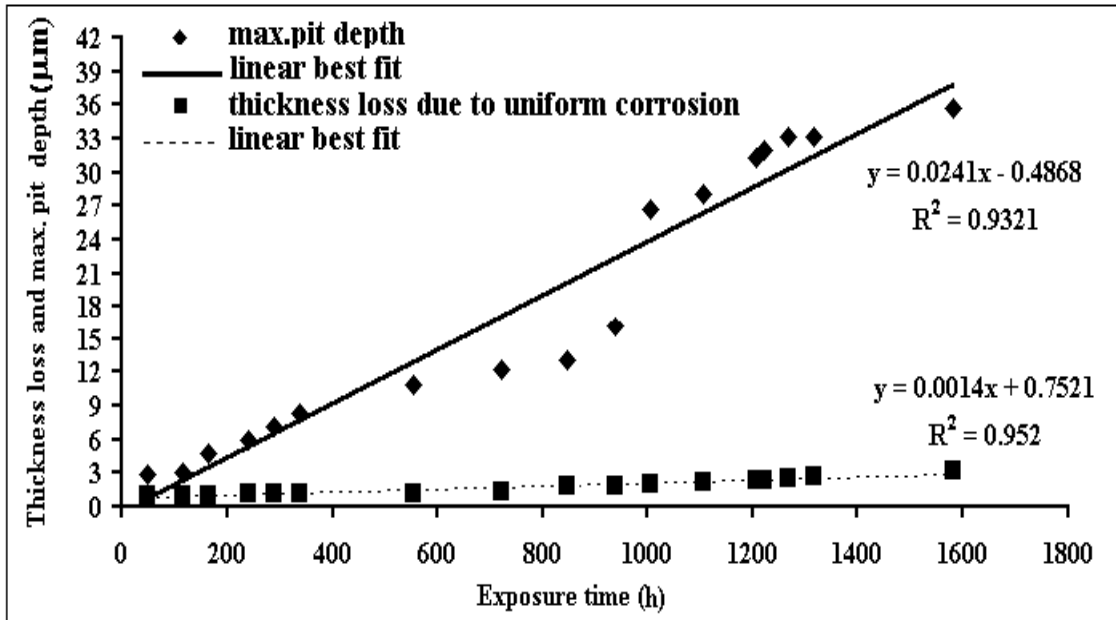
Figure 4.21. Maximum pit depth and thickness loss as function exposure time at 0.02 m/s fluid velocity.
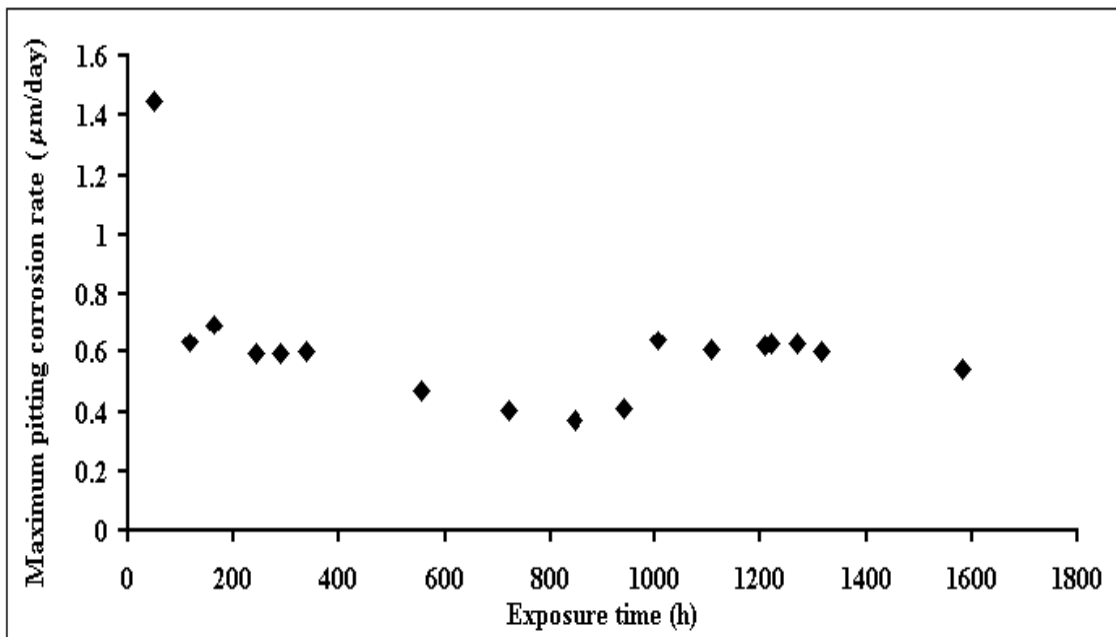
Figure 4.22 Maximum pitting corrosion rates *vs.* Exposure time of St-37 steel at 0.02 m/s fluid velocity.

The typical stress-strain curves of the test specimens after prescribed exposure times are shown in Figure 4.23. Tensile tests were performed following the maximum pit depth measurements. The variation of ultimate tensile strength (UTS) of the steel specimens as function of exposure time is also shown in Figure 4.24. The UTS values show a tendency of decreasing with increasing exposure time and/or maximum pit depth. The UTS of the specimens decreases from 374.58-381.64 Mpa in uncorroded specimens to 364.27-367.71 in the specimens exposed 1581 h. The yield point elongation is also found to elongated in the corroded specimens as compared with uncorroded specimens. As is expected, pits as defects on the surface may act as stress risers, notch and/or crack under tensile forces and may lead to reductions in the UTS values. It is also anticipated that uniform corrosion will results in a homogeneous thickness reduction along the surfaces of the test specimen and therefore the reductions in UTS values is attributed partly to the presence of pits in various depths on the specimen surface. It may also possible that the fluid temperature may induce microstructural changes that may also affect the mechanical properties. The extend of these effects on the UTS of the specimens are however not understood. The increase in the yield point elongation in the exposed specimens may be an indication of the strain aging of the steel specimens in hot geothermal fluid. The increased upper yield point of the exposed specimens shown in Figure 4.24 also tends to comform this phenomenon. Finally, the variations of the UTS values of the uncorroded and corroded specimens of 1581 h exposure are shown in Figure 4.25(a) and (b), respectively. These figures clearly show the reduction of the UTS on the average at higher exposure times.
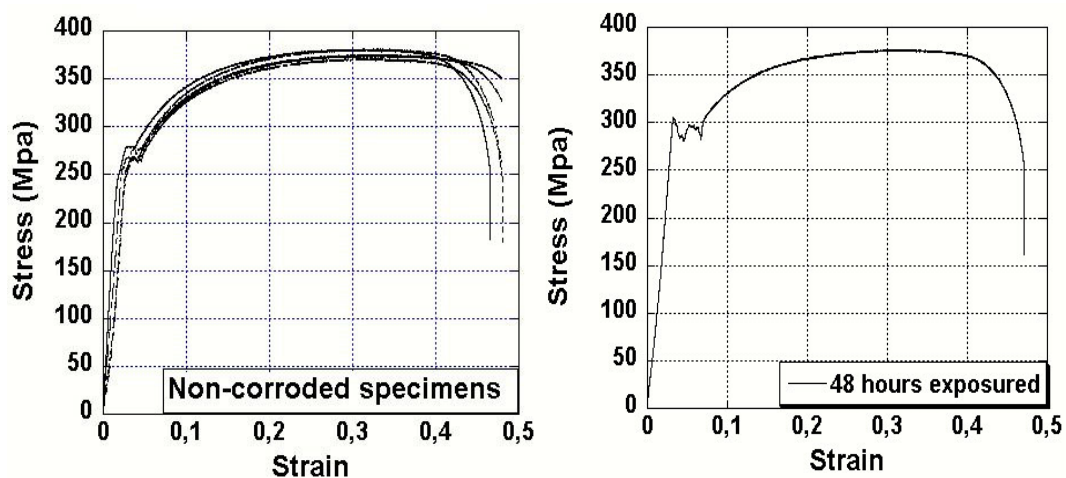
Figure 4.23. Stress-strain curves of St-37 carbon steel specimens for increasing exposure times.
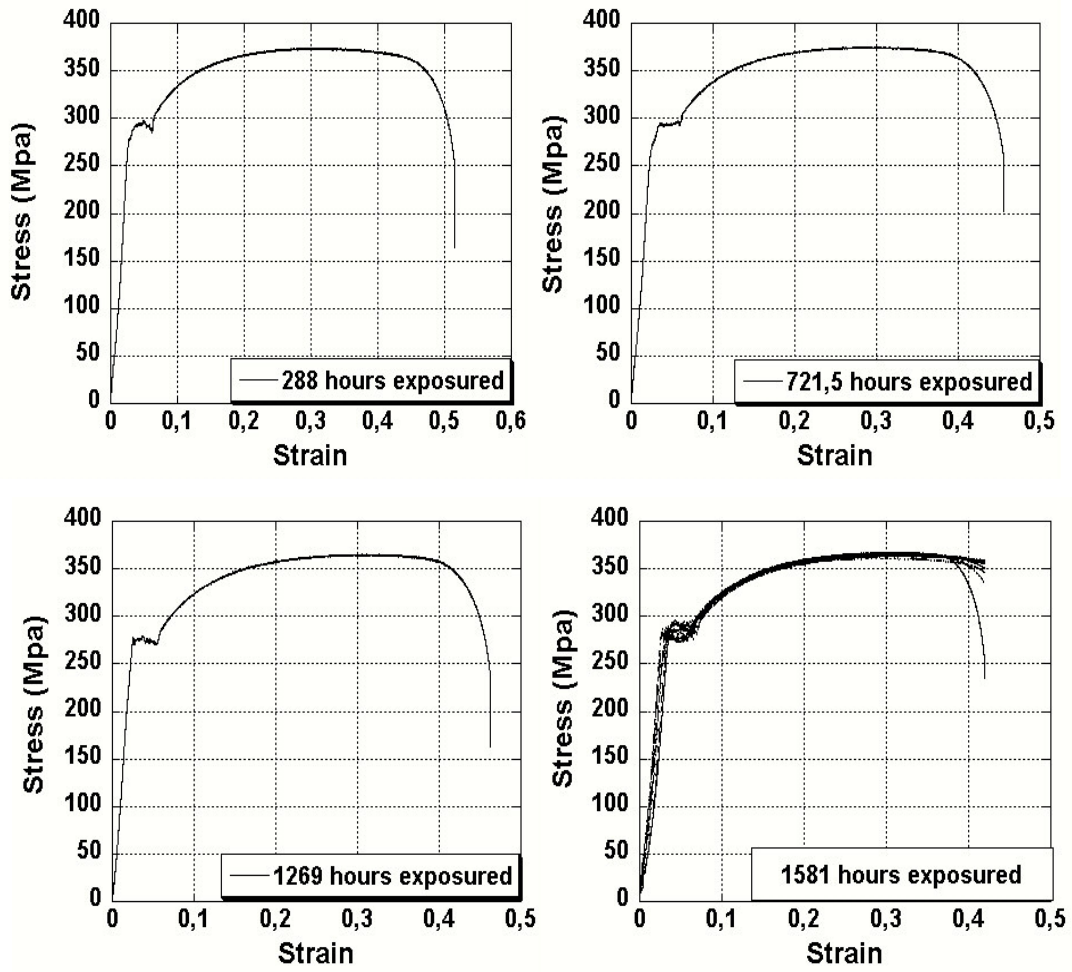
Figure 4.23. (Cont.)
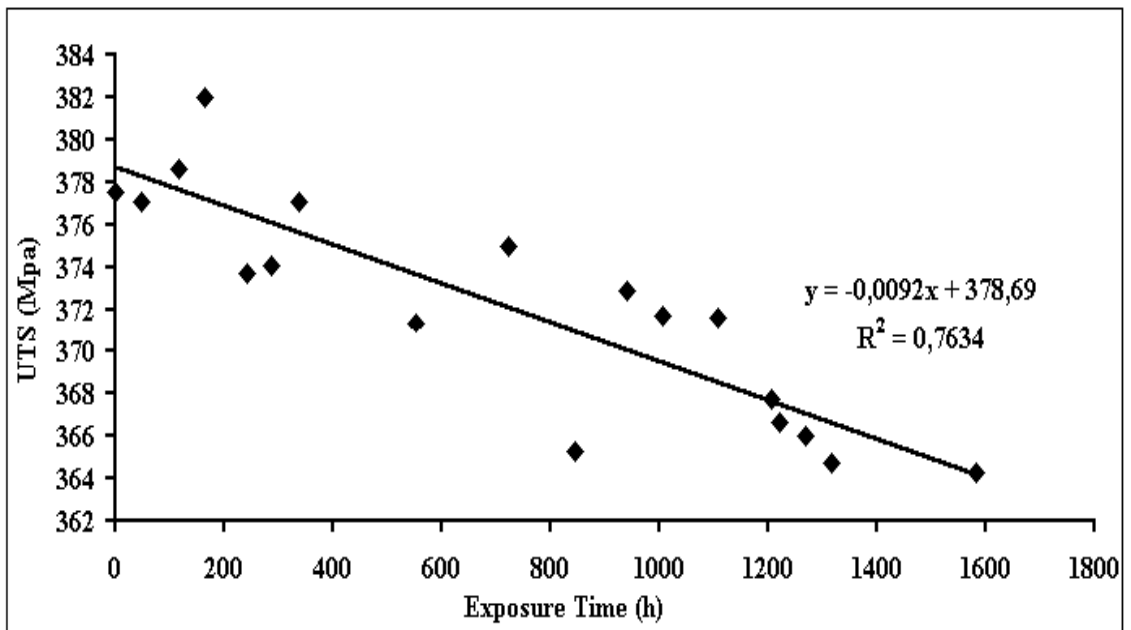
Figure 4.24. UTS *vs.* exposure time.
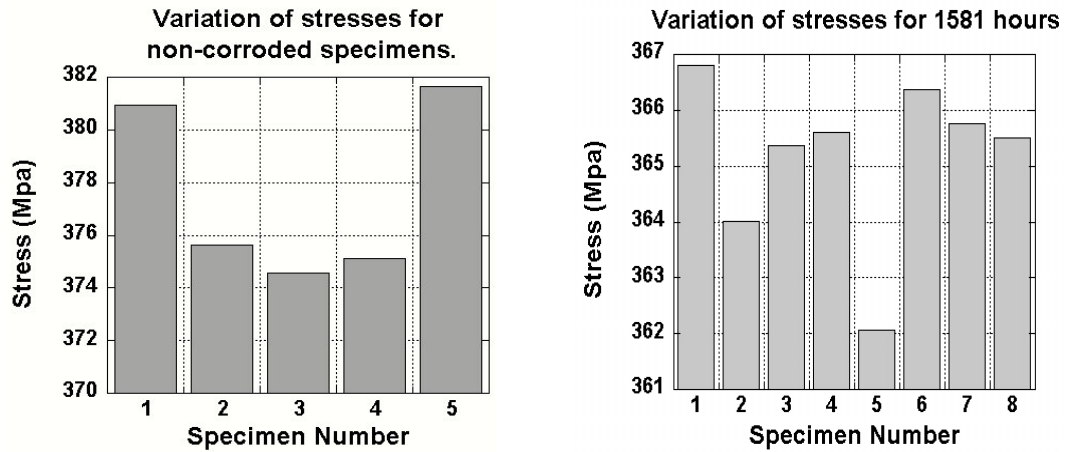
Figure 4.25. The variation of UTS values of the specimens (a) uncorroded and (b) exposed 1581 h.

The bursting pressures of a two inch schedule 40 pipeline (60.3 mm outside diameter and 3.91 mm wall thickness according to ASTM A53-94) calculated using DnV 1996, Norway standarts "Rules for Subsea Pipeline Systems" (Eqn. 3.8) and Eqn. 3.9 that include the pit length effect to the bursting pressure are shown as function of service time (month) in Figure 4. 26 and 4.27, respectively. In these calculations, the increase of the pith depth and decrease of the UTS with the service time were determined by linear fitting to the data given in Figure 4.21 and 4.24 , respectively.
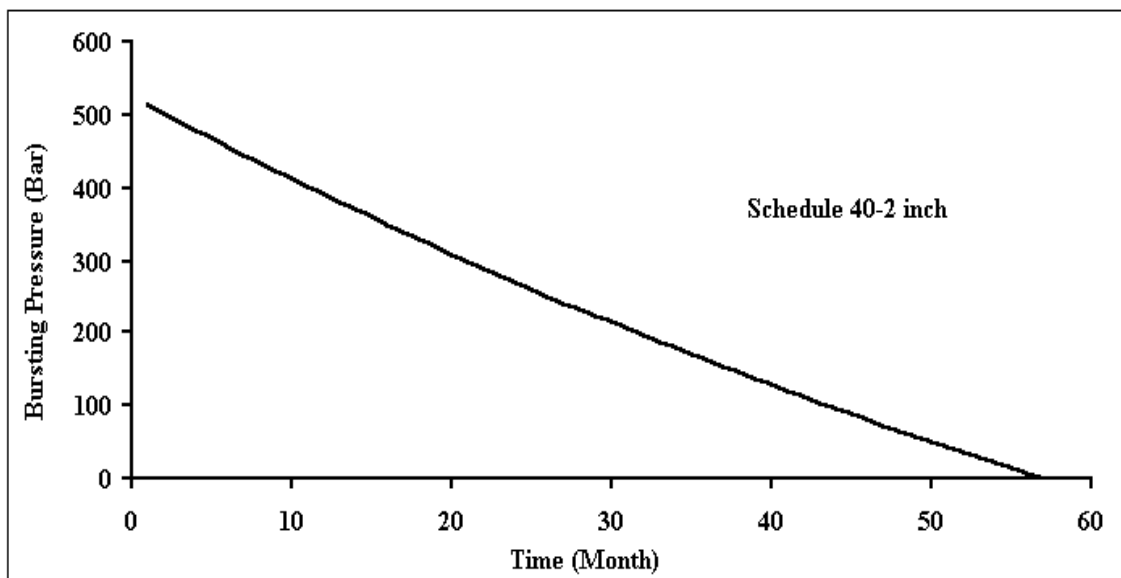
Figure 4.26. Bursting Pressure vs. service time of St-steel at low velocity fluid flow based on DnV 1996, Norway standarts (Eqn. 3.8)

The pit length rate was taken as 8.72 μm/day on the average. Assuming a pipeline operating under 4 bars fails to operate, a two inch schedule 40 pipe will fail after about 57 months, due to pitting corrosion and internal hydrolic pressure, according to calculations and curves shown in Figure 4.26 and Figure 4.27.
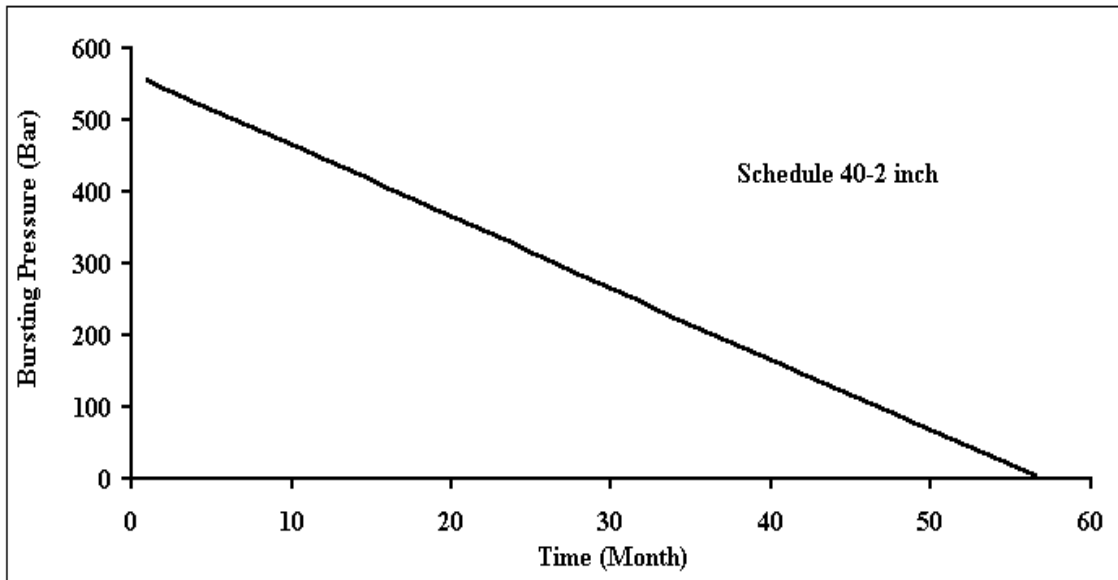
Figure 4.27 Bursting Pressure vs. service time of St-steel at low velocity fluid flow based on the Eqn. 3.9

4.3. The Corrosion Behavior of St-37 Steel at High Fluid Velocity

4.3.1 Corrosion Rate and Products

The measured weight loss and corrosion rate vs. exposure time graphs of St-37 steel at 9.6 m/s fluid velocity are shown in Figure 4.28(a) and (b), respectively. The maximum exposure time in these graphs is nearly 1600 h, corresponding to a 60-day exposure. Similar to low fluid velocity corrosion tests, the initial high uniform corrosion rate decreases as the exposure time increases and the uniform corrosion rate reaches a constant value of 0.022 mm/yr after about 700 h as seen in Figure 4.28(b). The uniform corrosion rate is increased about 25% as compared with low fluid velocity tests. The initial high corrosion rate decreases with increasing exposure times, since the corrosion products precipitating scaled on the surface of the test specimen as the exposure time

increased, hence formed a barrier between steel surface and geothermal water. The higher uniform corrosion rate at higher velocities is explained based on the morphology of the corrosion products.
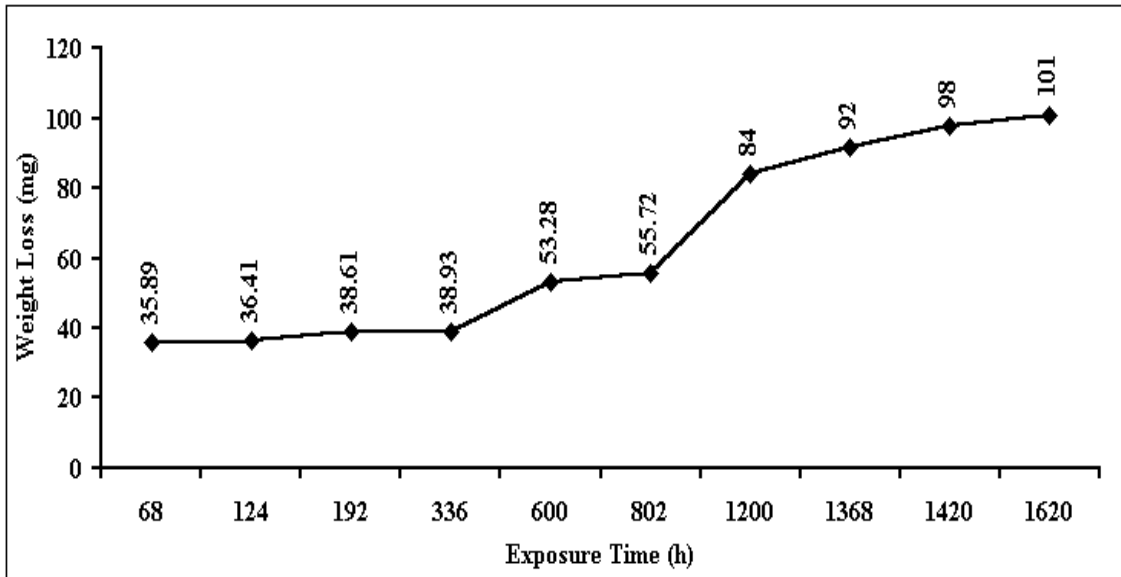
(a)
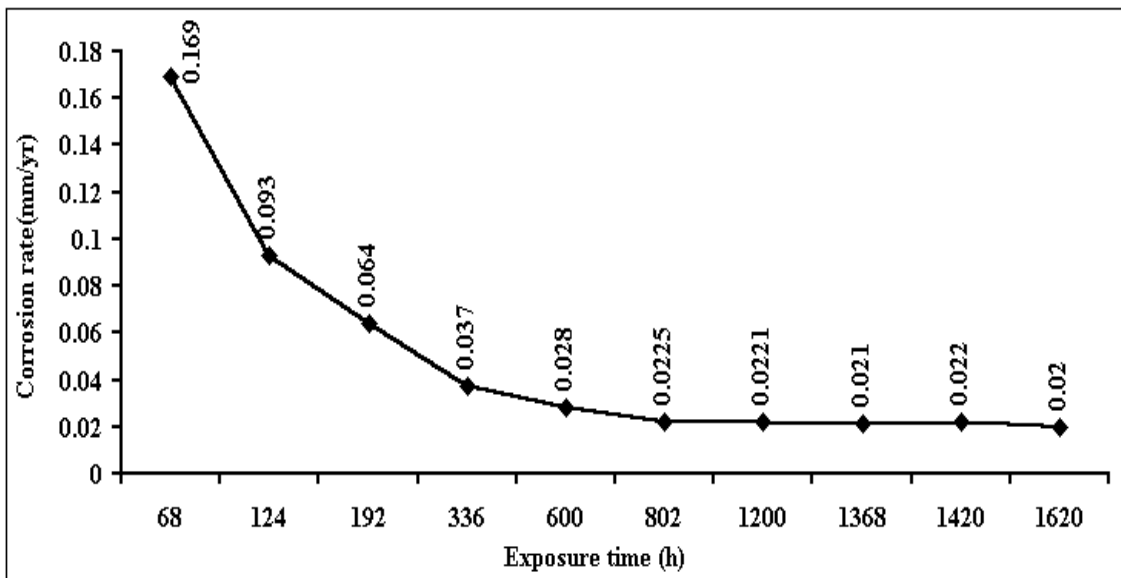
(b)

Figure 4.28. Weight loss and corrosion rate *vs.* exposure time for st-37 at fluid velocity of 9.6 m/s.

Figures 4.29 (a) and (b) show the SEM micrographs of the surfaces of the samples after 336 and 802 h exposure to the fluid, respectively. At 336 h exposure time, the measured corrosion rate of the specimen is about 0.037 mm/yr, higher than that of

specimen tested at 0.002 mm/s (0.031 mm/yr). The increase of the corrosion rate at a higher fluid velocity is attributed to the crystal form of the corrosion products as clearly seen in Figure 4.29 (c). The porosities between the crystals of the corrosion layer may permit a higher rate of fluid flow to and/or contact with the specimen surface as compared with the surface layer formed at 0.002 m/s fluid velocity. The crystal form of the corrosion products also differentiates the high fluid velocity corrosion from the low velocity corrosion of the steel.

(a)

(b)

(c)
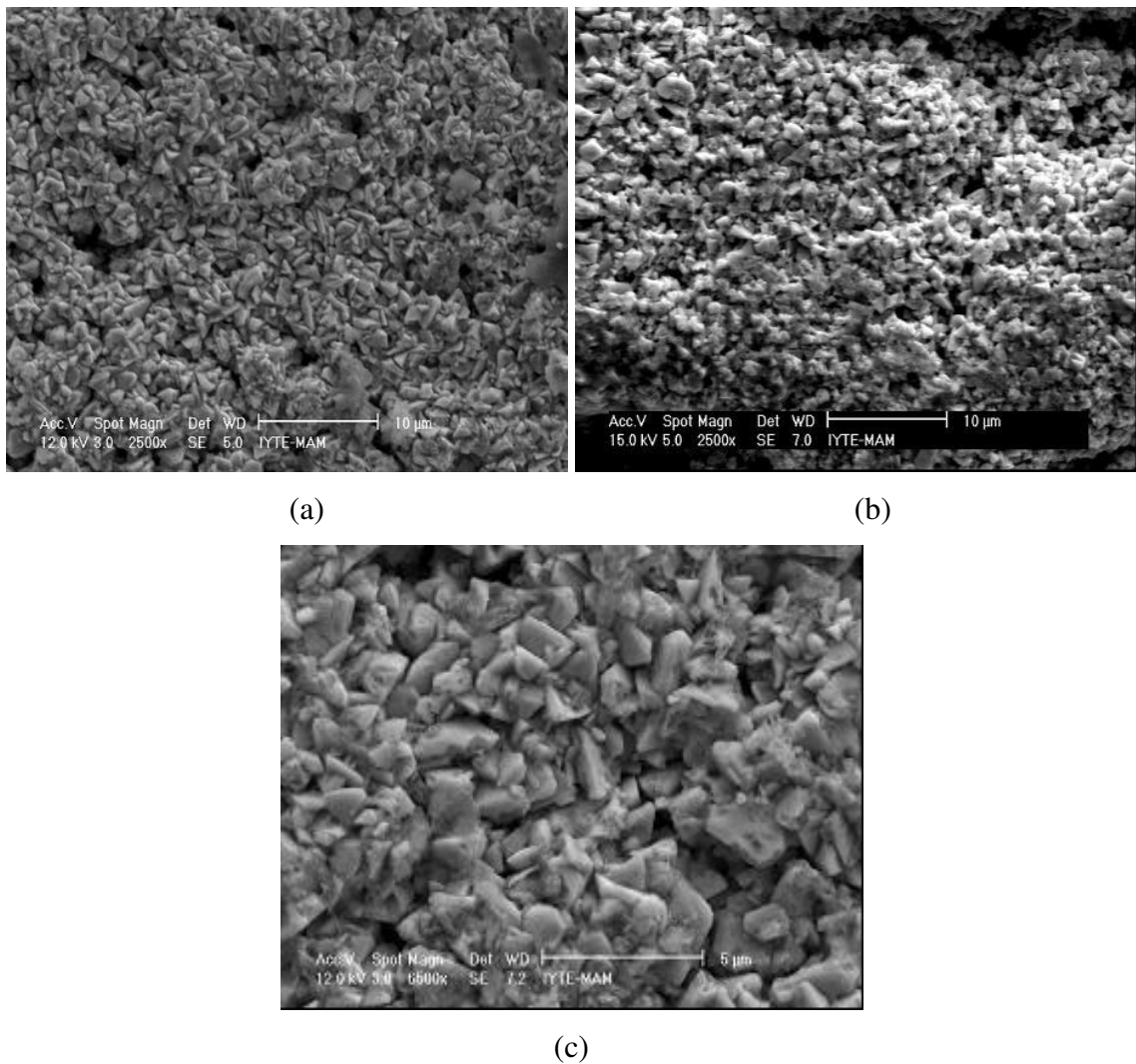
Figure 4.29. SEM surface images of specimen after exposure times of (a) 336, (b) 802 and (c) 336 h (magnified).

Additionally, the higher fluid velocity may increase the attack to the steel by increasing the amount of oxygen, carbon dioxide or hydrogen sulfide in contact with the metal surface. The higher velocity may also increase diffusion or transfer of ions by

reducing the thickness of the stagnant film at the surface. On the contrary, high fluid velocity may prevent the development of the tubercle structures by continuously removing such structures from the surface. The EDX analyses of the corrosion products of the specimens at 336 and 802 h exposure are shown in Figure 4.30(a) and (b), respectively. In all tested specimens, similar to test specimens at low fluid velocity, the EDX analyses showed the presence of the following elements: C, O, Mg, Si, S, Sb and Fe. The compositions of the corrosion products at these three different exposure times are also tabulated in Table 4.2. It is noted in the table, although C, O and Fe concentration increase with increasing exposure time from 336 to 802 h, Sb concentration decreases at higher exposure times, a behavior very similar to the low velocity test specimens.
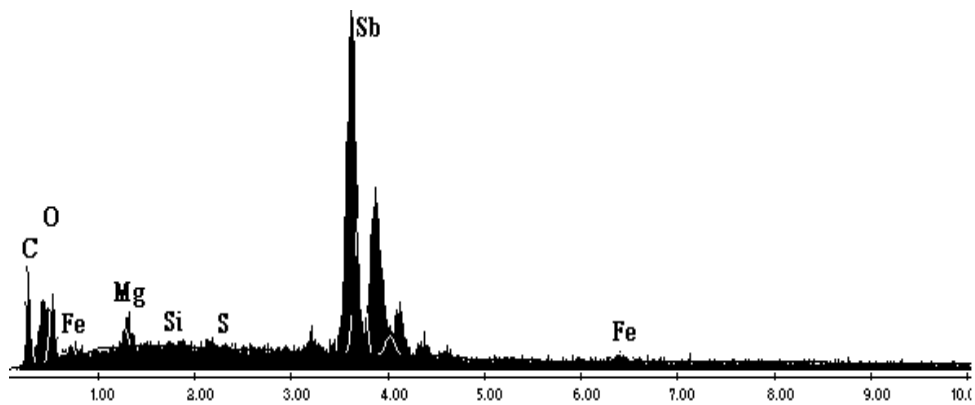
(a).
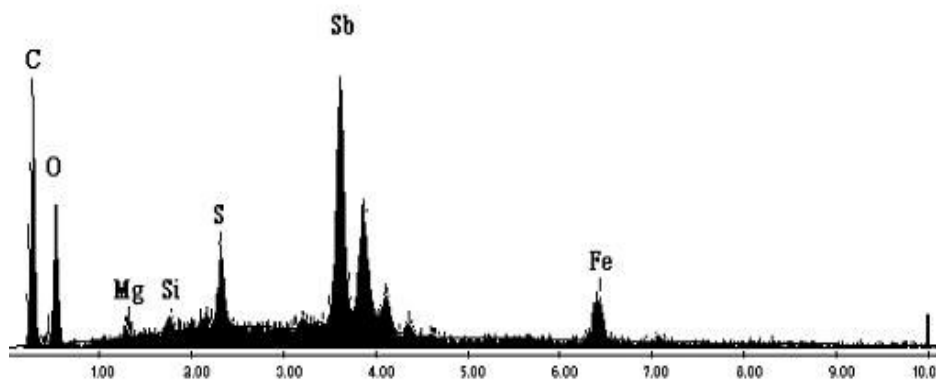
(b)

Figure 4.30. EDX analyses of corrosion products at exposure times of (a) 336 and (b) 802 h

Table 4.2. EDX analyses results of the tested St-37 specimens at two different exposure times.

Element Wt%	336 h	802 h
C	5.57	31.04
O	4.90	8.94
Mg	1.47	0.63
Si	0.24	0.73
S	0.33	3.17
Sb	84.30	43.48
Fe	3.19	12.01

In Figure 4.31, the cross-section of the corrosion layer formed on a sample of 336 h exposure is shown. The sample was prepared in a similar way of low velocity test samples as explained before in this section. As in the case of low velocity test samples, the epoxy mount detached from the surface of the steel. EDX analysis were performed to the regions designated as "A", "B", "C" and "D" in Figure 4.31 and results are shown sequentially in Figures 4.32 (a), (b), (c) and (d). It is seen in Figures 4.32 (a-d), Sb concentration increases near the surface of the specimen, a behavior similar to low velocity tests specimens.
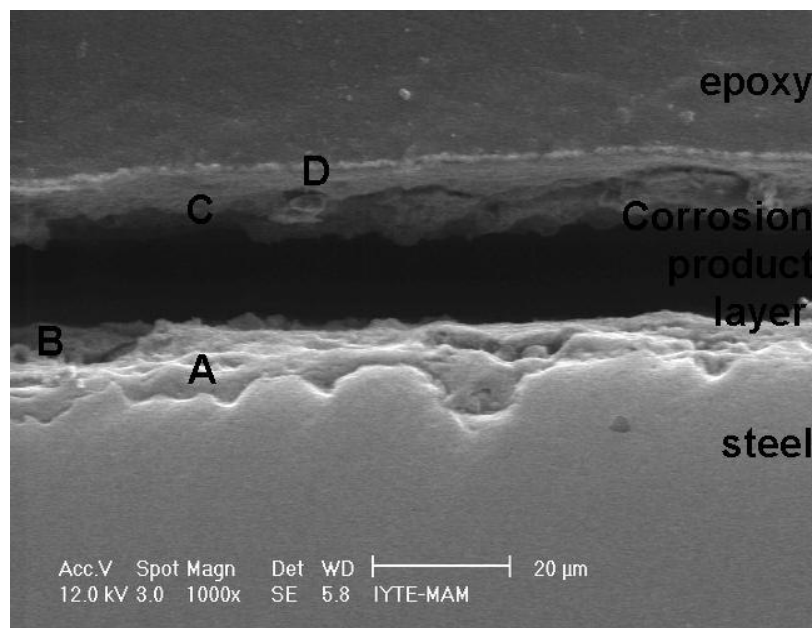
Figure 4.31. The epoxy-mounted and polished cross-section SEM image of an St-37 sample (336 h), showing the split corrosion layers marked as A, B, C and D.

Element	Wt%	At%
C	38,02	56,15
O	30,86	34,23
Mg	0,33	0,24
Si	0,34	0,22
S	0,41	0,23
Sb	3,61	0,53
Fe	26,42	8,4

(a)

Element	Wt%	At%
C	75,99	85,84
O	14,62	12,40
Mg	0,25	0,14
Si	0,33	0,16
S	0,29	0,12
Sb	5,53	0,62
Fe	3,00	0,73

(b)

Element	Wt%	At%
C	18,56	51,20
O	7,84	16,25
Mg	0,80	1,09
Si	0,62	0,74
S	2,67	2,63
Sb	41,26	11,23
Fe	28,24	16,76

(c)

Element	Wt%	At%
C	12,05	49,02
O	4,15	12,66
Mg	1,55	3,11
Si	0,34	0,59
S	0,39	0,59
Sb	78,74	31,59
Fe	2,78	2,43
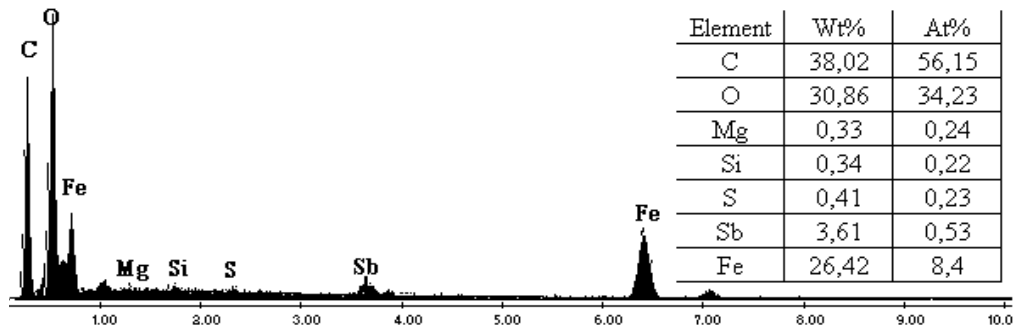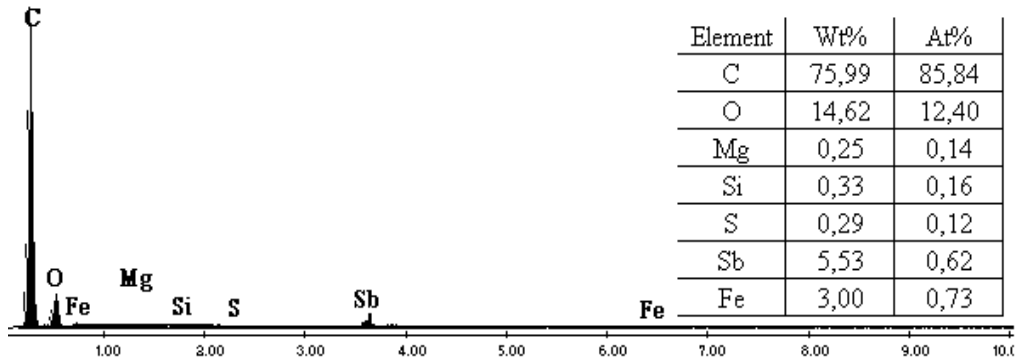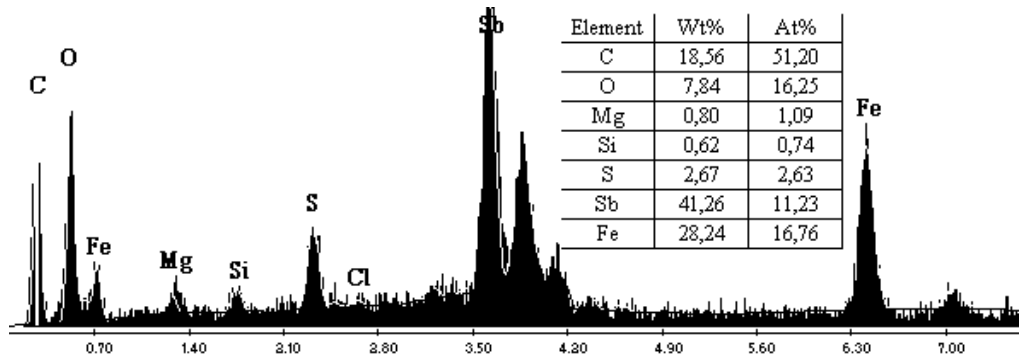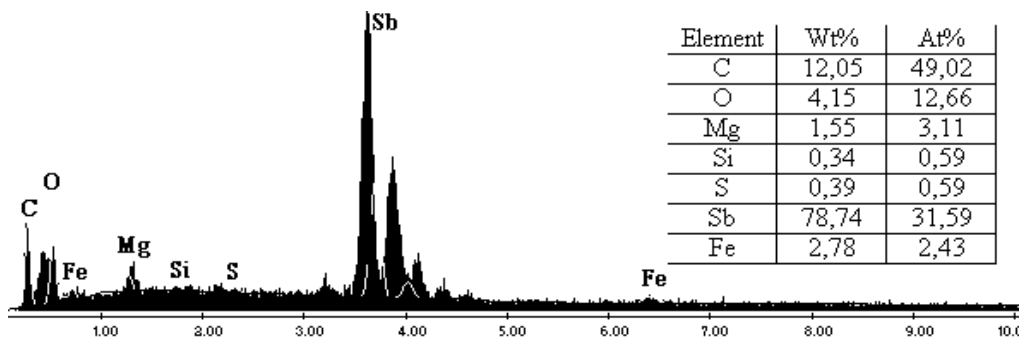
(d)

Figure 4.32 EDX analyses results of the cross-sections shown in Figure 4.31, regions: (a) A, (b) B, (c) C and (d) D.

81

The SEM cross-section image of the corrosion layer formed on a sample of 802 h exposure is shown in Figure 4.33. Corresponding EDX analyses of the split corrosion layers marked as A and B in this figure are shown in Figures 4.44(a) and (b), respectively. Similar to 336 h exposure, at this exposure time EDX analysis shown in Figures 44(a) and (b) show the presence of S, Mg, C, O, Fe, Sb and trace amount of Si in the corrosion product layer.
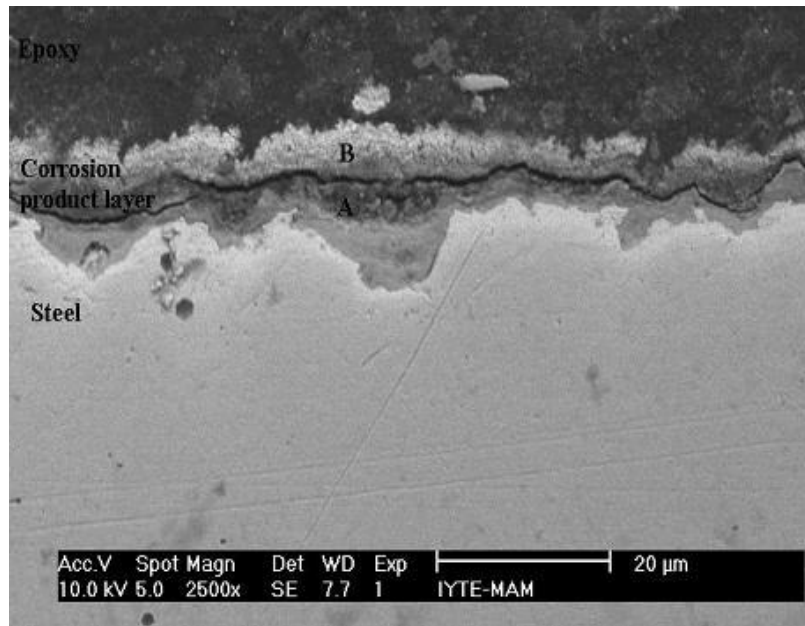
Figure 4.33. The epoxy-mounted and polished cross-section SEM image of an St-37 sample (802 h), showing split corrosion layers marked as A and B.   .

Element	Wt%	At%
C	21,86	42,89
O	22,07	32,51
Mg	2,43	2,36
Si	1,48	1,24
S	8,84	6,49
Sb	16,50	3,19
Fe	26,82	11,32

(a)
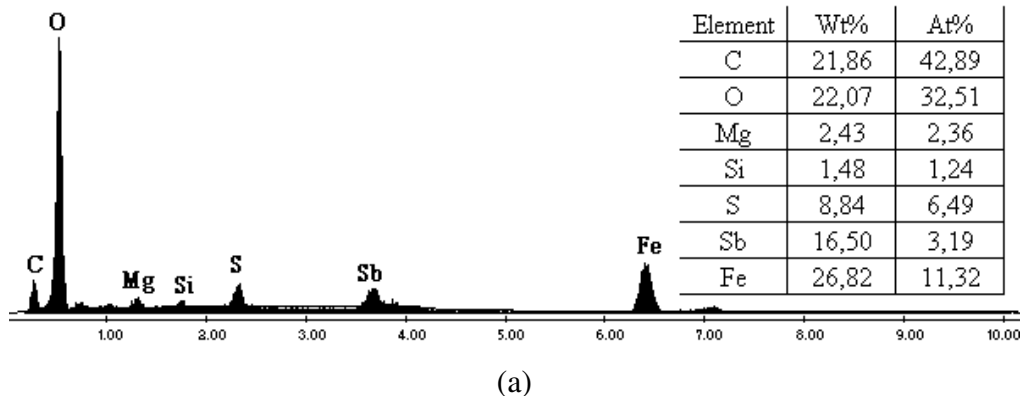
Figure 4.34. EDX analyses results of the cross-sections shown in Figure 4.32, (a) section A and (b) section B.

Element	Wt%	At%
C	11,92	40,48
O	8,11	20,69
Mg	0,87	1,45
Si	0,83	1,21
S	2,91	3,71
Sb	57,11	19,14
Fe	18,25	13,33
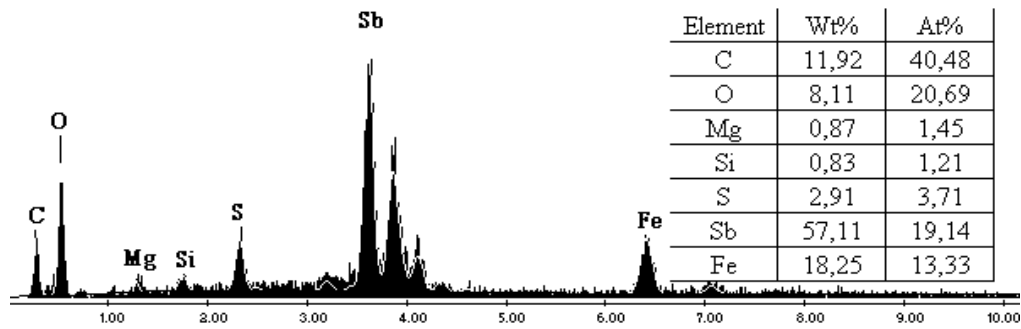
(b)

Figure 4.34. (Cont.)

At both exposure times, in the samples tested in high velocity tests, a relatively high concentration of Sb is detected near the surface as compared with low velocity tests specimens. The region of relatively high Sb concentration was at distance approximately 5 μm from the surface. There was also a tendency of increasing sulphur concentration from the surface to the interior of the corrosion layer. An SEM image of a sulfur reducing bacterium is shown in Figure 4.35. The number of SRB however greatly reduced in these samples as compared with the samples exposed to lower fluid velocity tests. On the other hand, the tubercle structures, which were found in the samples of lower fluid velocity tests, were not microscopically detected on the surfaces of the specimens exposed to higher fluid velocity.

Figure 4.35. SEM image of a sulphate reducing bacterium.

The XRD analyses of the corrosion products recovered after cleaning of the surfaces of the specimens showed similar corrosion products in 336 and 802 h exposed samples and they are composed of elemental iron and antimony, ferrisilicate (FeSi), gupelite (Fe_3Si) and carbon sulfide (CS_2) as shown in Figure 4.36. Mackinawite (FeS) and valentinite (Sb_2O_3) detected in the low fluid velocity tests are not found in the high velocity tests. The lack or nondetectable amount of FeS at this fluid velocity proved the insignificant SRB activity in corrosion process.
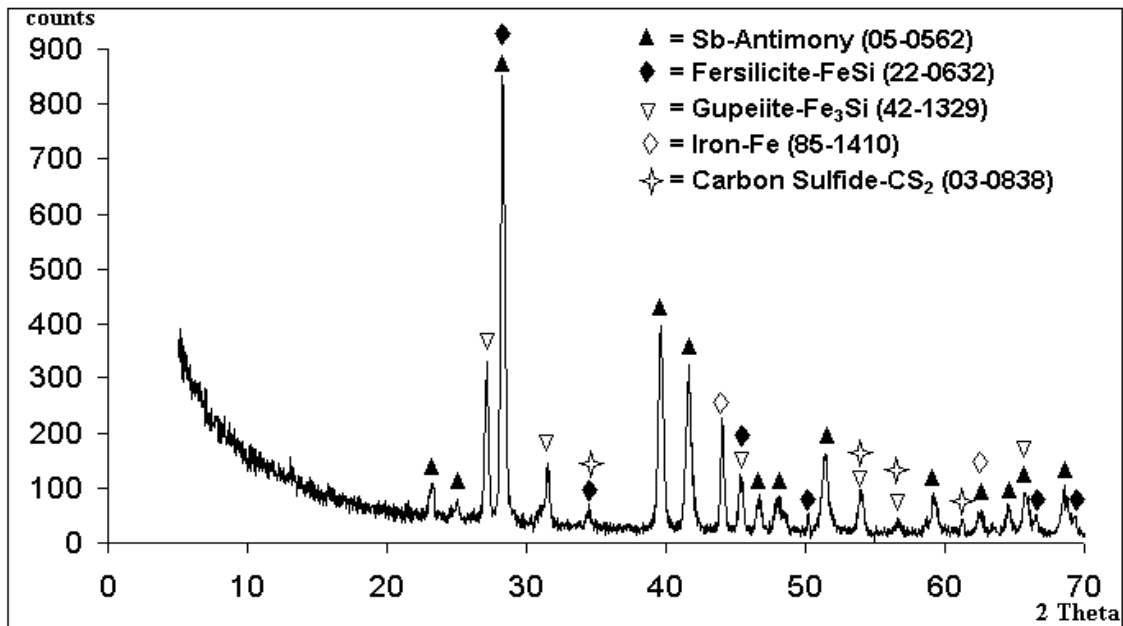
Figure 4.36. Typical XRD analysis of the corrosion products after 336 and 802 h exposure.

4.3.2. Pit depth, Mechanical Properties and Service Life at High Velocity Fluid Flow

The optical microscope images of the pits formed at increasing exposure times are shown in Figure 4.37. The pits of the maximum depth are circled in the same figure for each exposure time. Figure 4.37 shows an increasing trend in the pit lengths at increasing exposure times. The maximum pit length of the pits of maximum depth was approximately 0.88 mm, the same as the low velocity test specimens and detected in the specimens after 1420 and 1620 h exposure. From the maximum, minimum and average pith lengths, the maximum, minimum average pitting length rates were calculated and

found 19.354,7 and 11.85 µm/day, respectively. Similar to the low fluid velocity tests, the pit shapes were found shallow wide, vertical grain and elliptical.
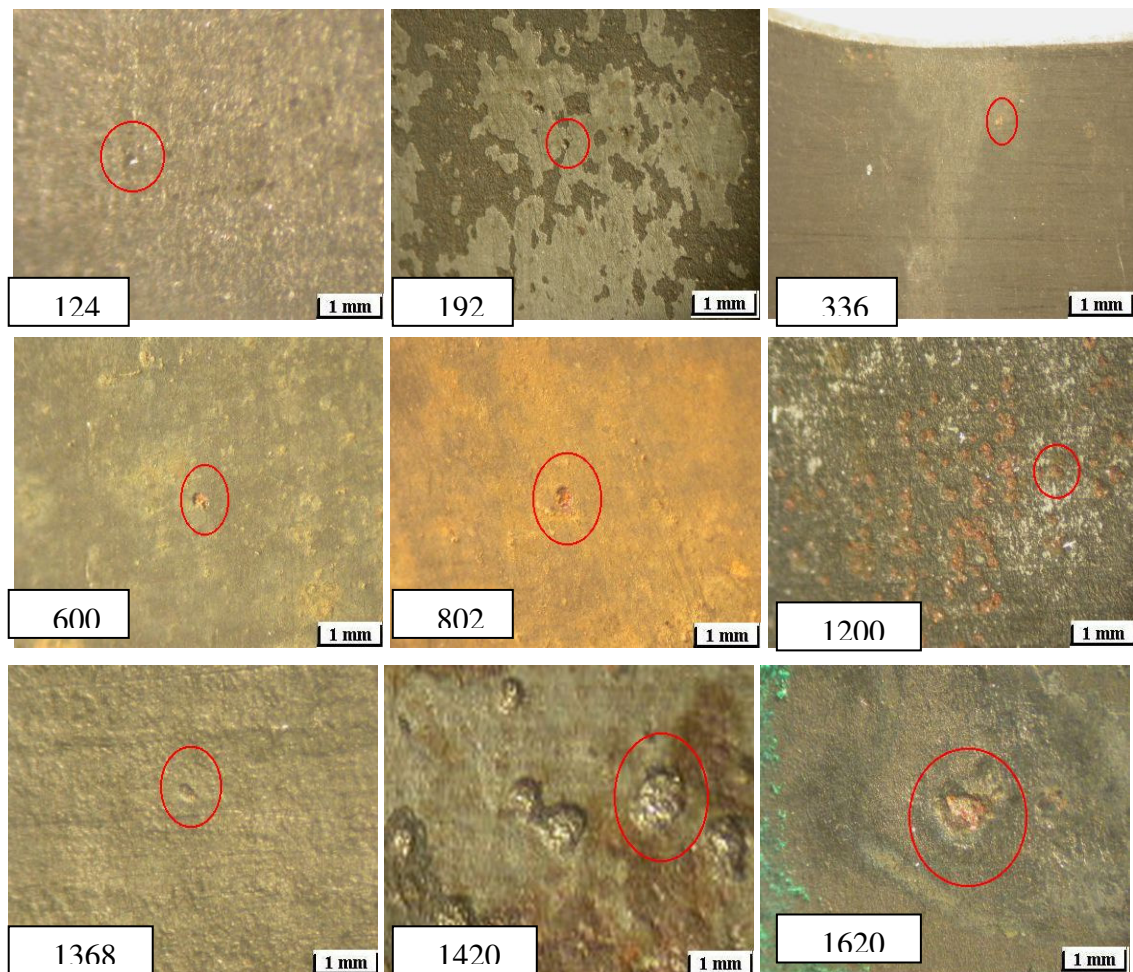
Figure 4.37. Stereo zoom microscope images of the pits formed on surfaces of St-37 steel at increasing exposure times.

The thickness loss due to uniform corrosion and the maximum pit depth increase with increasing exposure time as shown in Figure 4.38. Thickness loss at 1620 h exposure is about 3.71 µm while the measured maximum pit depth is 23.84 µm. At a similar exposure time, 1581 h, the thickness loss in the specimens tested at 0.02 m/s is however smaller, 3.220 µm, showing the lower rate of uniform corrosion rate in low fluid velocity tests, while the pit depth is comparably higher, 35.78 µm. The average maximum pit depth corrosion rate, 0.3 µm/day, is also comparable lower than that of the low velocity tests, 0.617 µm/day (Figure 4.39). The pits that are free of tubercle structure at this fluid velocity are probably filled with corrosion products at their initial growth state, causing the prevention of further pit growth.
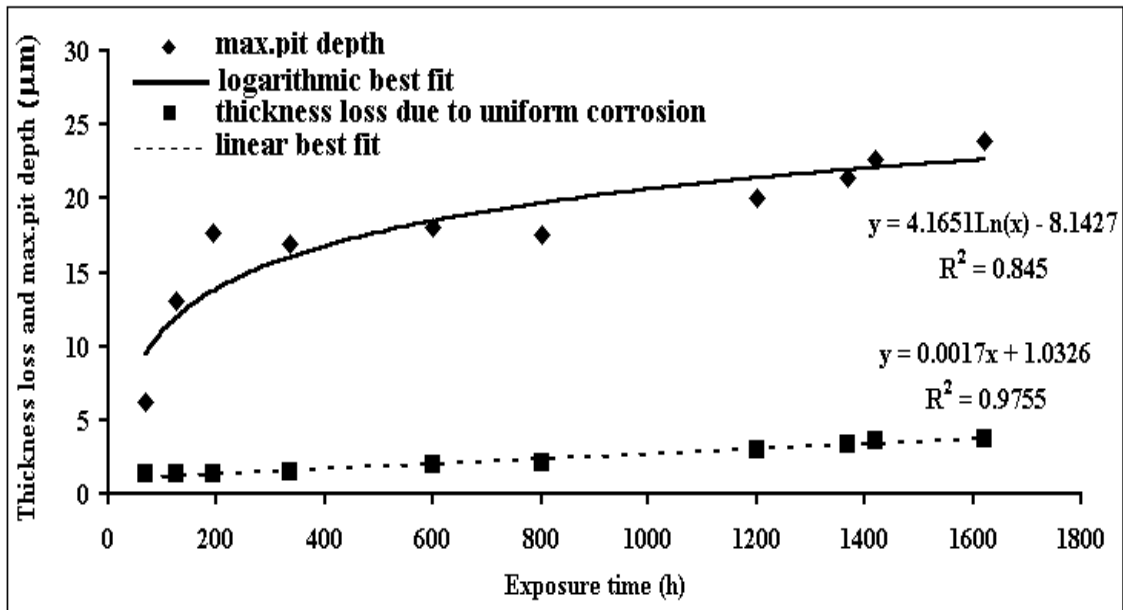
Figure 4.38. Maximum pit depth and thickness loss of specimens as a function of exposure time at 9.6 m/s fluid velocity.
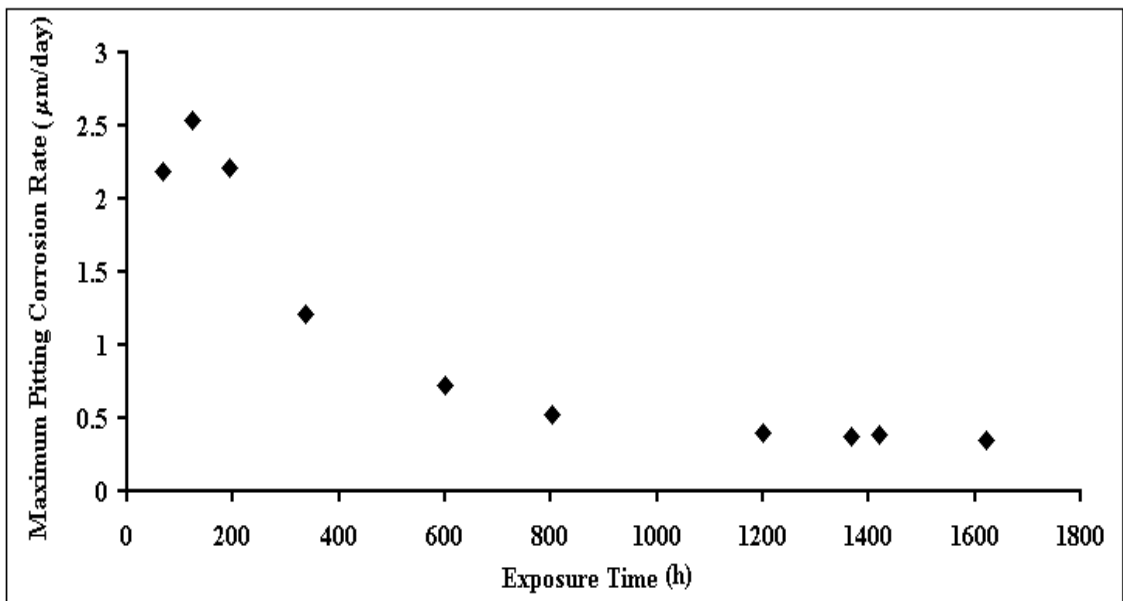
Figure 4.39. Maximum pitting corrosion rates vs. exposure time of St-37 steel at 9.6 m/s fluid velocity.

Typical stress-strain curves of the test specimens after prescribed exposure times are shown in Figure 4.40. The reductions in the UTS values at this fluid velocity are moderate (see Figure 4.41); from 374.58-381.64 MPa in uncorroded specimens to 370.17-374.79 MPa after 1620 h exposure. The increase in yield point elongation is also seen in the samples tested at high velocity.
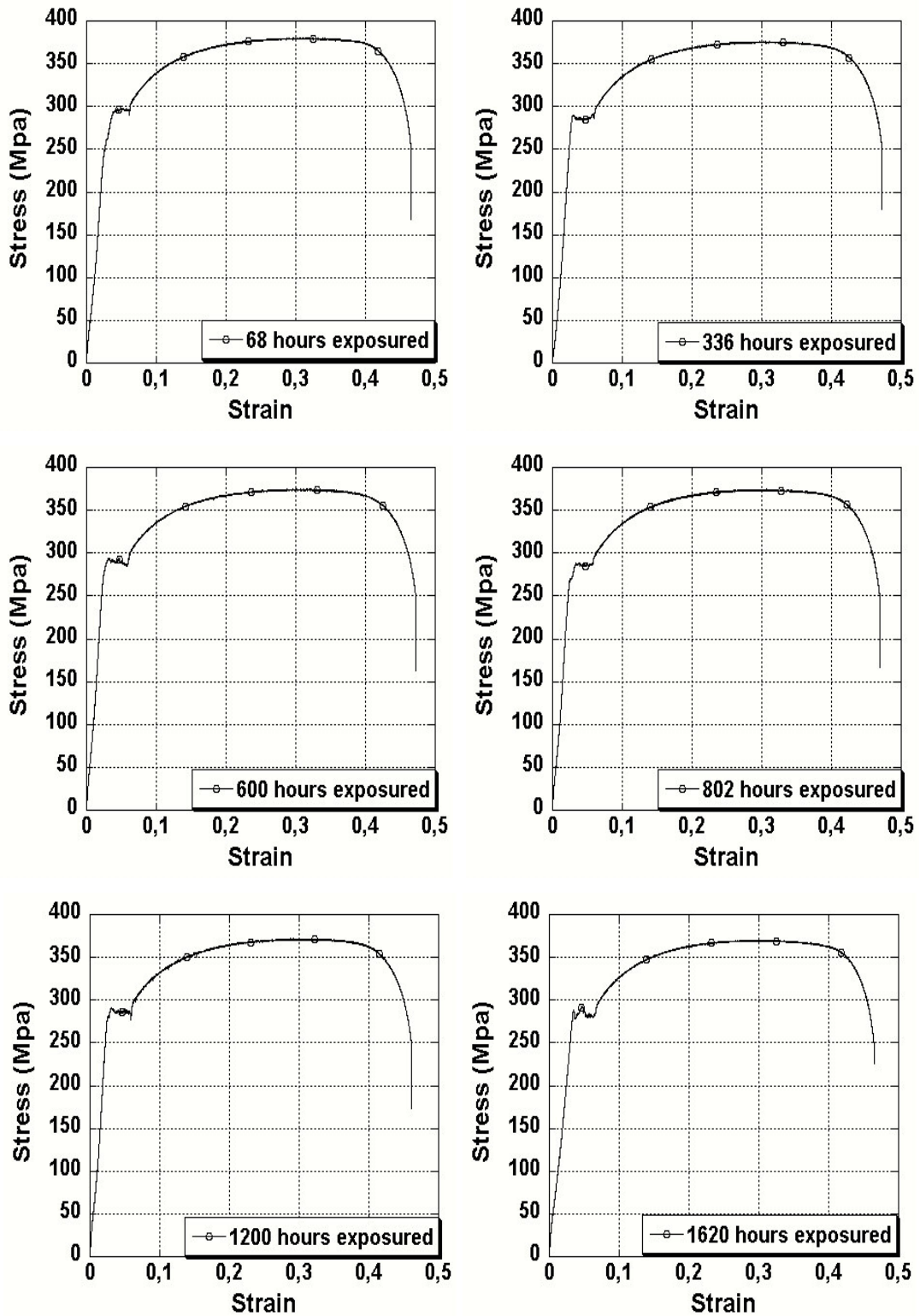
Figure 4.40. Stress-strain graphs of st-37 carbon steel specimens of increasing exposure time exposed to 9.6 m/s fluid velocity.

The bursting pressures of a two inch schedule 40 pipeline calculated using DnV 1996, Norway standards "Rules for Subsea Pipeline Systems" Eqn. 3.8 and Eqn. 3.9 are

shown as function of time of service (month) in Figure 4.42 and 4.43, respectively. The pit length rate was taken as 11,85 μm/day on the average. Both equations result in similar service life, about 95 months, which comparably higher than low velocity test specimens (57 months).
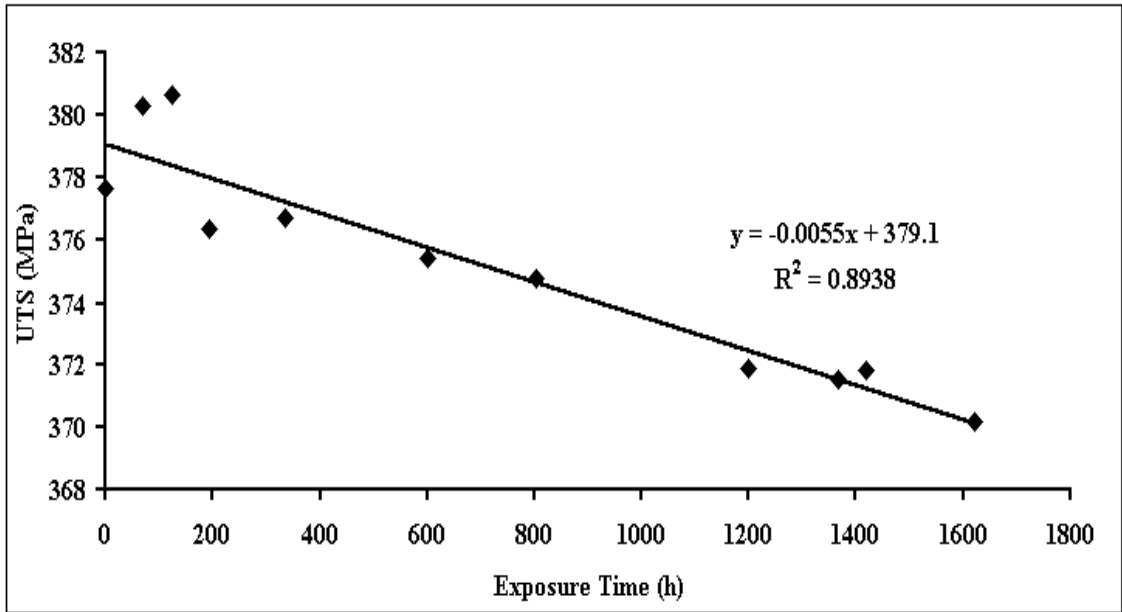
Figure 4.41 UTS vs. exposure time in samples exposed to high velocity of fluid.
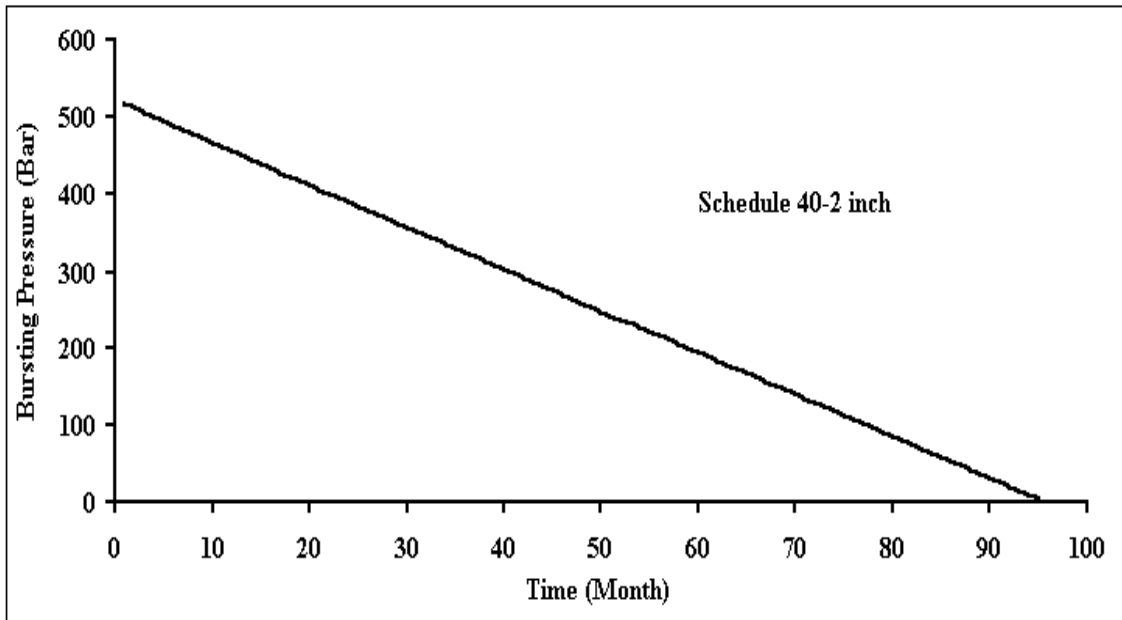
Figure 4.42. Bursting Pressure vs. service time of St-37 steel at high velocity fluid flow based on DnV 1996, Norway standards (Eqn. 3.8)
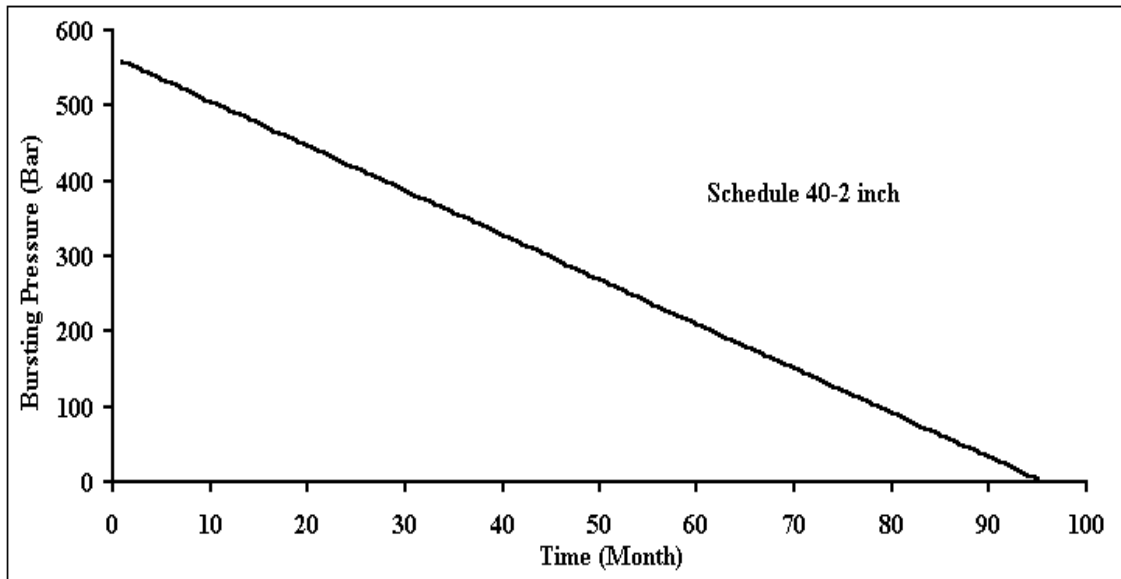
Figure 4.43. Bursting Pressure vs. service time of St-37 steel at high velocity fluid flow based on the Eqn. 3.9

4.4. The Corrosion Behaviour of Austenitic Stainless Steels in Geothermal Water.

The uniform corrosion rate of AISI 304, 316 and 316L austenitic stainless steels determined from the corrosion test coupons are sequentially 0.00034, 0.00011 and 0.00010 mm/yr for 0.02 m/s fluid flow (Figure 4.44) and 0.00039, 0.00026, 0.00018 mm/yr for 9.6 m/s fluid flow (Figure 4.45). The uniform corrosion rates of 316 stainless steels are found to increase about two or more times when the fluid velocity increases from 0.02 to 9.6 m/s, showing a predominant effect of fluid velocity on the corrosion rate. Figures 4.46 and 4.47 show the pictures of the specimens after 648 and 2000 h exposure to the geothermal fluid of velocities 0.02 m/s and 9.6 m/s respectively. At the low fluid velocity, the calcium carbonate scaling are seen both after 648 and 2000 h exposures, while at high velocity it forms slowly and after 600 h exposure the scale is hardly detected or very thin to be detected. After 2000 h exposure, the scaling is seen to cover the surfaces of the steel test coupons completely at both fluid velocities. These pictures clearly show a higher rate of calcium carbonate scaling at the lower fluid velocity. This also explains the lower rate of uniform corrosion at the low fluid velocity since a higher rate of calcium carbonate deposition is more effective in protecting the specimen surface contacting with fluid.
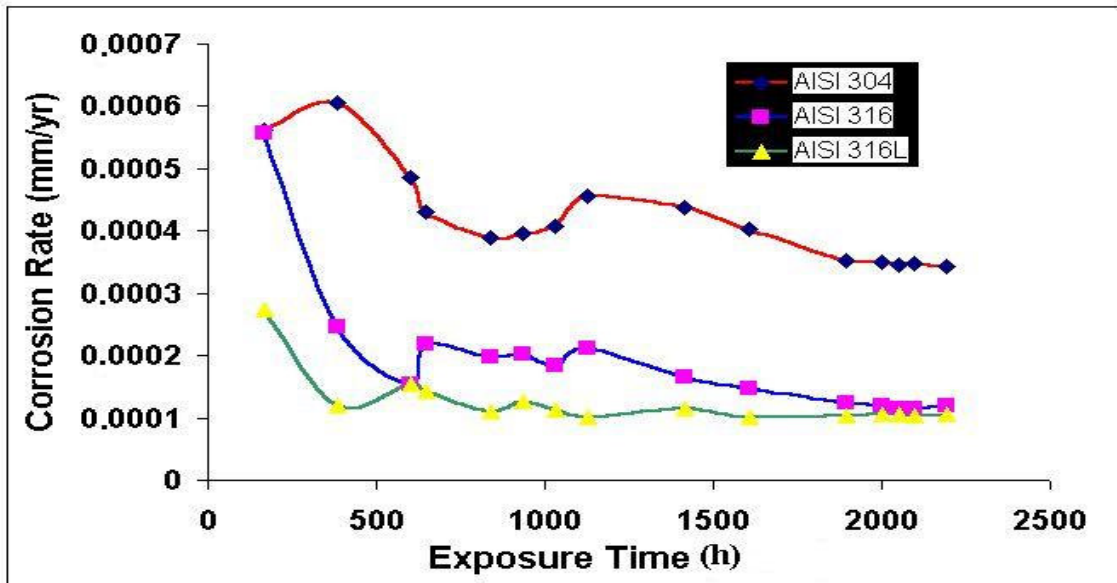
Figure 4.44. Corrosion rate vs. exposure time of stainless steels specimens tested at 0.02m/s fluid velocity.
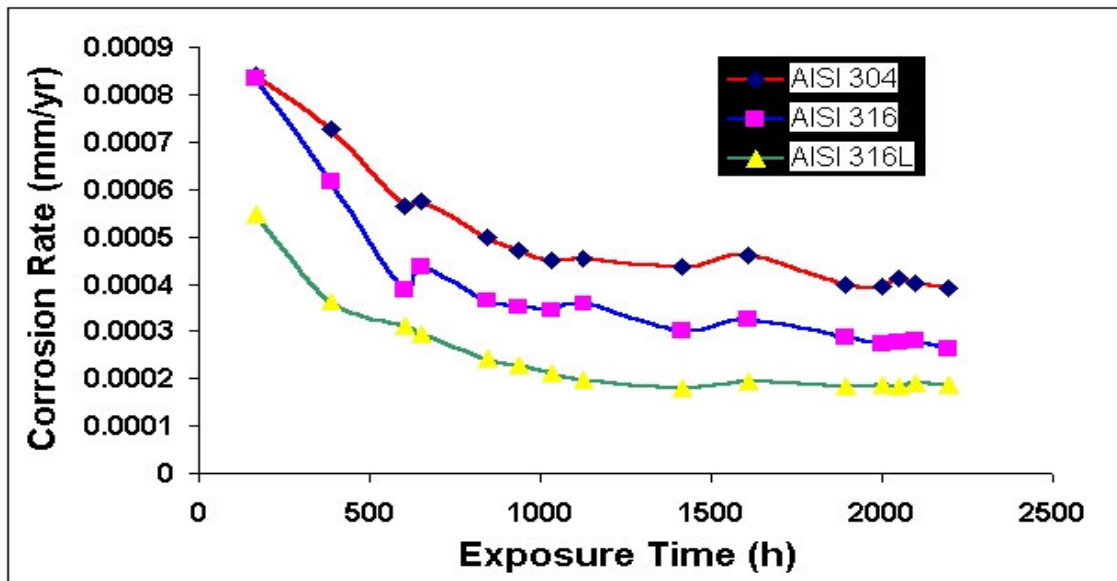
Figure 4.45. Corrosion rate vs. exposure time of stainless steels specimens tested at 9.6 m/s fluid velocity.

Calcium carbonate precipitation is further observed in two forms: aragonite and cubic. Figure 4.48 (a) and 4.49(a) show the optical microscope and SEM images of aragonite calcium carbonate precipitates, while 4.48(b) and 4.49(b) cubic precipitates. The EDX analysis results of the precipitates are shown in Figure 4.50.
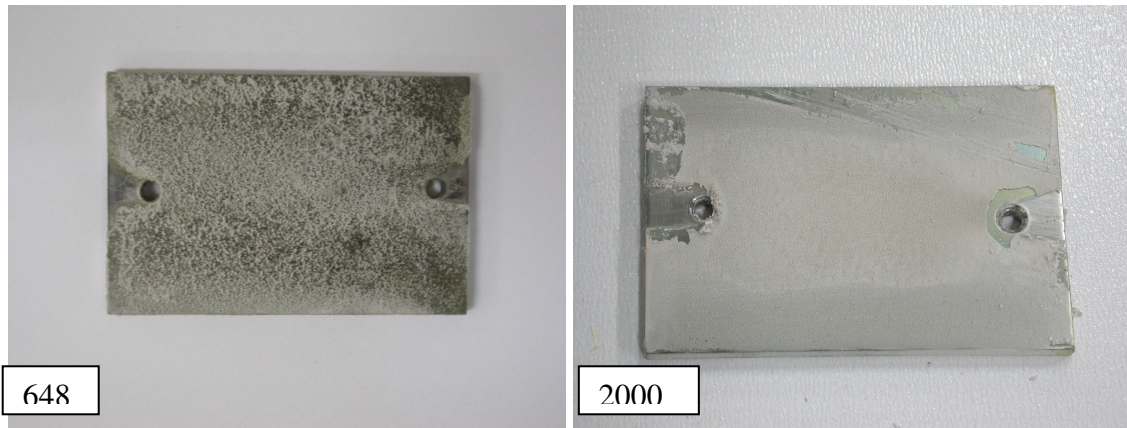
<center>(a)   (b)</center>

Figure 4.46. Calcium carbonate scaling on the surfaces of the AISI 304 austenitic stainless steel after (a) 648 and (b) 2000 h exposure to 0.02 m/s fluid velocity.
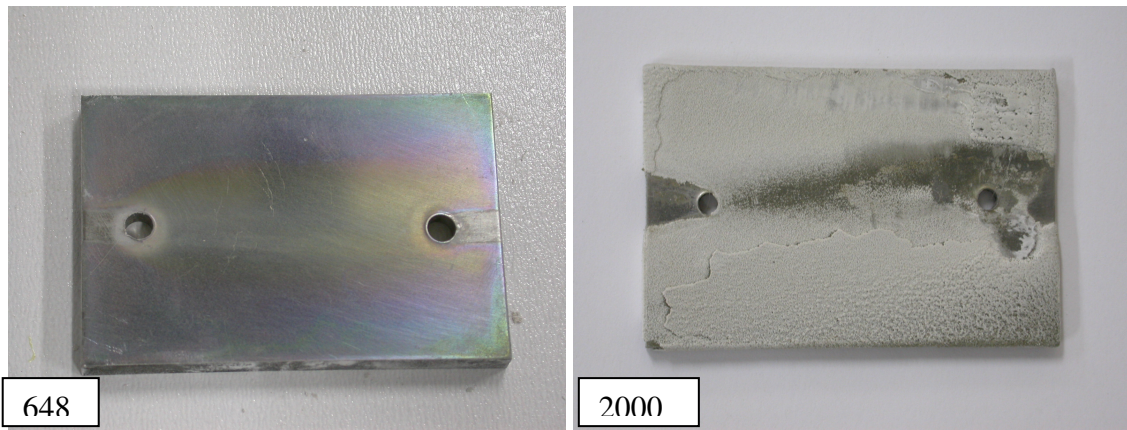
<center>(a)   (b)</center>

Figure 4.47. Calcium carbonate scaling on the surfaces of the AISI 304 austenitic stainless steel after (a) 648 and (b) 2000 h exposure to 9.6 m/s fluid velocity.
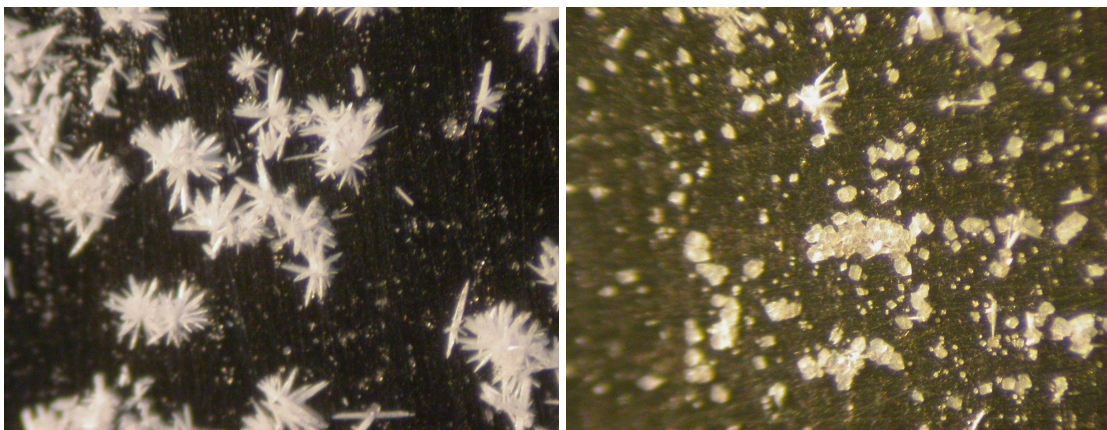
<center>(a)   (b)</center>

Figure 4.48. Stereo zoom microscope images of (a) aragonite and (b) cubic calcium carbonate precipitation on the surface of AISI 304 stainless steel.
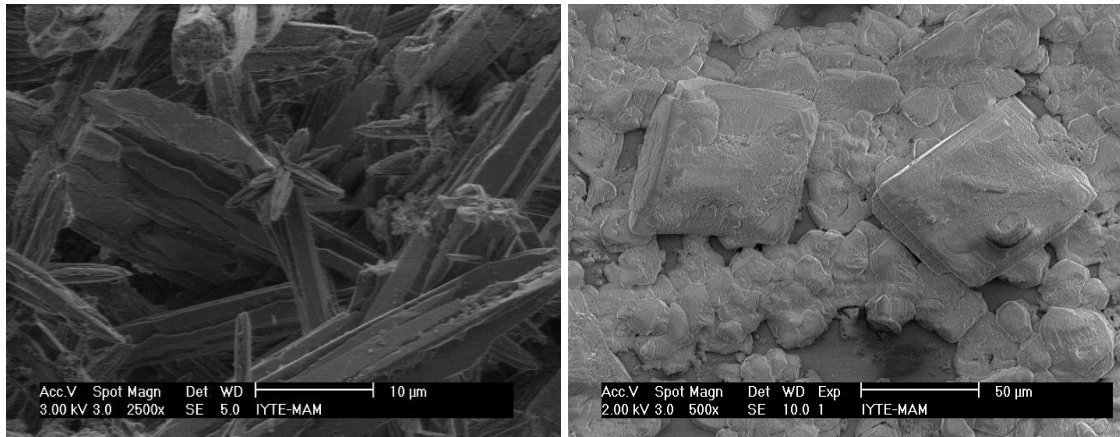
<div align="center">(a)   (b)</div>

Figure 4.49. SEM images of (a) aragonite and (b) cubic calcium carbonate precipitation on the surface of AISI 304 stainless steel.

Element	Wt%	At%
C	7,50	13,67
O	43,56	59,60
Ca	48,94	26,73
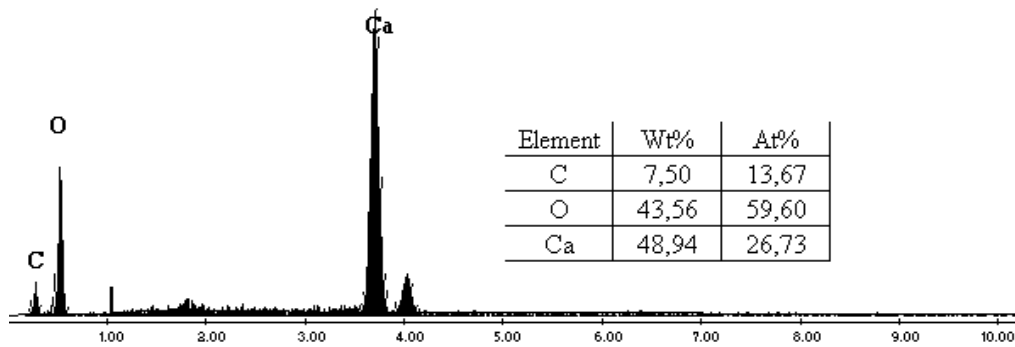
Figure 4.50. EDX analysis results of aragonite and cubic calcium carbonate precipitates.

Microscopic observations have further shown that the SRB form on the surfaces of the steels at both fluid velocities (Figure 4.51), while their numbers of occurance on the surface are relatively low in the samples tested at the low fluid velocity. Within the studied exposure time range (0-2250 h) pits were not detected on the surfaces of AISI 316 and 316L austenitic stainless steels. Few pits however formed on the surfaces of AISI 304 austenitic stainless steel samples merely in test samples at low fluid velocity (Figure 4.52). The measured maximum pit depths are 3.10, 2.71, 3.20 and 3.50μm for 2000, 2048, 2096 and 2192 h exposure, respectively.

The thickness loss of AISI 304 steel due to uniform corrosion at 2192 h exposure is 0.096 μm while the measured maximum pit depth is 3.5 μm, showing a higher rate of pitting rate in the AISI 304 steel. In the same steel, the maximum value of maximum pitting corrosion rates is 0.038 μm/day and the average value of pitting corrosion rates 0.035 μm/day. The measured maximum pitting length of maximum pit

depths are however higher, 0.11, 0.16, 0.33 and 0.55 mm for the exposure times of 2000, 2048, 2096 and 2192 h, respectively. The pits are also filled with SRB as shown in Figure 4.53. The EDX analysis of the pits show the high concentrations of the S in the pit (Figure 454(a) and (b)).
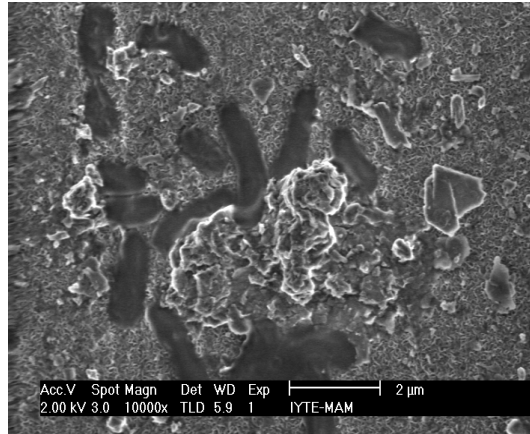
Figure 4.51. SEM image of SRB accumulation on the surface of AISI 316 steel at 0,02 m/sn fluid velocity.
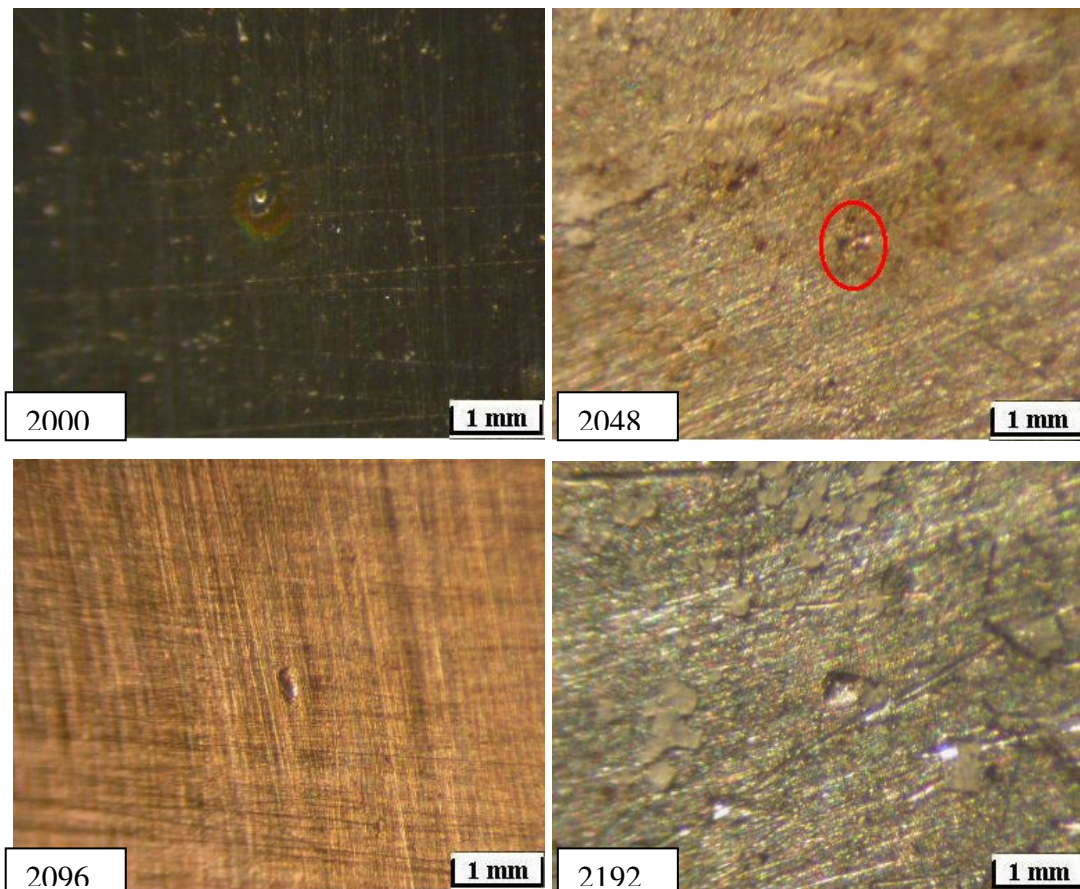
Figure 4.52. Stereo zoom microscope images of pits on the AISI 304 austenitic stainless steel surfaces exposed to 0.02 m/s geothermal water.
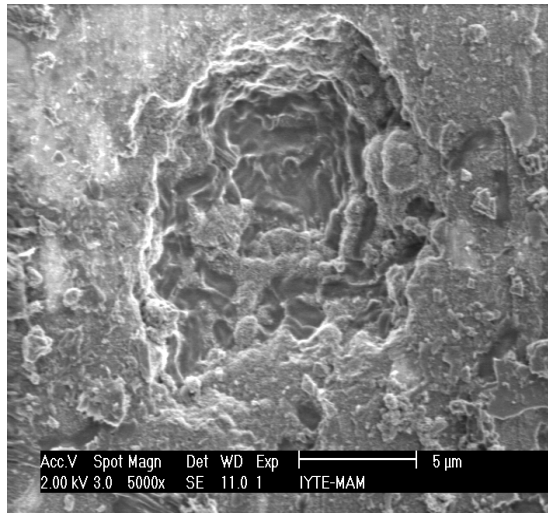
Figure 4.53. SEM images of sulphate reducing bacteria accumulation in pits.
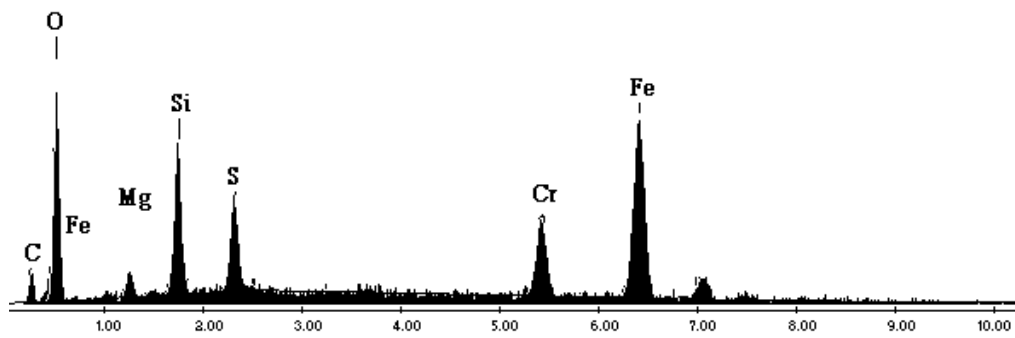
(a)
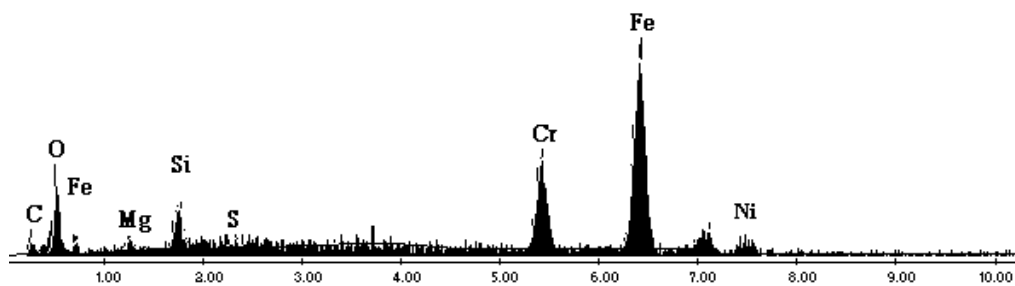
(b)

Figure 4.54. EDX analysis results of pit shown in Figure 4.53 (a) inside and (b) outside of the pit.

In Figure 4.55(a) and (b), the epoxy mounted and polished cross-section of the calcium carbonate scaling layer on samples of AISI 316 and AISI 316L after 2000 h exposure time in low fluid velocity is shown respectively. EDX analyse of calcium carbonate layer shown in Figure 4.55(a) is shown in Figure 4.56.

(a)   (b)
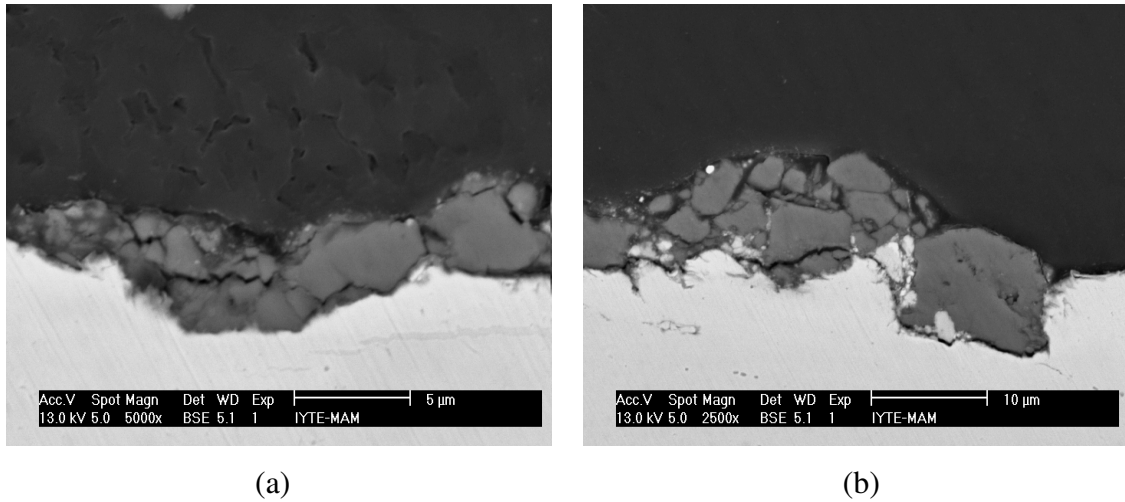
Figure 4.55. SEM images of calcium carbonate layer precipitated on (a) AISI 316, (b) AISI 316L stainless steel surface after 2000 hours exposured time in low fluid velocity.
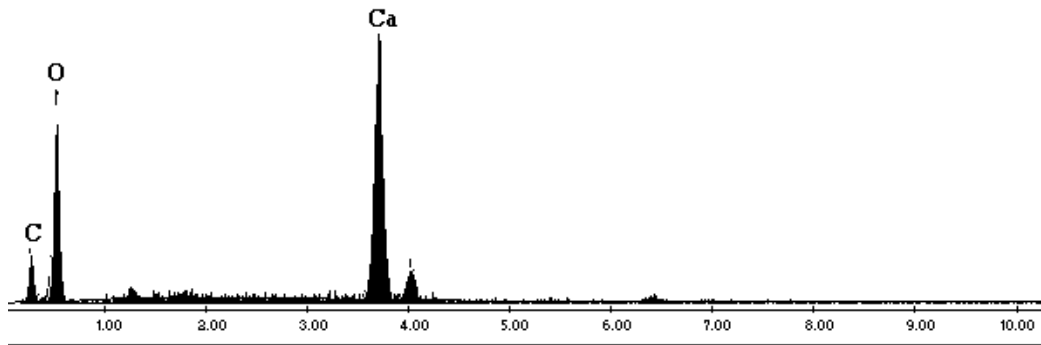
4.56. EDX analysis results of calcium carbonate layer shown in Figure 4.55(a)

4.5. Material Selections and The Effect of Fluid Velocity on the Corrosion Rate

The effect of fluid velocity on the corrosion rate of widely used pipeline materials, St-37, AISI 304 and AISI 316 and 316 L, in the geothermal district heating systems were investigated thorough the corrosion experiments conducted at the site on the tensile tests specimens and corrosion test coupons. Two fluid velocities, 0.02 and 9.6 m/s, showing the low or stagnant and high velocity fluid flow, respectively were selected for the corrosion experiments. The fluid temperature in stainless steel tests coupons experiemnts was 120 $^\circ$C, while it was 96 $^\circ$C in St-37 steel tensile test specimens. These tests were further accompained by the qualitative laboratory tests. The

results of laboratory and site experiments with the microscopically oberved corrosion products are tabulated in Tables 4.3 and 4.4 for 0.02 and 9.6 m/s fluid velocities, respectively.

Table 4.3. Laboratory and corrosion test results summary (0.02 m/s).

Material	Ryznar stability index	Pitting resistance equivalent	Electro potential (V)	Uniform Corrosion Rate (mm/y)	Average of max. pitting corrosion rate (μm/day)	Existence of SRB	CaCO$_3$ scaling
St-37	5.01	-	-0.18660	0.01780	0.600	Yes	Negligible
AISI 304	4.60	19.00	0.02010	0.00034	0.035	Yes	Heavy
AISI 316	4.60	25.25	0.01610	0.00010	negligible	Yes	Heavy
AISI 316 L	4.60	25.25	0.01529	0.00011	negligible	Yes	Heavy

Table 4.4. Laboratory and corrosion test results summary (9.6 m/s).

Material	Ryznar stability index	Pitting resistance equivalent	Electro potential (V)	Uniform Corrosion Rate (mm/y)	Average of max. pitting corrosion rate (μm/day)	Existence of SRB	CaCO$_3$ scaling
St-37	5.01	-	-0.18660	0.02200	0.3	Less than stagnant water	Negligible
AISI 304	4.60	19.00	0.02010	0.00039	negligible	Less than stagnant water	Heavy with some removed parts
AISI 316	4.60	25.25	0.01610	0.00026	negligible	Less than stagnant water	Heavy with some removed parts
AISI 316 L	4.60	25.25	0.01529	0.00018	negligible	Less than stagnant water	Heavy with some removed parts

The corrosion rates of the materials used in low temperature geothermal wells and plants vary significantly between different locations and wells. Lund et al. 2000

was investigated the uniform corrosion rates of 1010 carbon and AISI 304 stainless steels at fluid temperatures ranging between 21 to 110 ^{0}C in a geothermal reservoir in Klamath Falls, Oregon. It was found that the uniform corrosion rates were negligible for both steels, maximum 0.0039 mm/yr at fluid temperature of 93-99 ^{0}C in stagnant geothermal water. The uniform corrosion rate of an carbon steel exposed to a geothermal fluid of 70 ^{0}C and 5.5 to 8.5 pH was reported to vary between 0.017 and 0.023 mm/yr (Hirowatari et al. 1995). These corrosion rate values are in accord with the corrosion rates determined in this study for the low carbon steel, 0.017 and 0.022 mm/yr. The uniform corrosion rates even decreased below these values in the tested stainless steels. Therefore, the low uniform corrosion rates of steels found in low temperature geothermal systems show that uniform corrosion rate is not a main cause for the pipeline failure. It should be noted that uniform corrosion rates were calculated neglecting pitting corrosion effects on weight loss. In fact, uniform corrosion rate of studied steels are lesser than calculated uniform corrosion rates.

The investigations have shown that the uniform corrosion rate of carbon steels in fresh water increased with increasing water velocity since higher water velocities increased the supply of oxygen, carbon dioxide or hydrogen sulfide and the diffusion or transfer of ions by reducing the thickness of the stagnant film at the surface until a critical velocity reached (03-0.7 m/s), above which the corrosion rate decreased due to passivation (Matsushima 1992b, Davis 2003). It was also shown that the critical water velocity in fresh water depended on the concentration of chloride ions. Above about 100 ppm chloride content the chlorine ions prevented the passivation and there was no effect of critical velocity on the corrosion rate of carbon steels (Herce et al. 1995). In the case of erosion, the critical velocity reached after about 20 m/s (Ichikawa et al. 2000). The high chlorine content of the geothermal fluid (206-208 ppm) and the presence erosion dictate no critical velocitiy for pasivation of the investigated steels is expected.

Corrosion product morphology may be also effective in increasing uniform corrosion rate at increasing fluid velocities. The crystal form of corrosion products forming at the higher fluid velocity may not act as a barrier for the corrosion as efficiently as amorph form of corrosion product formed at the lower fluid velocity. It is also noted in Table 4.1 and 4.2 that the uniform corrosion rate of St-37 steel is at least one order magnitude greater than those of stainless steels even though the fluid temperature is relatively lower. This tendency is also seen in the measured high electropotential of St-37 steel in the laboratory tests.

The reduced corrosion rate of stainless as compared with St-37 is a combined effects of (a) reduced oxygen solubility at high temperatures, (b) formation of protective Cr-oxide and calcium carbonate films on the surface and (c) reduced SRB corrosion activities due to higher fluid temperature. Most common strains of SRB grow best at temperatures from 25 ^{o}C to 35 ^{o}C and a few thermophilic strains are capable of functioning efficiently above 60 ^{o}C (Web_2 2005). A study on stagnant water has shown that the corrosion of pipe at favorable corrosion temperatures of 35-50 ^{o}C was mainly due to the SRB activity since stagnation and low flow velocity conditions promoted the attachment of the bacteria to the metal surface (Elshawesh 2003). This explains the observed relatively reduced SRB activity on the steels at the higher fluid velocity as tabulated in Table 4.1 and 4.2. Torres-Sanchez investigated the microbiologically influenced corrosion in a geothermal system and concluded that SRB were found in the seperated geothermal water and steam, therefore the microbiologically influenced corrosion could be expected whereever geothermal fluid contacted with the steel (Torres et al. 2001). Amalhay showed that although very few SRB were present in the circulating geothermal fluid, they could be found in much greater and variable numbers on the corrosion coupons due to the fact that the number of bacteria was linked to the presence of a thick scale. Stagnant water may also lead to the formation of tubercle structures which may be initiated in an oxygen shielded a small area such as a grain of sand or a microbial colony (Rossum 1998). The increased SRB activity and tubercle formation at the low fluid velocity further lead to increase in pitting corrosion rate.

XRD investigations have shown the mackinawite formation on the St-37 surface in stagnant water while it was not found at the higher fluid velocity. This may be partly due to the increased rate of SRB accumulation in the stagnant water, leading to the formation of mackinawite all over the corroded surface. On the other hand, since few SRB observed on the steel surface exposed to the high fluid velocity, this may results in mackinawite precipitation at small local points on the surface, which cannot be detected by XRD. The work of Meyer (Amalhay et al. 1995) on the corrosion of carbon steel in H_2O-$NaCl$-CO_2-H_2S fluid system showed the formation of mackinawite at the end of a 20-week test. It was also shown in the same study that the nature of corrosion products depended on the initial pH of the corrosive environment and mackinawite was the main component of the film in the pH range between 6.6. and 8.4. Mackinawite was shown to be a protective corrosion product (Meyer et al. 1958). The protective nature of

mackinawite is in accord with the measured relatively lower uniform corrosion rate of St-37 carbon steel in the lower velocity fluid. It was further proposed that Fe^{2+} and HS^- ions reacted together either in the solution or on the surface of a corroded steel, leading directly to the formation of mackinawite (Rickard 1975, Wikjord 1976).

AISI 304 type stainless steel exposed to stagnant water would be expected to be less resistance against the pitting than AISI 316 stainless steels based on the predicted pitting resistance equivalent. This is in accord with the mesured pitting rates at the lower fluid velocity as tabulated in Table 4.1, while the expaosure time was insuffcent to form pits on the stainless steels at the higher fluid velocity.

Although the statistical studies showed any significant correlation between the corrosion rates and Ryznar stability index (Ellis 1985), the predictions based on Ryznar index were found in accord with experimental results. The Ryznar stability indexes shown in Tables 4.1 and 4.2 dictates relatively low rates of uniform corrosion in the tested samples and a heavy calcium carbonate scaling in stainless steel samples. Heavy calcium carbonate scaling was observed in the stainless steels at both velocities studied. Flow velocity is an important factor on the scale formation. It is recognized that velocity affected the fouling process as regard both deposition and removal steps and that, in general, high velocities may reduce scale formation due to increased deattachment (Epstein 1983, Taborek et al. 1972). Moreover, Andritsos and Karabelas found that the presence of fine aragonite particles greatly increased the calcium carbonate deposition rates in tubes, especially at low fluid velocities due to it's rippled appearance while the same concentration of colloidal silica particles did not exhibit any effect on the precipitation characteristics (Anditros and Karabelas 1999). Observed aragonite particles on the stainless steel surfaces at the high and low fluid velocity support a heavier calcium carbonate scaling formation in stagnant water due to greater scaling tendency of aragonite particles.

The service lifes of St-37 pipe materials were predicted 57 and 95-month for low and high fluid velocities, respectively. In the prediction, it was assumed that deeper pits initiated at the first stages of exposure would be able to survive and continue to grow at the same rate determined. Normally, some pits and tubercles initiated at the first stage of exposure could be inactive because of change in environmental parameters and water chemistry. The deepest pits initiated at the first stages of exposure time may be ineffective after a period of exposure but the second or third deepest pits will cause to fail of pipe. Another scenario, for example is that, a few year later, a new pit can initiate

and grow fastly and becomes the deepest pit, which is possible when significant changes in environmental parameters and water chemistry. Therefore, the prediction made on the service life of St-37 pipe materials was only valid for the investigated water chemistry and environmental parameters. The predicted minimum service lives of St-37, 57 and 95 months for fluid flow velocities between 0.02 and 9.6 m/s were in agreement with the reported St-37 pipe line service lives in the studied geothermal system. There has been only one St-37 pipe line failure due to pitting after 7 years service until 2005 at B-11 well. The water velocity was 2-3 m/s in the well. However, in the year of 2005, there were two pipeline failures after 9 years of service. This two failures could be possible caused by the pitting corrosion, since the pipes are still in the system, the main failure mechanism is not know.

This study revealed that St-37 material is prone to the pitting type corrosion. A suitable biocide chemical at recommended levels can be added to system in order to reduce SRB activity. Alternatively, the district heating system can be operated at high fluid velocities to reduce pitting corrosion. However, the second may need a much higher investment cost than replacement of St-37 pipes with stainless steel pipes.

CHAPTER V

CONCLUSIONS

An experimental study has been conducted to determine corrosion behavior of widely used pipeline steels including St-37, AISI 304 and AISI 316 and 316 L steels in the geothermal district heating systems. The corrosion experiments conducted at the site on the tensile tests specimens and corrosion test coupons. Two fluid velocities, 0.02 and 9.6 m/s, showing the low or stagnant and high velocity fluid flow, respectively were selected for the corrosion experiments. These tests were further accompained by the qualitative laboratory tests and extensive microstructural analysis on the corrosion products. The followings may be concluded;

1-Ryznar stability index, pitting resistance equivalent and electropotential calculations and measuments results showed well relations with experimental results.

2- Relatively lower corrosion rates of stainless steels at both high and low fluid velocity was partly due to (a) reduced oxygen solubility at high temperatures, (b) formation of protective Cr-oxide and calcium carbonate films on the surface and (c) reduced SRB corrosion activities due to higher fluid temperature.

3-Pitting corrosion rate was found to be promoted at low fluid velocity, mainly driven by the SRB activity and tubercle formation. The SRB activity however reduced at higher fluid velocities and on the stainless steel surfaces.

4-Calcium carbonate precipitation on the steel surface was scaled at higher rate at low fluid velocity than high fluid velocity. This was attributed to the fact that high velocities reduced scale formation due to increased deattachment and/or aragonite particles on the stainless steel surfaces.

5- The tensile tests on the St-37 corroded samples have shown that the UTS decreased as the exposure time increased. The decrease in the UTS of St-37 was pronounced in the samples tested at the lower fluid velocity, which showed a good agreement with the measured maximum pitting depts found in these samples.

6-The service lifetime of the St-37 was predicted for two selected fluid velocities using equation developed for the effect of defects on the bursting pressure of the pipelines. The predicted service life of St-37 were 57 and 95 month for low and high velocity fluid

flow respecitvely. These service lives was also comparable with the reported service lives of the pipeline used currently in the studied geothermal system.

7. To increase the service life of the St-37, a solution was proposed; addition of SRB activity reducing reagents to the fluids.

REFERENCES

AAH 1999. "Water Treatment", in *ASHRAE Application Handbook*, Chapter 47, p. 78.

Akkuş, İ. Aydoğdu, Ö. Sarp, S., 2002. "Ülkemiz Enerji Gereksinimin Karşılanmasında. Jeotermal Enerjinin Yeri", *IV.UTES Bildiriler Kitabı, cilt II*, İstanbul. pp. 619-628.

American Society for Testing and Materials G01-90 standard, 2000. "Practice for Preparing, Cleaning and Evaluating Corrosion Test Specimens".

Andritsos, N. Karabelas, A.J. Koutsoukos, P.G. 1998. "Scale Formation in Geothermal Plants", International Summer School on Direct Application of Geothermal Energy, Greece.

American Society for Testing and Materials E-8 standard "Standard Test Methods of Tension Testing of Metallic Materials".

American Society for Testing and Materials A53-94 standard "Dimensions and Weights for Welded Steel Pipes, Black, Plain End".

Amalhay, M. Akar, A. Ignatiadis, I. 1995. "Overview of the Deposition Phenomena in Geothermal Wells in the Paris Basin", Proceedings of the World Geothermal Congress, Italy, pp. 2497-2503.

Andritsos, N. Karabelas, A.J. 1999. "The Influence of Particulates on $CaCO_3$ Scale Formation", *J. Heat transfer*. Vol 121, p. 225-227

Armstead, H.C.H., 1983. *Geothermal Energy*, (E. & F. Nn Spon, London), p. 404.

Bullard, E. 1973. "Basic theories", *Geothermal Energy*, Review of Research and Development, UNESCO, Paris, p. 38.

Bendetritter, Y. Cormy, G. 1990. "Possible Approach to Geothermal Research and Relative Cost", Small Geothermal resources : A Guide to Development and Utilization", *UNITAR*, NewYork. pp. 59-69.

Butlin, K. Vernon, W. Whiskin, L. 1951. "Symposium on Corrosion of Buried Metals", Iron and Steel Inst, Vol 6, London. p. 29.

Bela, L. 1996. "*Stainless Steels and Their Properties*", (Euro-Inox Publication), p. 7.

Beech, L.B. Gaylarde, C.C. 1999. "Recent Advances In The Study of Biocorrosion-An Overview", *Revista de Microbiologia*, Vol. 30, pp. 177-190.

Brown, M. Nessim, M. Greaves, H. 1995. "Pipeline Defect Assestment : Deterministic and Probabilistic Considerations", Second International Conference on Pipeline Technology, Ostend, Belgium.

Carrier 1965: Handbook of air conditioning system design, *Carrier Corp, Syracuse*, NewYork, Vol. 7, p. 586.

Chan, S.H. 1989. "A Review on Solubility and Polymerisation of Silica", *Geothermics*, Vol. 18, pp. 49-56.

Cornell, R.M. Schwertmann, U. 1996. " The Iron Oxides, Structure, Properties, Reactions, Occurrence and Uses" *VCH Verlagsgesellschaft*, Weinheim, p. 79.

Colin, S. Kent, R.K. 2000. "Failure Analysis and Prevention - Velocity Effected Corrosion", in *ASM handbook MDE Engineers Inc*,Vol 11, p. 49.

Conover, M.F. Ellis, F.P. 1981. "*Material Selection Guideline for Geothermal Energy Systems*", NTIS Code DOE/RA/27026-1, (Radian Corporation, Austin, USA).

Criaud, A. Fouillac, C. 1989. "Sulfide Scaling in Low-Enthalpy Geothermal Environments : A Review", *Geothermics,* Vol. 18, p. 73-81.

Cunat, P.J. 2000. "*Stainless Steel in Drinking Water Systems*", (Euro-Inox Publication), p. 36.

Cumpson, P.J. Seah, M.P. Qiu, J.H. Castle, J.E., 1993. "NPL Report Code : DMM(A) 95", *Metrologia*, p. 63.

Davis, J.R. 2003. "*Corrosion Understanding Basics*", ASM International The Materials Information Society, USA.

Degiorgi, V.G. 2000. "Corrosion Basics and Computer Modelling", *Naval Research Laboratory*, Washington D.C.

Efird, K. D. Moller, G. E. 1978. "Electrochemical Characteristics of 304 and 316 Stainless Steels in Fresh Water as Functions of Chloride Concentration and Temperature" Paper Nr 87, *Corrosion/78*, Houston, TX, USA, p.12.

Ellis, F.P. 1985. "Companion Study Guide to Short Course on Geothermal Corrosion and Mitigation in Low Temperature Geothermal Heating", Geo-heat center, Oregon, USA.

Elshawesh, F. Abusowa, K. Mahfud, H. Elagdel, E. September 2003 "Microbiologically Influenced Corrosion of Type 304 Austenitic Stainless Steel Water Pipe", *Materials Performance*, pp. 54-58.

Energy Information Administration, *Annual energy outlook 1994*", DOE/EIA-0383(94), Washington DC (Jan. 1994), USA, Table 21.

Energy Information Admininstration, *Annual energy Review 2003*", section 10, Renewable Energy, Annual report, USA.

Epstein, N. 1983. "Thinking about heat transfer fouling : a 5 x 5 matrix", *Heat Tranfer Eng.* Vol. 4, pp. 43-56.

Flentje, M.E. Am, J. 1961. "Annual Report", Water works Assoc, Nr 53, p. 146.

Fontana, M.G. "*Corrosion Engineering*", (Mc-Graw Hill International Editions) Third Edition, 1987.

Francy, H. Bancon, G. Baron, J. Meignen. C.J. Seva, G. "The Gentle Solution With the Water Hardness : How to Avoid the Incrustations in Networks Without Chemicals – An Electro-Physics Technique Effective and Innovating", Rue du pont de fer 71100, *Chalon Sur Saone*, France, p. 13.

FRP I&II, Minerals Management Service Contract Nr 1435-01-CT-99-50001. "Appraisal and Development of Pipeline Defect Assessment Methodologies Final Report Phases I & II" Doc Ref CH109R001 Rev 0 JUNE 2000, Ascot, Berkshire. SL5 9NQ, p. 11.

Fujii, T. Bosei, K. 1983. "*Rust Prevention and control*", (Euro-Inox Publication), p.71.

Goddard, W.B. 1990. "Energy Fuel Resources and Their Contribuiton to Recent Global Air Pollution Trends", Transactions, *Geothermal Resources Council*, Vol 14, p. 643-649.

Hamrouni, B. Dhahbi, M. 2002. "Calco-carbonic Equilibrium Calculation", *Desalination –Elsevier*, Departement de Chimie, Faculte des Sciences de Tunis.

Henley, R.W. 1983. "pH and Silica Scaling Control in Geothermal Field Development", *Geothermics,* Vol 12, p. 307-321.

Hepbaşlı, A. Özgener, L. 2003. "Development of Geothermal Energy Utilization in Turkey : a review" Renewable Energy and Sustainable Energy Reviews.

Herce, J.A. Wright, E.J. Boros, J.A. Hailey, T.G. "Effect of Solution Chemistry and Flow on the Corrosion of Carbon Steel in Sweet Production", *CORROSION/95*, Paper nr 95111, Orlando, FL, USA.

Hirowatari, K. Kusaba, S. Izumi, J. Takeuchi, K. May 1995. "Production of Sulfuric Acid From Geothermal Power Station Exhausted Gas for Use in Scale Prevention", Proceedings of The World Geothermal Congress, Italy, p. 2445-2450.

Hoar, T.P. 1967. "Corrosion Science Report", *Corrosion Science*, Vol 7, p. 355.

Hochstein, M.P. 1990. "Classificaiton and Assetment of Geothermal Resources, Small Geothermal Resources : A Guide to Development and Utilization", *UNITAR*, NewYork, pp. 31-57.

Huttrer, G.W. 2000. "The Status of World Geothermal Power Generation - 1995-2000" Proceedings of the world geothermal congress, Japan.

Ichikawa, K. Nagano, K. Kobayashi, S. Kitajima, N. 1973. "Ebara Engineering Report", Rev Nr 85, p. 2.

Jones, D.R.H. 1993. "Materials Failure Analysis : Case Studies and Design Implications" Headington Hill Hall, *Pergamon press*, U.K, p. 8.

Kent, R.K. 2000. "Failure analysis and prevention-uniform corrosion", *ASM handbook, MDE Engineers Inc*, Vol.11, p. 51.

Kizito, M.O. "Corrosion Tests in Cooling Circuit Water at Olkaria 1 Plant and Scale Predictions for Olkaria and Reykjanes Fluids", Geothermal Training Programme, The United Nations Universty, Reports 2002, Nr 10, USA.

Kristmannsdóttir, H. Ólafsson, M. Thórhallsson, S. 1989. "Magnesium Silicate Scaling in District Heating Systems in Iceland", *Geothermics,* Vol 18, p. 191-198.

Lindal, B. 1973. "Industrial and Other Applications of Geothermal Energy", *Geothermal Energy,* UNESCO, Paris, p. 135-148.

Lippmann, F. 1973. "*Sedimentary Carbonate Minerals in : Mineral Rocks and Inorganic Materials*", (Springer-Verlag, New York).

Loewental, R.E. Marais, G.V.R. 1976. "Carbonate Chemistry of Aqueous Systems", *Ann Arbor*, Michigan, USA, p. 28.

Lopez, D.A. Schreiner, W.H. Sanchez, S.R. Simison, S.N. 2002. "The Influence of Carbon Steel Microstructure on Corrosion Layer, an XPS and SEM Characterization", *Applied surface science*, Elsevier, Vol 42, p. 20.

Lund, J.W. 1999. "World Status of Geothermal Energy Use Overview 1995-1999", Geo-Heat center, Oregon institute of Technology Geothermal Lesson Presentation, Klamath Falls, OR, USA.

Lund, J.W. Culver, G. Lienau, J.P. 2000. "Groundwater Characteristics and Corrosion Problems Associated With The Use of Geothermal Water In Klamath Falls, Oregon" Geo-heat Utilization Center, Oregon Institute of Technology presentation notes, USA.

Matsushima, I. 1992a. "Carbon Steel Corrosion by Seawater", in *Uhlig's Corrosion Handbook,* Second Edition, (Mc-Graw Hill International Editions), Chapter 32, p. 545.

Matsushima, I. 1992b. "Carbon Steel Corrosion by Freshwater", in *Uhlig's Corrosion Handbook*, Second Edition, (Mc-Graw Hill International Editions), Chapter 31, p. 529.

Matsushima, I. 1992c. "Localized Corrosion of Iron and Steel", in *Uhlig's Corrosion Handbook,* Second Edition, Mc-Graw Hill International Editions, Chapter 34, p. 561.

Maeng, S.M. 1999. "Characterization of Steel Corrosion In an Aggresive Environment" Master Thesis on Environmental Enginnering of New Jersey Institute of Technology, Department of Civil and Environmental Engineering, p. 32.

Mertoğlu, O. Canlan, A. Bakır, N. Dokuz, İ. Kaya, T. 2000. "Geothermal Direct Use Application in Turkey : Technology and Economics", Proceedings World Geothermal Congress, May 28-June 10 (2000), p 3505-3510, Kyushu-Japan.

Metal Handbook: Vol 10 on Materials Characterization, 9th ed, American Society for Metals, Metals Park, Ohio, 1986, p. 89.

Meyer, F.H. Riggs, O.L. Meglasson, R.L. Sudbury, J.D. 1958. "Corrosion Products of Mild Steel in Hydogen Sulfide Environments", *Corrosion*, Vol 14, pp. 69-75.

Muffler, P. Cataldi, R. 1978. "Methods for Regional Assestment of Geothermal Resources", *Geothermic,* Vol. 7, pp. 53-89.

Nemzer, M. Carter, A. 2000. "Introduction to Geothermal Energy slide show", Geothermal Education Office, Geothermal information presentation slide shows, USA.

Nicholson, K. 1993. "Geothermal Fluids", *Springer Verlag*, Berlin, Vol 18, p. 264.

Papavinasam, S. 1992. "Corrosion Inhibitors" in *Uhlig's Corrosion Handbook*, Second Edition, (Mc-Graw Hill International Editions), Chapter 59, p. 1089.

Qiu, J.H. 2002. "Passivity and Its Breakdown on Stainless Steels and Alloys", *Surface and Interface Analysis*, Vol. 33, pp. 830-833.

Rimstidt, J.D. Barnes, H.L. 1980. "The kinetics of silica-water reactions", *Geochim-Cosmochim Acta,* Vol. 44, pp. 1683-1699.

Roberge, P.R. "*Handbook of Corrosion Engineering*", (Mc-Graw-Hill International Editions), 2000, p. 410.

Rossum, J.R. 1998. "Fundementals of Metallic Corrosion in Fresh Water", Roscoe Moss Company education notes.

Rafferty, K.D. 1992. "Chapter 10 - Piping" Geo-heat center, Oregon, USA.

Rickard, D.T. 1975. "Kinetics and Mechanism of Pyrite Formation at Low Temperatures", *Amer Journal of science*, Vol 275, pp. 636-652.

Reeves, J.N. 1997. "Chemical Speciation Modelling of the Cooling Water Circuit at Matla Power Station" Master Thesis in the Department of Chemical Engineering, Universty of Natal, Durban.

Riggs, O.L. 1973. "Corrosion Inhibitors", *NACE International*, Texas, USA , pp. 11-15.

Seah, M.P. Qiu, J.H. Castle, J.E. 1994. "Metrologia Report", *Metrologia* (1994), pp. 31-93.

Serpen, U. 1999. "Türkiye'de Jeotermal Enerjinin Çevreyle Uyumlu Kullanımı", *JENARIUM*, pp. 127-136.

Shibata, T. 1992. "Corrosion Probability and Statistical Evaluation of Corrosion Data", in *Uhlig's Corrosion Handbook,* Second Edition, (Mc-Graw Hill International Editions), Chapter 22, p. 367.

Taborek, J. Aoki, T. Ritter, R.B. Palen, J.W. Knudsen, J.G. 1972. "Predictive Methods for Fouling Behaviour", *Chemical. Eng. Progr*. Vol. 68 (2), pp. 59-67.

Torres, R. Sanchez, Gonzalez. M.C. Martinez, H. November 2001. "Microbiologically Influenced Corrosion in a Geothermal Electric Power Plant", *Materials performance*, pp. 46-49.

Van Delinder, L.S. 1984. "Inhibitors, Corrosion Basics : An Introduction" *NACE International*, pp. 127-146.

Web_1, 2005. Cranfield Company Education Web Site, 12/02/2005. http://www.cranfield.ac.uk

Web_2, 2005. Corrosion Experts Education Web Site, 20/03/2005. http://www.corrosion-doctors.org.

Web_3, 2005. Steel supplier's Web Site, 21/04/2005. http://www.al6xn.com.

White, D.E. 1973. "Characteristics of Geothermal resources", *Geothermal Energy*, Stanford Universty Press , Vol. 8, p. 69-94.

Wikjord, A.G. Rummery, T.E. 1976. "Crystallisation of Pyrite From Deoxygenated Aqueous Sulfide Solutions at Elevated Temperature and Pressure", *Canadian Minerologist*, Vol. 14, p. 571-573.

Yuzwa, G. F. Eng, P. 1991. "Corrosion by Sulfate Reducing bacteria", Presented at Alberta Public Works, Supply and Services Property Management Operations Division Water Treatment Co-ordinators' Meeting 14, Italy.

Zheng, J.H. 2000. "Electrochemical Techniques for Corrosion Testing and Monitoring", *MetaLogic,* Belgium, Vol. 24, p. 18.

APPENDICES

APPENDIX A

 Designation: ASTM G01-90

Standard Practice for Preparing, Cleaning and Evaluating Corrosion Test Specimens

1.Scope

1.1.This practice covers suggested procedures for preparing bare, solid metal specimens for test, for removing corrosion products after the test has been completed, and for evaluating the corrosion damage that has occured. Emphasis is placed on procedures related to the evaluation of corrosion by mass loss and pitting measurement. (Warning- In many cases the corrosion product on the reactive metals titanium and zirconişum is a hard and tightly bonded oxide that defies removel by chemical or ordinary mechanical means. In many such cases, corrosion rates are established by mass gain rather than mass loss)

1.2.This standard does not purport to address all of the safety concerns, if any, associated with its use. It is the responsibility of the user of this standard to establish appropriate safety and health practices and determine the applicability of regidatory limitations prior o use. For specific precautionary statements, see 1 and 7.2.

2. Referenced Documents

2.1.ASTM Standards:

A262 Practices for detecting susceptibility to intergranular attact in austenitic stainless steels.

D1193 Specification for Reagent water

D1384 Test method for corrosion test for engine coolants in glassware

D2776 Test method for corrosivity of water in the absence of heat transfer

G15 Terminology relating to corrosion and corrosion testing

G16 Guide for applying statistics to analysis of corrosion data

G31 Practice for laboratory imersion corrosion testing of metals

G33 Practice for recording data from atmospheric corrosion tests of metallic coated steel specimens.

G46 Guide for examination and evaluating of pitting corrosion

G50 Practice for conducting atmospheric corrosion tests on metals

G78 Guide for crevice corrosion testing of iron Base and Nickel Base stainless alloys in seawater and other chloride-containing aqueous environment.

3.Terminology

3.1. See terminology G15 for terms used in this practice

4.Significance and Use

4.1.The procedures given are designed to remove corrosion products without significant removal of base metal. This alows an accurate determination of the mass loss of the metal or alloy that occured during exposure to the corrosive environment.

4.2.These procedures, in some cases, may apply to metal coatings. However, possible effects from the substrate must be considered.

5.Reagents and Materials

5.1.Purity of Reagents-Reagent grade chemicals shall be used in all tests.Unless otherwise indicated, it is intended that all reagents conform to the specifications of the Committe on Analytical Reagents of the American Chemical Society where such specifications are available. Other grades may be used, provided it is first ascertained that the reagent is of sufficiently high purity to permit its use without lessening the accuracy of the determination.

5.2.Purity of Water-Unless otherwise indicated, references to water shall be understood to mean reagent water as defined by Type IV of Specification D 1193.

6.Methods for Preparing Specimens for Test

6.1. For laboratory corrosion tests that simulate exposure to service environments, a commercial surface, closely resembling the one that would be used in service, will yield the most meaningful results.

6.2. It is desirable to mark specimens used in corrosion tests with a unique designation during preparation. Severel techniques may be used depending on the type of specimen and test.

6.2.1.Stencil or Stamp-Most metallic specimens may be marked by stenciling, that is, imprinting the designation code into the metal surface using hardened steel stencil stamps hit with a hammer. The resulting imprint will be visible even after substantial corrosion has occured. However, this procedure introduces localized strained regions and the possibility of superficial iron contamination in the marked area.

6.2.2. Electric engraving by means of a vibratory marking tool may be used when the extent of corrosion damage is known to be small. However, this approach to marking is much more susceptible to having the marks lost as a result of corrosion damage during testing.

6.2.3. Edge notching is especially applicable when extensive corrosion and accumulation of corrosion products is anticipated.Long term atmospheric test and sea water immersion tests on steel alloys are examples where this approach is applicable. It is necessary to develope a code system when using edge notches.

6.2.4. Drilled holes may also be used to identify specimens when extensive metal loss, accumulation of corrosion products, or heavy scaling is anticipated. Drilled holes may be simpler and less costly than edge notching. A code system must be developed when using drilled holesç Punched holes should not be used as tehy introduce residual strain.

6.2.5.When it is undesirable to deform the surface of specimens after preparation procedures, for example, when testing coated surfaces, tags may be used for specimen identification. A metal or plastic wire can be used to attach the tag to the specimen and the specimen identification can be stamped on the tag. It is important to be sure that there are no galvanic intractions between the tag, wire, and specimen.

6.3.For more searching tests of either the metal orthe metal environment, standart surface finishes may be preferred. A suitabe procedure might be:

6.3.1.Degrease in an organic solvent or hot alkaline cleaner.

6.3.2.Pickle in an appropriate solution if oxides or tarnish are present. In some cases the chemical cleaners described in section 6 will be suffice.

6.3.3Abrade with a slurry of an appropriate abrasive or with an abrasive paper. The edges as well as the faces of the specimens should be abraded to remove burrs.

6.3.4.Rinse thoroughly, hot airdry, and store in desiccator.

6.4.When speicmen preparation changes the metallurgical conditions of the metal, other methods should be chosen or the metallurgical condition must be corrected by subsequent treatment. For example, shearing a specimen to size will cold work and may possibly fracture the edges. Edges should be machined.

6.5. The clean, dry specimens should be measured and weighed. Dimensions determined to the third significant figure and mass determined to the fifth significant figure are suggested. When more significant figures are available on the measuring instruments, they should be recorded.

7.Methods for Cleaning After Testing

7.1. Corrosion product removal procedures can be divided into three general categories: mechanical, chemical and electrolytic.

7.1.1. An ideal procedure should remove only corrosion products and not result in removal of any base metal. To determine the mass loss of the base metal when removing corrosion products, replicate uncorroded control specimens should be cleaned by the same procedure being used on the test specimens. By weighing the control specimen before and after cleaning, the extent of metal loss resulting from cleaning can be utilized to correct the corrosion mass loss.

7.1.2. The procedure given in 7.1.1 may not be reliable when heavily corroded specimens are to be cleaned. The application of replicate cleaning procedures to specimens with corroded surfaces will often, even in the absence of corrosion products, result in continuing mass losses. This is because a corroded surface, particularly of a multiphase alloy, is often more suspectible than a freshly machined or polished surface to corrosion by the cleaning procedure. In such cases, the following method of determining the mass loss due to the cleaning procedure is preferred.

7.1.2.1. The cleaning procedure should be repeated on specimen severel times. The mass loss should be detrmined after each cleaning by weighing the specimen.

7.1.2.2. The mass loss should be graphed as a function of the number of equal cleaning cycles as shown in figure 1. Two lines will be obtained: AB and BC. The latter will correspond to corrosion of the metal after removal of corrosion products. The mass loss due to corrosion will correspond approximately at point B.

7.1.2.3. To minimize uncertainty associated with corrosion of the metal by the cleaning method, a method should be chosen to provide the lowes slope (near to horizontal) of line BC
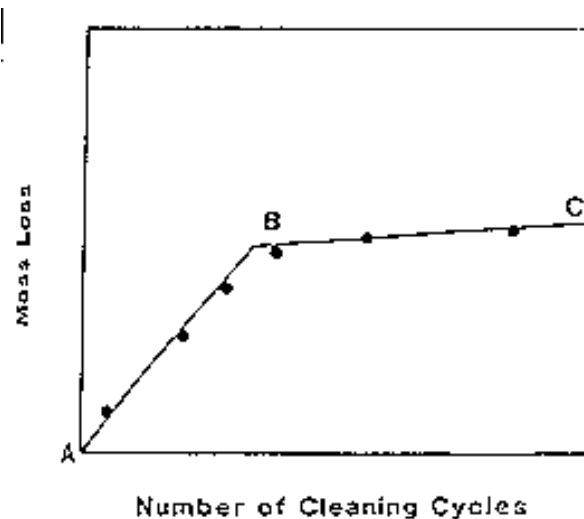
Figure 1.Mass loss of corroded speicmens resulting from repetitive cleaning cycles.

7.1.3.Repeated treatment may be required for complete removal of corrosion products. Removal can often be confirmed by examination with a low power microscope. This is particularly useful with pitted surfaces when corrosion products may accumulate in pits. This repeated treatment may also be necessary because of the requirements of 7.1.2.1. Following the final treatment, the specimen should be thoroughly rinsed and immediately dried.

7.1.4. All cleaning solutions shall be prepared with water and reagent grade chemicals.

7.2. Chemical procedures involve immersion of the corrosion test speicmens in a specific solution that is designed to remove the corrosion products with minimal dissolution of any base metal. The choice of chemical procedure to be used is partly a matter of trial and error to establish the most effective method for a specific metal and type of corrosion product scale.

7.2.1.Chemical cleaning is often preceded by light brushing or ultrasonic cleaning of the test specimen to remove loose, bulky corrosion products.

7.2.2.Intermittent removel of specimens from the cleaning solution for light brushing or ultrasonic cleaning can often facilitate the removal of tightly adherent corrosion products.

7.2.3.Chemical cleaning is often followed by light brushing or ultrasonic cleaning in reagent water to remove loose products.

7.3.Electrolytic cleaning can also be utilized for removal of corrosion products.

7.3.1. Electrolytic cleaning should be preceded by brushing or ultrasonic cleaning of the test specimen to remove any loose, bulky corrosion products. Brushing or ultrasonic

cleaning should also follow the electrolytic cleaning to remove any loose sime or deposit.s. This will help to minimize any redeposition of metal from reducible corrosion products that would reduce the apparent mass loss.

7.4.Mechanical procedures can include scraping, scrubbing, brushing, ultrasonic cleaning, mechanical shocking, and impact blasting (for example, grit blasting, water-jet blasting, and so forth). These methods are often utilized to remove heavily encrusted corrosion products. Scrubbing with a non metallic bristle brush and a mild abrasive-distilled water slurry can also be used to remove corrosion products.

7.4.1.Vigorous mechanical cleaning may result in the removal of some base metal; therefore, care should be exercised. These should be used only when other methods fail to provide adequate removal of corrosion products. As with other methods, correction for metal loss due to the cleaning method is recommended. The mechanical forces used in cleaning should be held as nearly constant as possible.

8.Assessment of Corrosion Damage

8.1. The initial total surface area of the specimen (making corrections for the areas associated with mounting holes) and the mass lost during the test are determined. The avarage corrosion rate may then be obtained as follows:

$$Corrosion\,Rate = \frac{K \times W}{A \times T \times D}$$

Where:

K=a constant (see 8.1.2)

T= time f exposure in hours

A=area in cm^2

W=mass loss in grams, and

D=density in g/cm^3

8.1.1.Corrosion rates are not necessarily constant with time of exposure. See practice G 31 for further guidance.

8.1.2.Many different units are used to express corrosion rates. Using the units in 7.1 for T, A, W, and D, the corrosion rate can be calculated in a variety of units with the following appropriate value of K:

Corrosion Rate Units Desired	Constant (K) in Corrosion Rate Equation
mils per year (mpy)	3.45×10^6
inches per year (ipy)	3.45×10^3
inches per month (ipm)	2.87×10^2
millimetres per year (mm/y)	8.76×10^4
micrometres per year (um/y)	8.76×10^7
picometres per second (pm/s)	2.78×10^6
grams per square meter per hour (g/m²·h)	$1.00 \times 10^4 \times D$
milligrams per square decimeter per day (mdd)	$2.40 \times 10^6 \times D$
micrograms per square meter per second (µg/m²·s)	$2.78 \times 10^6 \times D$

Note 5—If desired, these constants may also be used to convert corrosion rates from one set of units to another. To convert a corrosion rate in units X to a rate in units Y, multiply by K_Y/K_X; for example:

$$15 \text{ mpy} = 15 \times (2.78 \times 10^6)/(3.45 \times 10^6) \text{ pm/s} \qquad (2)$$

8.1.3. In the case of sacrificial alloy coatings for which there is preferential corrosion of a component whose density differs from that of the alloy, it is prefable to use the density of the corroded component (instead of the initial alloy density) for calcultaing avarage thickness loss rate by use of Eq.1.This is done as follows: (1) cleaning to remove corrosion products only and determine the mass loss of the corroded component; (2) stripping the remaining coating to detemine the mass nof the uncorroded component; (3) chemical analysis of the stripping solution to determine the composition of the uncorroded component (4) performing a mass balance to calculate the composition of the corroded components (5) using the mass and density of the corroded component to calculate the avarage thickness loss rate by use of eq.1

The procedure described above gives an avarage penetration rate of the coating but the maximum penetration for a multiphase alloy may be larger when the corroded phase is not uniformly distributed across the surface. In such cases, it is generally considered good practice to obtain a cross section through the corroded surface for microscopic examination. This examination will reveal the extent of selective corrosion of particular phases in the coating, and help in understanding the mechanism of attack.

8.2. Corrosion rate calculated from mass losses can be misleading when deterioration is highly localized, as in pitting or crevice corrosion. If corrosion is in the form of pitting, it may be measured with a depth gage or micrometer caliper with pointed anvils. Microscopical methods will determine pir depth by focusing from top to bottomof the pit when it is viewved from above (using a calibrated focusing knob) or by examining a section that has been mounted and metallographically polished. The pitting factor is

the ration of the deepest metal penetration to the average metal penetration (as measured by mass loss)

8.3. Other methods of assessing corrosion damage are:

8.3.1 Appearance- the degration of appearance by rusting, tarnishing or oxidation.

8.3.2. Mechanical Properties- An apparent loss in tensile strength will result if the cross-sectional area of the specimen is reduced by the corrosion. Loss in tensile strength will result if compositional change, such as deallying taking place, Loss in tensile strength and elongation will result from localized attack, such as cracking or intergranular corrosion.

APPENDIX B

Ⓐⓢⓣⓜ E 8

Dimensions

	Standard Specimens				Subsize Specimen	
	Plate-Type, 1½-in. Wide		Sheet-Type, ½-in. Wide		¼-in. Wide	
	in.	mm	in.	mm	in.	mm
G — Gage length (Notes 1 and 2)	8.00 ± 0.01	200.0 ± 0.2	2.000 ± 0.005	50.0 ± 0.1	1.000 ± 0.003	25.0 ± 0.1
W — Width (Notes 3 and 4)	1½ + ⅛ − ¼	40 ± 2	0.500 ± 0.010	12.50 ± 0.25	0.250 ± 0.005	6.25 ± 0.10
			thickness of material			
T — Thickness (Note 5)						
R — Radius of fillet, min (Note 6)	1	25	½	13	¼	6
L — Over-all length, min (Notes 2 and 7)	18	450	8	200	4	100
A — Length of reduced section, min	9	225	2¼	60	1¼	32
B — Length of grip section, min (Note 8)	3	75	2	50	1¼	32
C — Width of grip section, approximate (Notes 4 and 9)	2	50	¾	20	⅜	10

NOTE I —For the IVi-in. (40-mm) wide specimen, punch marks for measuring elongation after fracture shall be made on the flat or on the edge of the specimen and within the reduced section. Either a set of nine or more punch marks 1 in. (25 mm) apart, or one or more pairs of punch marks 8 in. (200 mm) apart may be used.

NOTE 2—When elongation measurements of P/i-in. (40-mm) wide specimens are not required, a minimum length of reduced section *(A)* of 2.000 ± 0.005 in. (50.0 ± 0.1 mm) may be used with all other dimensions similar to the plate-type specimen.

NOTE 3~For the three sizes of specimens, the ends of the reduced section shall not differ in width by more than 0.004, 0.002 or 0.001 in. (O.I, 0.05 or 0.03 mm), respectively. Also, there may be a gradual decrease in width from the ends to the center, but the width at each end shall not be more than 0.015, 0.005, or 0.003 in. (0.4, 0.1 or 0.08 mm), respectively, larger than the width at the center.

NOTE 4—For each of the three sizes of specimens, narrower widths! Wand O may be used when necessary. In such cases the width of the reduced section should be as large as the width of the

material being tested permits; however, unless stated specifically, the requirements for elongation in a product specification shall not apply when these narrower specimens are used.

NOTE 5— The dimension T is the thickness of the test specimen as provided for in the applicable material specifications. Minimum thickness of 172-in. (40-mm) wide specimens shall be •'/>»; in. (5 mm). Maximum thickness of V_z-in. (12.5-mm) and Vi-in. (6.25-mm) wide specimens shall be VK in. (16 mm) and Vi in. (6.25 mm), respectively.

NOTE 6— For the IVi-in. (40-mm) wide specimen, a M>-in. (13-mm) minimum radius at the ends of the reduced section is permitted for steel specimens under 100 000 psi (690 MPa) in tensile strength when a profile cutter is used to machine the reduced section.

NOTE 7—To aid in obtaining axial loading during testing of Vi-in. (6-mm) wide specimens, the over-all length should be as large as the material will permit, up to 8.00 in. (200 mm).

NOTE 8—It is desirable, if possible, to make the length of the grip section large enough to allow the specimen to extend into the grips a distance equal to two thirds or more of the length of the grips. If the thickness of Vi-in. (13-mm) wide specimens is over % in. (10 mm), longer grips and correspondingly longer grip sections of the specimen may be necessary lo prevent failure in the grip section.

NOTE 9-For the three sizes of specimens, the ends of the specimen shall be symmetrical in width with the center line of the reduced section within 0.10, 0.05 and 0.005 in. (2.5, 1.0 and 0.1 mm), respectively. However, for referee testing and when required by product specifications, the ends of the 7i-in. (12.5-mm) wide specimen shall be symmetrical within 0.01 in. (0.2 mm).

NOTE 10— Specimens with sides parallel throughout their length are permitted, except for referee testing, provided: *(a)* the above tolerances are used; *(b)* an adequate number of marks are provided for determination of elongation; and (r) when yield strength is determined, a suitable extensometer is used. If the fracture occurs at a distance of less than 2 W from the edge of the gripping device, the tensile properties determined may not be representative of the material. In acceptance testing, if the properties meet the minimum requirements specified, no further testing is required, but if they are less than the minimum requirements, discard the test and retest.

APPENDIX C

EDX (Energy Dispersive X-ray Microanalysis)

Interpretation of results:

The results of EDX Analysis are usually presented as a spectrum. In this graphical representation the X -axis represents the energy level - and therefore identifies the elements, and the Y-axis provides the number of counts of each element detected.

A common error equates peak height to the quantity of each element present. In order to provide an accurate determination of the quantity of a particular element there are a number of factors, which must be applied to the number of counts. These corrections are performed and the results are presented in a table displayed below the spectrum. The quantities as presented in the table are normalized to 100% and displayed as weight % (wt%).

The results obtainable through a modern 'Quantitative Standardless Analysis' package offer a very accurate representation of the composition of the material (with the exception, generally, of trace elements below the 1000 ppm detection level). Nevertheless, the figures provided in the weight% table need to be considered according to the guidelines provided below;

Results in weight %	Relative % i.e. 'the error could be up to'
100 – 20	5
20 - 5	10
5 - 1	20
1 - 0.2	50 - 100

For example: if you have a result where Pb = 21.13% this is accurate to ~5% (21.13 x 5% = 1%) so the result of Pb is between 20 and 22. As may be seen from the figures above there is a very wide margin of error for low concentrations of elements.

The software is under continual development in this area and we expect updates on a regular basis. The so-called Phi-Ro-Z standardless quantification package is used routinely as it is more accurate in light element analysis than the older ZAF package, which is still available as an alternative.

To illustrate the points mentioned above, an Example is provided overleaf. Note that although the Oxygen peak is not significant on the spectrum once quantitative analysis is performed Oxygen is found to comprise about 30% of the specimen. The large Silica peak might suggest that there is more Silica than Oxygen - but the quantitative results show that it is less than the Oxygen. The quantitative program performs complex algorithms to correct for matrix effects, atomic mass (Z), absorption (A) and fluorescence (F) effects of the different elements to arrive at the figures provided in the table.

It should be noted that the ideal specimen for EDX microanalysis is perfectly flat and polished. Although the current software does take a limited amount of surface roughness into account it is safe to assume that greater surface roughness will mean less reliable and consistent results.